UNIVERSITY OF CALIFORNIA
RIVERSIDE

Combined Computational and Experimental Approach in the Synthesis and Characterization of Magnetic Metal Borides

A Dissertation submitted in partial satisfaction
of the requirements for the degree of

Doctor of Philosophy

in

Chemistry

by

Kate Amano Gibson

December 2023

Dissertation Committee:
Dr. Boniface Fokwa, Chairperson
Dr. Chia-en Chang
Dr. Yadong Yin

The Dissertation of Kate Amano Gibson is approved:

_____

_____

_____

Committee Chairperson

University of California, Riverside

Acknowledgments

Some of the research presented in here has previously been published as:

Gibson, K. A.; Küpers, M.; Fokwa, B. P. T., The First Quaternary Phase of the NbRuB Structure Type: Experimental and Computational Investigations of $TiFe_{1.3}Os_{3.9}B_{2.8}$. *Zeitschrift für anorganische und allgemeine Chemie* **2023,** e202300132.

Scheifers, J. P.; Gibson, K. A.; Fokwa, B. P. T., Experimental and computational investigations of TiIrB: a new ternary boride with $Ti_{1+x}Rh_{2-x+y}Ir_{3-y}B_3$-type structure. *Zeitschrift für Naturforschung B* **2021,** *76* (10-12), 727-731.

Other manuscripts that have been published while in the Graduate Program at UC Riverside, but which are not part of the dissertation are listed below:

Pouamo, L. S.; Nguemdzi, C. F. N.; Azam, M.; Luong, D.; Gibson, K. A.; Li, W.; Haddon, E. B.; Fokwa, B. P. T.; Nenwa, J., Two high-spin cobalt(III) complex anions with pyridinium-based cations: synthesis, structural elucidation and magnetic properties. *Journal of Molecular Structure* **2022,** *1266*, 133528.

I would like to thank all of my co-authors, in particular my first co-authors Dr. Jan P. Scheifers and Michael Küpers for their contributions. Additionally, I acknowledge the financial support by UC Riverside and the NSF (Career grant to B.P.T.F., DMR 1654780).

I want to take a moment to thank all of the people who helped me along this journey. First and foremost, I deeply thank my supervisor Dr. Boniface Fokwa for his guidance, mentorship, support, and understanding. In a similar way I express my gratitude to Dr. Leonard Mueller who was my supervisor for the first 2-3 years of the PhD Program. In the Mueller lab I got my first glance of solid-state chemistry, which led me to take Dr.

Fokwa's solid state chemistry class and eventually switch to a solid state research lab. I am utterly thankful to Dr. Boniface Fokwa for accepting me into his research lab halfway through the PhD program. It is thanks to his understanding and flexibility that I was able to work on research projects I was passionate about and have the freedom to do computational and experimental research.

I am also very thankful to my colleagues and former colleagues: Dr. Diana Luong, Johan Yapo, and Sang Bum Kim. I am very thankful to have worked with such wonderful, supportive, passionate people. I also thank lab alumni Dr. Jan Scheifers and Dr. Yuemei Zhang who helped us when we had questions.

I also express my thanks to my family and friends for their continued support throughout the program. I particularly thank Dr. Duy Doan who supported me through the good and tough times. This guy is waiting until I finish working with crystals to give me a crystal.

Finally, I wouldn't have gotten into graduate school without my undergraduate research advisors – Dr. James Seiber, Dr. Dean Tantillo, and Dr. Annaliese Franz. I thank you all for the experiences in your labs and your guidance.

ABSTRACT OF THE DISSERTATION

Combined Computational and Experimental Approach in the Synthesis and Characterization of Magnetic Metal Borides

by

Kate Amano Gibson

Doctor of Philosophy, Graduate Program in Chemistry
University of California, Riverside, December 2023
Dr. Boniface P. T. Fokwa, Chairperson

The combination of computation and experiment is vital to the efficient and thorough study of magnetic materials. Computation allows us to determine the preferred magnetic state of a given model, and techniques including Density of States (DOS) and the Crystal Orbital Hamilton Population (COHP) will explain what orbitals dominate at the fermi energy, and if there are any electronic instabilities. This enables us to efficiently use our time in the experimental lab by predicting novel magnetic materials with Density Functional Theory (DFT) before synthesizing them. The structures discovered were synthesized by arc-melting and further characterized by X-Ray diffraction, Energy Dispersive X-Ray (EDX) analysis, and magnetic measurements.

The quaternary $Hf_2MOs_5B_2$ (M = Mn, Fe, or Co) compositions, belonging to the $Ti_3Co_5B_2$ structure type, were first studied. Magnetic measurements confirmed the DFT predictions that $Hf_2MnOs_5B_2$ and $Hf_2FeOs_5B_2$ exhibit semi-hard and hard-magnetic

behaviors, respectively, with coercivity values of 10.0 kA/m and 49.9 kA/m at 5 K. Prior to this study, all semi-hard and hard magnets of this structure type had a group 9 transition metal. Replacing the group 9 transition metal with osmium illustrates that osmium can also be used to create hard magnets. However, the computational data also illustrated there is the possibility of creating harder magnets by incorporating osmium and a group 9 metal. Based on this knowledge and other recent literature, the compositions $Hf_2MOs_4IrB_2$ and $Hf_2MOs_3Ir_2B_2$ (M = Mn, Fe) were computationally investigated and confirmed the hypothesis that a harder magnet can be obtained by incorporating iridium.

$TiFe_{1.3}Os_{3.9}B_{2.8}$ is the first quaternary composition of the NbRuB structure type, and the third quaternary composition containing titanium, iron, osmium, and boron. Theory predicted a preference for magnetic ordering which was confirmed qualitatively when the material was synthesized. As a result of this magnetic material, the NbRuB structure type, which was previously known for the NbRuB superconductor, is now also of interest for studying magnetism. TiIrB was also synthesized and crystallizes in the $Ti_{1+x}Rh_{2-x+y}Ir_{3-y}B_3$ structure type. Upon synthesis, computation was utilized to understand the electronic structure of this ternary composition containing B_4 zigzag units.

Table of Contents

Chapter 1: Introduction and Computational and Experimental Techniques 1
1.1 Introduction 1
1.2 Introduction to Magnetism 2
1.3 Computational Methods 3
1.3.1 Density of States (DOS) 4
1.3.2 Crystal Orbital Hamilton Population (COHP) 7
1.4 Experimental Techniques 10
1.4.1 Arc-melting 10
1.4.2 Powder X-Ray Diffraction (PXRD) 11
1.4.3 Energy-Dispersive X-Ray (EDX) Analysis 12
1.5 Arrangement of Dissertation 13
1.6 References 15
Chapter 2: Computational and Experimental Investigations of Osmium-Rich Metamagnetic Borides $Hf_2MOs_5B_2$ (M = Mn, Fe, Co) 18
2.1 Abstract 18
2.2 Introduction 19
2.3 Results and Discussion 21
2.3.1 Computational Results and Discussion 21
2.3.2 Experimental Results and Discussion 26
2.4 Conclusion 32
2.5 Methods 33
2.5.1 Experimental Methods 33
2.5.2 Computational Methods 34
2.6 Acknowledgements 35
2.7 References 36
2.8 Supplementary Material 38
2.9 Supplementary Material References 43
Chapter 3: Rare-Earth-free Magnets of the $Ti_3Co_5B_2$ structure type $Hf_2MOs_4IrB_2$ and $Hf_2MOs_3Ir_2B_2$ (M = Mn, Fe) 44
3.1 Abstract 44
3.2 Introduction 44
3.3 Results and Discussion 47
3.3.1 Experimental 47
3.3.2 Computational Analysis 50
3.4 Conclusion 50
3.5 Methods 51
3.5.1 Experimental Methods 51
3.5.2 Computational Methods 52
3.6 Acknowledgements 53
3.7 References 54
3.8 Supplementary Material 56

Chapter 4: The First Quaternary Phase of the NbRuB Structure Type: Experimental and Computational Investigations of $TiFe_{1.3}Os_{3.9}B_{2.8}$ 60
Kate A. Gibson, Michael Küpers, Dr. Boniface P. T. Fokwa 60
4.1 Abstract 60
4.2 Introduction 60
4.3 Results and Discussion 63
4.3.1 X-ray diffraction and structure analysis 63
4.3.2 Electronic structure, chemical bonding, and magnetism 69
4.4 Conclusions 74
4.5 Experimental Section 74
4.5.1 Synthesis and Characterization 74
4.5.2 Computational methods 75
4.6 References 77
4.7 Supporting Information 79
Chapter 5: Experimental and computational investigations of TiIrB: a new ternary boride with $Ti_{1+x}Rh_{2-x+y}Ir_{3-y}B_3$-type structure 87
5.1 Abstract 87
5.2 Introduction 87
5.3 Results and discussion 89
5.3.1 Phase analysis and structure refinement 89
5.3.2 Electronic structure 94
5.4 Conclusions 97
5.5 Experimental section 97
5.5.1. Synthesis of TiIrB 97
5.5.2. Computational methods 98
5.6 References 99
Chapter 6: Conclusion 101

List of Tables

Table 2.1. VASP Total Energies for the different magnetic models relative to the lowest energy model, and Exchange Energy ($E_{EX} = E_{AFM} - E_{FM}$) and Spin-Orbit Coupling Energy (E_{SOC}) for the ferromagnetic models. (VEC = valence electron count, FM = ferromagnetic, AFM = antiferromagnetic, NM = nonmagnetic). 23
Table 2.2. Rietveld refinement data of the $Hf_2MOs_5B_2$ (M = Mn, Fe, Co) phases, and lattice parameters of the corresponding lowest energy computational model. 28
Table S2.1. Calculated spin orbit coupling energy (E_{SOC}), exchange energy (E_{EX}), magnetic moment (M_{th}), and experimental magnetic quantities [coercivity (H_c) at 5 K, magnetic moment (M), Néel temperature (T_N), and Curie temperature (T_C)] for various $Ti_3Co_5B_2$-type phases. VEC = valence electrons count. 38
Table 3.1. Rietveld refinement data of the $Hf_2MOs_4IrB_2$ and $Hf_2MOs_3Ir_2B_2$ (M = Mn, Fe) phases, and lattice parameters of the corresponding lowest energy computational model. 48
Table S3.1. Total Energies for the different magnetic models relative to the lowest energy (FM = ferromagnetic, AFM = antiferromagnetic, NM = nonmagnetic). 56
Table 4.1. Single-crystal refinement results for $TiFe_{1.3}Os_{3.9}B_{2.8}$. 66
Table 4.2. Wyckoff sites, fractional coordinates, occupancy, and equivalent (isotopic for boron) displacement parameters for $TiFe_{1.3}Os_{3.9}B_{2.8}$. 67
Table S4.1. Results of the Rietveld refinement for $TiFe_{1.3}Os_{3.9}B_{2.8}$ and elemental osmium corresponding to the Powder X-Ray Diffractogram (PXRD) in Figure S4.2. 79
Table S4.2. Selected distances in $TiFe_{1.3}Os_{3.9}B_{2.8}$ 80
Table S4.3. Anisotropic displacement parameters (in $Å^2$) for $TiFe_{1.3}Os_{3.9}B_{2.8}$. $U_{12} = U_{23} = 0$ 81
Table S4.4. Energy dispersive X-ray (EDX) results of the metals content for $TiFe_{1.3}Os_{3.9}B_{2.8}$. 81
Table S4.5. Selected experimental ($d$exp, Å) and theoretical (dth, Å) bond distances in $TiFeOs_4B_3$, and the corresponding pICOHP values (eV). 82
Table S4.6. Lattice parameters [Å] and B_2 bond distances [Å] for $TiFe_{1.3}Os_{3.9}B_{2.8}$ (d_{exp}), theoretical (antiferromagnetic model) $TiFeOs_4B_3$ (d_{th}), theoretical (antiferromagnetic model) $TiFeOs_4B_3$ with B2 distance fixed at the single crystal B_2 distance (d_{th}/fixed B_2), and the NbRuB structure. 83
Table 5.1. Details of the Rietveld refinement for TiIrB sample. 91
Table 5.2. Atomic coordinates from PXRD experiments and DFT calculations and site occupation factors (SOF) for TiIrB. 92
Table 5.3. Experimental interatomic distances (Å) around the boron atoms in TiIrB obtained from Rietveld refinement. 93

List of Figures

Figure 1.1 Temperature versus inverse magnetic susceptibility for different substances.[3] 3
Figure 1.2 Molecular orbitals in different systems with arbitrary atoms.[4] 5
Figure 1.3 Band width of an arbitrary set of p-orbitals.[4] 6
Figure 1.4 DOS and -COHP curves of the nonmagnetic 3d transition metals.[6] 8
Figure 1.5. DOS and -COHP of ferromagnetic iron.[5, 6, 8] 9
Figure 1.6 Fokwa Lab Arc melting apparatus.[9] 10
Figure 1.7. The different stages of Powder X-Ray Diffraction (PXRD) structure determination.[11] 12
Figure 2.1. (a) Structure of $Hf_2MOs_5B_2$ (M = Mn, Fe, or Co) and (b) the two magnetic models based on ferromagnetic chains of M. 21
Figure 2.2. Non-spin-polarized (left) and spin-polarized (right) density of state curves of $Hf_2FeOs_5B_2$. Insets represent the zoom in around E_F (between -0.2 and 0.2 eV)..... 23
2.3.2 Experimental Results and Discussion 26
Figure 2.3. Rietveld refinement plot showing observed (black) fitted with calculated (red) powder X-ray diffraction patterns of $Hf_2MnOs_5B_2$. The positions of the Bragg reflections are given in green for $Hf_2MnOs_5B_2$ (top row), Os (middle row), and HfO_2 - *P 21/c* (bottom row). Difference curve (blue) obtained from Rietveld refinement. 29
Figure 2.4. Low-temperature ZFC/FC magnetization curves at 0.01 T (left) and ZFC magnetization curve at 1 T (right) for $Hf_2MnOs_5B_2$. 31
Figure 2.5. Low-temperature ZFC/FC magnetization curves at 0.01 T for $Hf_2FeOs_5B_2$ (left) and $Hf_2CoOs_5B_2$ (right)..... 31
Figure S2.3. Rietveld refinement plot showing observed (black) fitted with calculated (red) powder X-ray diffraction patterns of $Hf_2FeOs_5B_2$. The positions of the Bragg reflections are given in green for $Hf_2MnOs_5B_2$ (top row), Os (middle row), and HfO_2 - *P 21/c* (bottom row). Difference curve (blue) obtained from Rietveld refinement. 40
Figure S2.5. SEM image (top left) and EDX spectrum (bottom left) and elemental mapping (right) of $Hf_2MnOs_5B_2$. 41
Figure S2.6. SEM image (top left) and EDX spectrum (bottom left) and elemental mapping (right) of $Hf_2FeOs_5B_2$. 41
Figure S2.7. SEM image (top left) and EDX spectrum (bottom left) and elemental mapping (right) of $Hf_2CoOs_5B_2$. 42
Figure S2.8. Low-temperature ZFC magnetization curve at 1 T (right) for $Hf_2CoOs_5B_2$. 42
Figure S2.9. Hysteresis plot (at 5 K, left) and magnetization versus magnetic field at different temperatures (right) for $Hf_2CoOs_5B_2$. The hysteresis is likely due to a ferromagnetic impurity. 43
Figure 3.1. Observed (black) and calculated (red) powder X-ray diffraction pattern with starting stoichiometry $Hf_2MnOs_4IrB_2$ with boron 120%. The position of the Bragg reflections (green): $Hf_2MnOs_4IrB_2$ (top row) and Os (bottom row). Difference curve (blue) obtained from Rietveld refinement..... 49
Figure 3.2. EDX spectrum and elemental mapping of $Hf_2MnOs_4IrB_2$ 49

Figure S3.1. The three computational models of $Hf_2FeOs_3Ir_2B_2$. 56
Figure S3.2. Illustration of the magnetic models using ferromagnetic chains of Fe. 56
Figure S3.3. Observed (black) and calculated (red) powder X-ray diffraction pattern with starting stoichiometry $Hf_2FeOs_4IrB_2$ with boron 120%. The position of the Bragg reflections (green): $Hf_2FeOs_4IrB_2$ (top row) and Os (bottom row). Difference curve (blue) obtained from Rietveld refinement. 57
Figure S3.4. Observed (black) and calculated (red) powder X-ray diffraction pattern with starting stoichiometry $Hf_2FeOs_3Ir_2B_2$ with boron 120%. The position of the Bragg reflections (green): $Hf_2FeOs_3Ir_2B_2$ (top row) and Os (bottom row). Difference curve (blue) obtained from Rietveld refinement..... 57
Figure S3.5. Observed (black) and calculated (red) powder X-ray diffraction pattern with starting stoichiometry $Hf_2MnOs_3Ir_2B_2$ with boron 120%. The position of the Bragg reflections (green): $Hf_2MnOs_3Ir_2B_2$ (top row) and Os (bottom row). Difference curve (blue) obtained from Rietveld refinement..... 58
Figure S3.6. EDX spectrum and elemental mapping of $Hf_2FeOs_4IrB_2$ 58
Figure S3.7. EDX spectrum and elemental mapping of $Hf_2FeOs_3Ir_2B_2$ 59
Figure S3.8. EDX spectrum and elemental mapping of $Hf_2MnOs_3Ir_2B_2$..... 59
Figure 4.1. Projected crystal structure of TiFe1.3Os3.9B2.8 as obtained from single-crystal refinement..... 67
Figure 4.2. Coordination polyhedra around the Fe4 (left) and Ti3/Os3 (right) sites in the crystal structure of $TiFe_{1.3}Os_{3.9}B_{2.8}$. 68
Figure 4.3. Total (black) and partial (colored) non-spin polarized (left) and spin-polarized (right) density of states (DOS) plots for a unit cell of $TiFeOs_4B_3$. Fermi energy (E_F, black line) set at 0 eV, the red dashed line is the projected E_F of the experimental composition. 70
Figure 4.4. Non-spin polarized (left) and spin polarized (right) -pCOHP curves for intrachain Fe−Fe interaction in $TiFeOs_4B_3$. Fermi energy (E_F, black line) set at 0 eV, the red dashed line is the projected E_F of the experimental composition. 73
Figure S4.1. Powder X-ray Diffractogram consisting of NbRuB structure type (red), $Ti_{1+x}Rh_{2-x+y}Ir_{3-y}B_3$ structure type (blue), elemental osmium (green), and unidentified peaks (arrows). 83
Figure S4.2. Observed (black) and calculated (red) powder X-ray diffraction pattern with starting stoichiometry $TiFe_{1.5}Os_{3.5}B_3$. The position of the Bragg reflections (green): $TiFe_{1.3}Os_{3.9}B_{2.8}$ (top row) and Os (bottom row). The difference curve (blue) obtained from Rietveld refinement. 84
Figure S4.3. Energy dispersive X-ray (EDX) spectrum (left) of $TiFe_{1.3}Os_{3.9}B_{2.8}$ and an electron micrograph of the analyzed single crystal (right)..... 84
Figure S4.4. Structure models (non-spin polarized) and their relative energies for $TiFeOs_4B_3$ showing the different Ti and Os positions derived from the experimentally determined mixed occupied Os:Ti (50:50) site (4j). 85
Figure S4.5. Total (black) and partial (colored) non-spin polarized DOS (left) for the unit cell of $TiFeOs_4B_3$..... 85

Figure S4.6. Magnetic models for $TiFeOs_4B_3$ based on the most favorable structure model from Figure S3.4. Energy differences are relative to the AFM ground state. Intrachain and interchain Fe-Fe distances given in Å..... 86
Figure S4.7. Projected COHP (pCOHP) curves for Os-Os interactions in $TiFeOs_4B_3$..... 86
Figure 5.1. Observed (black) and calculated (red) powder X-ray diffraction pattern of TiIrB; the position of the Bragg reflections (green) for TiIrB (top row), TiB_2 (second row), $TiIr_3$ (third row), and of TiIr (bottom row); the difference curve (blue) obtained from Rietveld refinement..... 90
Figure 5.2. Projected structure of TiIrB ($Ti_{1+x}Rh_{2-x+y}Ir_{3-y}B_3$ type) as obtained from Rietveld refinement..... 92
Figure 5.3. Total and partial density of states (DOS) plots for TiIrB..... 95
Figure 5.4. Partial density of states (DOS) plots for the lone boron atoms and the B_4 zigzag boron fragments..... 96

Chapter 1

Introduction and Computational and Experimental Techniques

1.1 Introduction

There have been many challenges in the field of solid state chemistry. Many of the challenges that were apparent in the 1990s remain today, particularly predicting novel structures and the lack of knowledge on the mechanisms which form these materials.[1] There has been a flourishing amount of machine learning research that will eventually, and ideally, make these challenges minimal. However, the current machine learning methods geared towards materials are still in their infancy as they are quite basic and utilize small training sets.[2] One of the biggest challenges in machine learning for specifically materials research is the reliance on the amount and quality of experimental data available.[2] In a field where many of the novel structures continues to be discovered by means of replacing one or two elements in a composition with similar elements, and the synthetic conditions necessary to make novel compounds is largely unknown, we are still in a decade where most novel structures are obtained in the same manner as the studies in this dissertation – with the combination of computation and experiment.[1] Experiment can help us identify the structure, composition, and magnetic properties of a novel material. But what interactions are occurring on the molecular level that make something favor the ferromagnetic state over the non-magnetic state? Some questions,

like this, can be answered computationally. This chapter will briefly discuss many of the techniques used in this dissertation to identify and understand magnetic materials.

1.2 Introduction to Magnetism

Magnetism is most commonly associated with elements in the d and f block of the periodic table, as these elements generally have unpaired electrons.[3] These unpaired electrons are able to generate a magnetic moment from the spin and orbital motion.[3] If the unpaired electrons are oriented randomly, it is a paramagnetic substance. If the unpaired electrons are all pointing in the same direction, the material is a ferromagnet. If the unpaired electrons are aligned antiparallel with equal numbers, which would give a net magnetic moment of zero, the material is antiferromagnetic. If the unpaired electrons are aligned antiparallel but unequally, giving rise to a non-zero magnetic moment, then the material is ferrimagnetic.[3]

Magnetic susceptibility (χ) is the ratio of magnetization or magnetic moment of the sample (M) to the field (H). The magnetic susceptibility of a material is the main parameter used for the characterization of a material's magnetic properties.[3]

$$\chi = \frac{M}{H} \quad \text{(Eqn. 1.1)}^{3}$$

Magnetic materials can also have magnetization that is temperature-dependent. The temperature above which materials lose their ordered magnetization is called the Curie temperature (T_C) for ferro- and ferrimagnets, or the Neel temperature (T_N) for antiferromagnets.[3] The Curie-Weiss law is stated in Equation 1.2 where C is the Curie

constant, T is the temperature, and θ is the Weiss constant. This relationship is also described in Figure 1.1 which illustrates what kind of Weiss constants would be expected for different types of materials.

$$\chi = \frac{C}{T-\theta} \text{ (Eqn. 1.2)}^{3}$$

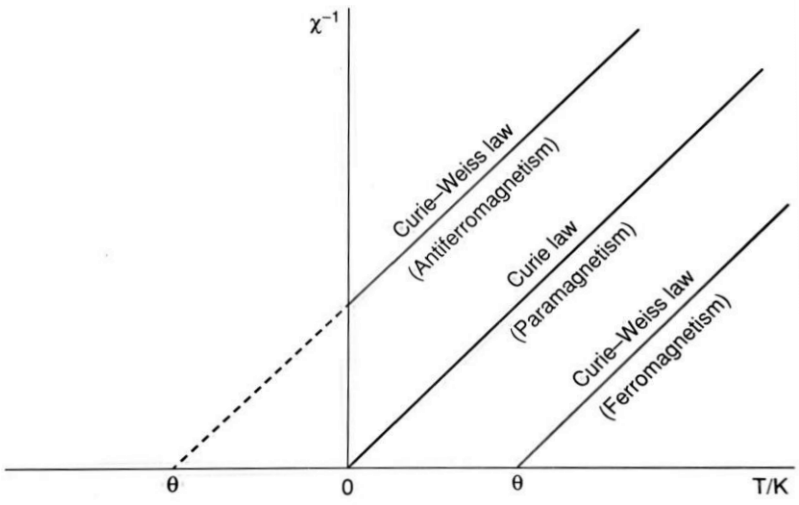

Figure 1.1 Temperature versus inverse magnetic susceptibility for different substances.[3]

1.3 Computational Methods

Density Functional Theory (DFT) is a computational technique utilized across many disciplines for a variety of purposes. In the field of solid state one of the most useful applications of DFT is to determine if a particular structure and composition is worth studying experimentally. It is highly inefficient to go into the lab and try to synthesize a magnet if DFT would show us it favors a non-magnetic state. DFT allows the prevention of "wasted time" by seeing if a desired material is worth pursuing – in our case, will this new material likely be magnetic? After the novel material is synthesized, DFT is then used to understand the interactions occurring on the molecular level to better

understand the material. Although some researchers would say that synthesizing the novel material is enough, and computation is a “add-on”, this approach isn’t very helpful in the long-term. When thinking about the periodic table, most elements were first discovered, studied to understand their properties, and then applied. This research lab focuses primarily on the first two steps for materials research – the discovery and understanding of novel materials. If another researcher down the road desires to make a magnet on an industrial scale, then they will build off materials they know with promising properties. Utilizing computation allows us to understand these properties. A brief, qualitative introduction to computational and experimental techniques is provided in the following sections.

1.3.1 Density of States (DOS)

The Density of States (DOS) is best understood if we start at the beginning. If we look at a chain of hydrogen atoms that are equally spaced apart, the lowest energy system would be where there are no nodes while the highest energy system would have the most nodes. In chemistry, we would refer to these energy levels using molecular orbital theory.

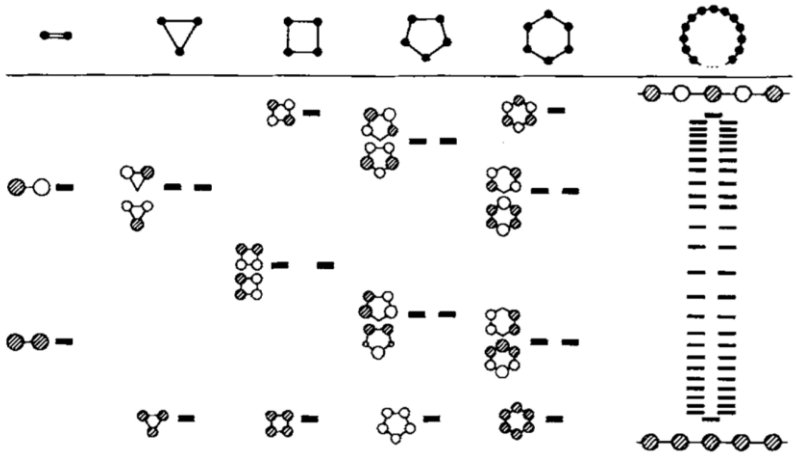

Figure 1.2 Molecular orbitals in different systems with arbitrary atoms.[4]

In Figure 1.2, we can see this trend for any system – the more nodes the higher the energy. What happens when there are so many energy levels, though, like the system at the right of Figure 1.2? Without going into details, what a chemist will draw as a series of molecular orbitals, in physics is represented by the energy as a function of k, where $0 \leq k \leq \pi/a$ and a is the spacing between neighboring atoms.[4] This is illustrated in Figure 1.3 where the lowest energy, at $k = \pi/a$, is the bonding orbital (no nodes) and the highest energy, at $k = 0$, is the highest antibonding orbital (the most nodes).

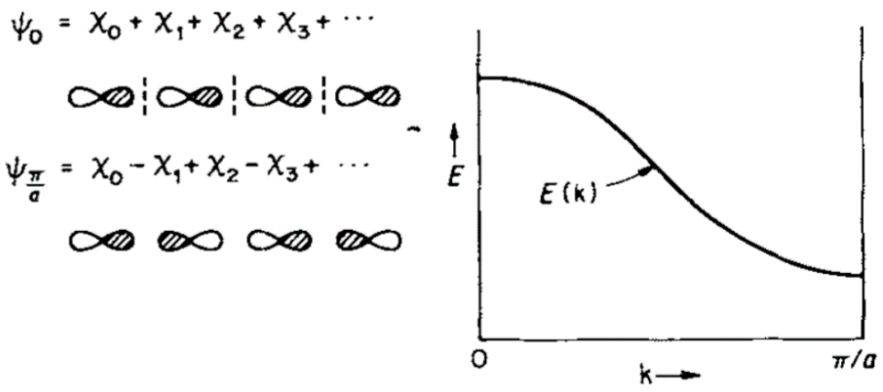

Figure 1.3 Band width of an arbitrary set of p-orbitals.[4]

The Density of States (DOS) is proportional to the inverse of the slope of E(k) versus k.[4, 5] The DOS helps us understand solids because unlike in basic molecules, where we can more simply identify the HOMO or LUMO, solids are a lot more complex.[4] Instead of looking at one orbital at an energy level, the DOS allows us to view a group of energy levels within an energy interval.[4] The integrated DOS up to the Fermi Energy (E_F) are the occupied molecular orbitals.[4] In our studies, the DOS is used primarily to identify if the magnetic state is favorable over the nonmagnetic state. That is, when the E_F lies on a peak it is an indicator of structural instability. For the structures in this dissertation, we see the E_F lying in a pseudo-gap, or on a much smaller peak, after magnetization which would indicate increased structural stability as a result of magnetism. The reasoning for this is discussed in the COHP section.

1.3.2 Crystal Orbital Hamilton Population (COHP)

The Crystal Orbital Hamilton Population (COHP) builds off the DOS. While the DOS will indicate in which orbitals the electrons are, the COHP will help in determining if these electrons are in a bonding or antibonding orbital.[4] The integrated COHP (ICOHP) will also provide the relative bond strength.[6] The COHP is often plotted alongside the DOS so one can identify what is contributing the most electron density at the fermi energy (DOS), and whether those are in bonding or antibonding orbitals (COHP). If the COHP indicates a large amount of antibonding at the fermi energy, then it would indicate instability. This instability is sometimes structural, but it can also be due to the magnetic state of the model. Many studies, particularly those associated with Hoffman and Dronskowski, have determined a pattern for the nonmagnetic COHPs of the 3d transition metals (Figure 1.4).

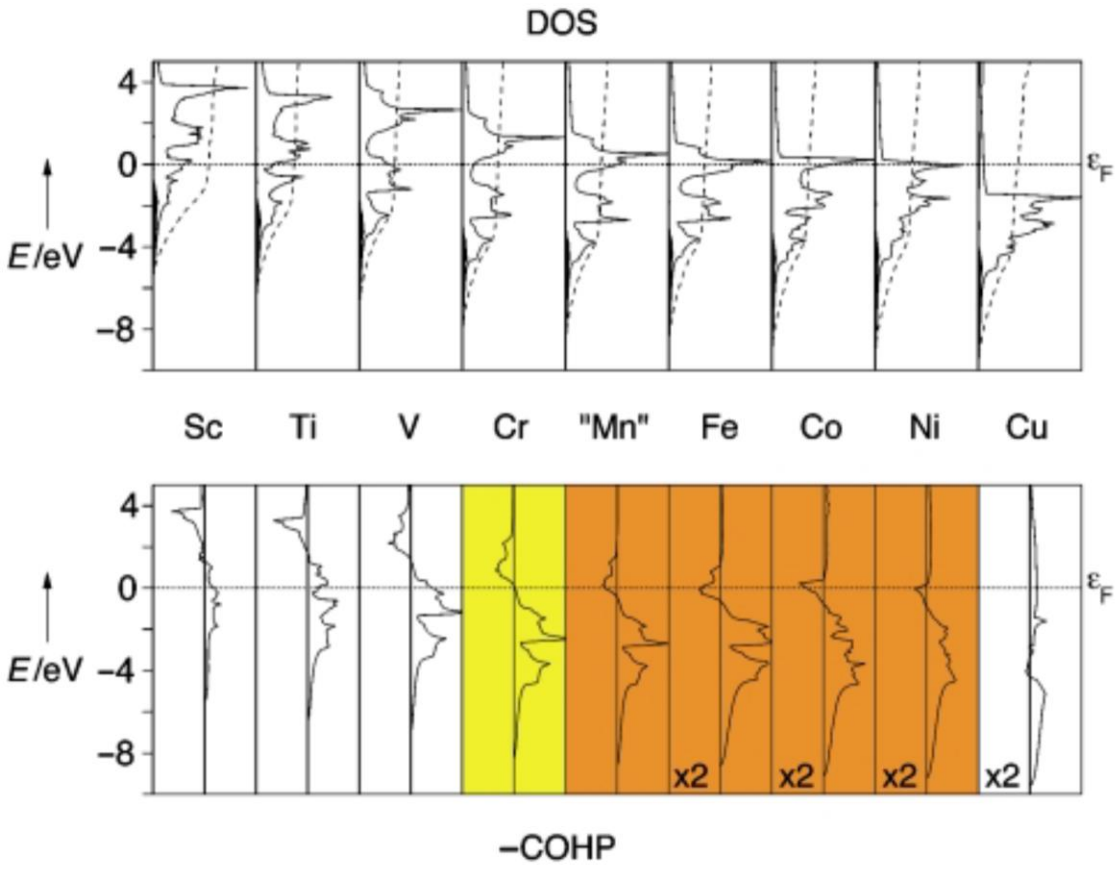

Figure 1.4 DOS and -COHP curves of the nonmagnetic 3d transition metals.[6]

Many of the studies in this dissertation will deal with Fe-Fe interactions and magnetism, so iron will be utilized in this explanation. As seen in Figure 1.4, the Fe-Fe nonmagnetic -COHP places the fermi energy in the antibonding region. In a -COHP, anything to the left of zero is antibonding while anything to the right is considered bonding. As with a molecular orbital interpretation, electrons in antibonding orbitals indicate instability. Previous studies have determined that when the nonmagnetic -COHP of a 3d transition metal lies in the antibonding region at the fermi energy it indicates ferromagnetism. When the fermi energy lies between the bonding and antibonding states

like in chromium, this would suggest an antiferromagnetic system. And when the fermi energy is in the bonding region, there is no drive towards ferromagnetism.[5-7]

What we see in the cases of magnetic elements is instead of the instability being structural, it is magnetic. That is, instead of the atoms needing to rearrange themselves, the electrons rearrange themselves.[4, 7] Upon magnetizing the iron atoms into a ferromagnetic state, we obtain the following DOS and -COHP (Figure 1.5). As can be seen, the fermi energy no longer lies in an antibonding region of the -COHP, indicating increased stability. Some of the studies in this dissertation graph DOS and -COHP together, while others extrapolate the structural stability from the Fe-Fe DOS. This is due to the Fe-Fe nonmagnetic and ferromagnetic DOS having a character that is in-line with these previous studies.

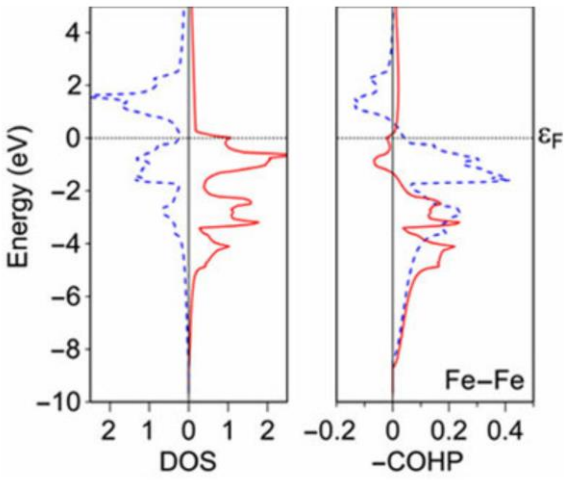

Figure 1.5. DOS and -COHP of ferromagnetic iron.[5, 6, 8]

1.4 Experimental Techniques

1.4.1 Arc-melting

Figure 1.6 Fokwa Lab Arc melting apparatus.[9]

Our lab's arc melting apparatus, shown in Figure 1.6, is home made by our lab alumni. The sample pellet is placed into the water-cooled copper crucible, and the chamber is vacuumed to ensure nothing can react with the elements in the sample. Argon is then allowed to fill the chamber, before turning on the electrode which ionizes the argon gas to create an arc that will bring the sample to ~3,000 ˚C. This method is used to obtain materials that require a high temperature in order to form the products. While the sample is heated in the arc, a solution is formed where the free elemental atoms are able to move and create new bonds. Upon the sample cooling, the novel material is synthesized. Details are given in the experimental section of the following chapters.

1.4.2 Powder X-Ray Diffraction (PXRD)

Single Crystal X-Ray Diffraction (SCXRD) is often used when identifying a novel material's unit cell. Although SCXRD can give much structural information, the need for a high-quality crystal can sometimes make it difficult to characterize the novel material.[10, 11] This is particularly the case when the novel material is a minor phase and thus, SCXRD is generally only used when the desired, novel phase is a high purity. Powder X-Ray Diffraction (PXRD) is often utilized to ensure a high purity of the novel phase before one starts picking crystals for SCXRD. In cases where materials can not be synthesized in the form of single crystals, PXRD can be used to characterize the novel phase.[11] In a PXRD diffraction pattern, the positions of the peaks depend on the dimensions of the unit cell while the intensities of the peaks are correlated with the atoms or ions in the unit cell.[3, 11] The general way a structure is determined from PXRD can be illustrated in the following diagram.

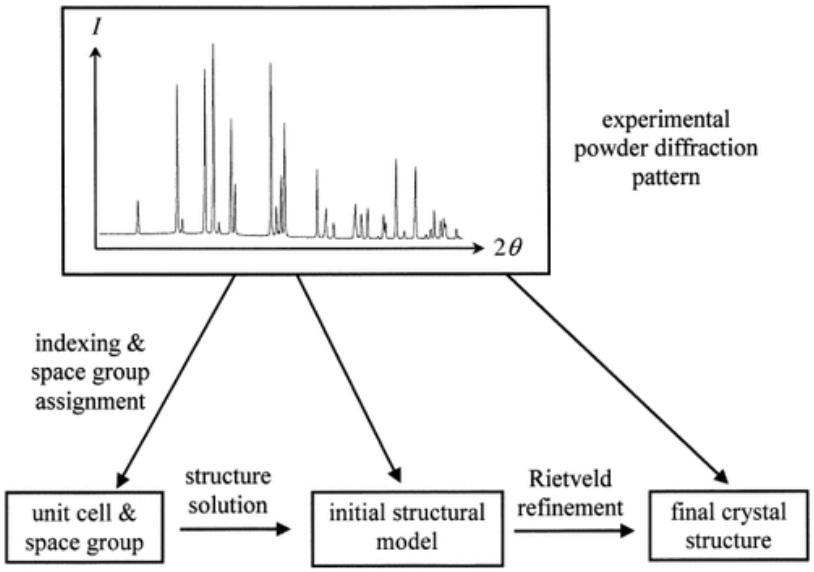

Figure 1.7. The different stages of Powder X-Ray Diffraction (PXRD) structure determination.[11]

For the studies in this dissertation, SCXRD is done to obtain the unit cell, space group, and the initial structural model. Rietveld refinement is then done on the initial structural model to determine the composition of the novel material. In the case of TiIrB and $Hf_2M_xOs_{5-x}B_2$ (M = Fe, Mn, or Co) the initial structural models were already known from prior studies, so only PXRD was necessary to identify the novel composition. For $TiFe_{1.3}Os_{3.9}B_{2.8}$, an initial structure was not known and so SCXRD was essential to the discovery of the novel phase.

1.4.3 Energy-Dispersive X-Ray (EDX) Analysis

In EDX, X-Rays are generated according to the elements present in the sample which allows for not only the detection of the element, but also the concentration of the elements in the sample.[12] The EDX done on $TiFe_{1.3}Os_{3.9}B_{2.8}$ was with point analysis on a

single crystal. This method allows for the ratio of the elements at each particular point of the crystal to be determined. In contrast, the EDX on the $Ti_3Co_5B_2$ structures were done on powders and a mapping analysis was done. Elemental mapping allows for a more visual analysis of the elements in a certain area and provides the ratio of the elements in the area. Qualitatively, we can confirm the elements are spread evenly throughout the sample which would point toward a uniform material as opposed to areas that have elemental powders. Quantitatively, the ratios can be used to confirm the elemental stoichiometric ratios and also guide the SCXRD refinement. For all the EDX conducted in this dissertation, plots of energy versus intensity are provided which indicate the presence of particular elements as each metal has a characteristic spectrum.[13]

1.5 Arrangement of Dissertation

Boron is an electron deficient element that is capable of bonding with a variety of other elements to form different materials.[14, 15] The strong covalent bonding between adjacent boron atoms, and in metal-boron bonds, gives rise to desirable properties including high melting points, chemical inertness, and wear resistance.[15] The variety of applications of metal borides is vast, including magnetism, electrical conductors, and having good conductivity.[14] A few examples of metal borides include $Nd_2Fe_{14}B$[14, 15] which is the strongest permanent magnet to date, YB_{66}[14, 15] which is used for synchrotron radiation, and MgB_2[15] the first high-temperature metallic superconductor. This dissertation focuses on transition metal borides (TMBs). TMBs have been an exciting area of research due to their desirable properties including high thermal and chemical

stability, and magnetism.[14] The following focuses on the structure types of the materials in this dissertation.

The first structure type encountered in this dissertation is the NbRuB structure type which contains B_2 dumbells in double trigonal prisms and isolated boron atoms in trigonal prisms.[16-18] $TiFe_{1.3}Os_{3.9}B_{2.8}$, presented in chapter two, is the first quaternary phase of the NbRuB structure type.[19] Computational studies have shown NbRuB to be a ductile and hard material and a possible superconductor[20, 21]. Another structure of the NbRuB structure type is TaRuB which was found to be Pauli paramagnetic.[16] However, TaRuB also synthesizes in the $Ti_{1+x}Rh_{2-x+y}Ir_{3-y}B_3$ structure type.[16] In chapter three TiIrB is discussed which belongs to the $Ti_{1+x}Rh_{2-x+y}Ir_{3-y}B_3$ structure type.[22] The $Ti_{1+x}Rh_{2-x+y}Ir_{3-y}B_3$ structure includes zigzag B_4 fragments.[22, 23] The most recent discovery of this structure type is the $Ti_2FeOs_3B_3$ ferromagnet (submitted). LT-NbOsB, which also belongs to the $Ti_{1+x}Rh_{2-x+y}Ir_{3-y}B_3$ structure type and is a potential superconductor, has Nb occupying the Ti and Rh positions, and Os occupying the Ir positions.[24] The final two chapters discuss various novel compositions of the $Ti_3Co_5B_2$ structure type. The $Ti_3Co_5B_2$ structure type has given rise to a variety of materials with useful properties: the soft magnetic $Ti_2FeRh_5B_2$, the semihard magnet $Ti_2FeRu_4RhB_2$, and the hard magnet $Sc_2FeRu_3Ir_2B_2$. There are at least seven structures of the $Ti_3Co_5B_2$ structure type, many of which exhibit some form of magnetic properties.[25] This dissertation adds seven more structures to the $Ti_3Co_5B_2$ structure type, many of which also exhibit magnetic properties.

1.6 References

1. DiSalvo, F. J., Solid-State Chemistry: a Rediscovered Chemical Frontier. *Science* **1990,** *247* (4943), 649-655.

2. Schmidt, J.; Marques, M. R. G.; Botti, S.; Marques, M. A. L., Recent advances and applications of machine learning in solid-state materials science. *npj Computational Materials* **2019,** *5* (1), 83.

3. West, A. R., *Solid state chemistry and its applications*. Second edition, student edition ed.; John Wiley & Sons, Ltd. Chichester, West Sussex: Chichester, West Sussex, 2014.

4. Hoffmann, R., How Chemistry and Physics Meet in the Solid State. *Angewandte Chemie International Edition in English* **1987,** *26* (9), 846-878.

5. Aechen, R. Theory: From H2 to Data-Storage Alloys. http://www.cohp.de/ (accessed April).

6. Landrum, G. A.; Dronskowski, R., The Orbital Origins of Magnetism: From Atoms to Molecules to Ferromagnetic Alloys. *Angewandte Chemie International Edition* **2000,** *39* (9), 1560-1585.

7. Dronskowski, R.; Hoffman, R., *Computational Chemistry of Solid State Materials*. WILEY-VCH: Germany, 2008.

8. Dronskowski, R.; Korczak, K.; Lueken, H.; Jung, W., Chemically Tuning between Ferromagnetism and Antiferromagnetism by Combining Theory and Synthesis in Iron/Manganese Rhodium Borides. *Angewandte Chemie International Edition* **2002,** *41* (14), 2528-2532.

9. Luong, D. Exploring Magnetism in Metal-Rich Borides: Synthesis, Characterization, and Magnetic Properties. University of California, Riverside, 2023.

10. Dudenko, D. V.; Williams, P. A.; Hughes, C. E.; Antzutkin, O. N.; Velaga, S. P.; Brown, S. P.; Harris, K. D. M., Exploiting the Synergy of Powder X-ray Diffraction and Solid-State NMR Spectroscopy in Structure Determination of Organic Molecular Solids. *The Journal of Physical Chemistry C* **2013,** *117* (23), 12258-12265.

11. Harris, K. D. M.; Tremayne, M.; Kariuki, B. M., Contemporary Advances in the Use of Powder X-Ray Diffraction for Structure Determination. *Angewandte Chemie International Edition* **2001,** *40* (9), 1626-1651.

12. Raval, N.; Maheshwari, R.; Kalyane, D.; Youngren-Ortiz, S. R.; Chougule, M. B.; Tekade, R. K., Chapter 10 - Importance of Physicochemical Characterization of Nanoparticles in Pharmaceutical Product Development. In *Basic Fundamentals of Drug Delivery*, Tekade, R. K., Ed. Academic Press: 2019; pp 369-400.

13. Quadri, T. W.; Fayemi, O. E.; Olasunkanmi, L. O.; Ebenso, E. E., Chapter 15 - Survey of different electrochemical and analytical techniques for corrosion measurements. In *Electrochemical and Analytical Techniques for Sustainable Corrosion Monitoring*, Aslam, J.; Verma, C.; Mustansar Hussain, C., Eds. Elsevier: 2023; pp 293-323.

14. Joshi, R.; Ningthoujam, R. S., Synthesis, Characterization, Physical Properties and Applications of Metal Borides. In *Handbook on Synthesis Strategies for Advanced Materials: Volume-III: Materials Specific Synthesis Strategies*, Tyagi, A. K.; Ningthoujam, R. S., Eds. Springer Singapore: Singapore, 2021; pp 251-305.

15. Scheifers, J. P.; Zhang, Y.; Fokwa, B. P. T., Boron: Enabling Exciting Metal-Rich Structures and Magnetic Properties. *Accounts of Chemical Research* **2017,** *50* (9), 2317-2325.

16. Mbarki, M.; Touzani, R. S.; Rehorn, C. W. G.; Gladisch, F. C.; Fokwa, B. P. T., New ternary tantalum borides containing boron dumbbells: Experimental and theoretical studies of Ta2OsB2 and TaRuB. *Journal of Solid State Chemistry* **2016,** *242*, 28-33.

17. Mbarki, M.; Touzani, R. S.; Fokwa, B. P. T., Experimental and Theoretical Investigations of the Ternary Boride NbRuB with a Layerlike Structure Type. *European Journal of Inorganic Chemistry* **2014,** *2014* (8), 1381-1388.

18. Iyer, A. K.; Zhang, Y.; Scheifers, J. P.; Fokwa, B. P. T., Structural variations, relationships and properties of M2B metal borides. *Journal of Solid State Chemistry* **2019,** *270*, 618-635.

19. Gibson, K. A.; Küpers, M.; Fokwa, B. T. P., The First Quaternary Phase of the NbRuB Structure Type: Experimental and Computational Investigations of TiFe1.3Os3.9B2.8. *Zeitschrift für anorganische und allgemeine Chemie* **2023,** *n/a* (n/a), e202300132.

20. Xie, W.; Luo, H.; Baroudi, K.; Krizan, J. W.; Phelan, B. F.; Cava, R. J., Fragment-Based Design of NbRuB as a New Metal-Rich Boride Superconductor. *Chemistry of Materials* **2015,** *27* (4), 1149-1152.

21. Tian, W.; Chen, H., Insight into the mechanical, thermodynamics and superconductor properties of NbRuB via first-principles calculation. *Sci Rep* **2016,** *6* (1), 19055.

22. Scheifers, J. P.; Gibson, K. A.; Fokwa, B. P. T., Experimental and computational investigations of TiIrB: a new ternary boride with Ti1+x Rh2−x+y Ir3−y B3-type structure. *Zeitschrift für Naturforschung B* **2021,** *76* (10-12), 727-731.

23. Goerens, C.; Fokwa, B. P. T., The complex metal-rich boride Ti1+xRh2−x+yIr3−yB3 (x=0.68, y=1.06) with a new structure type containing B4 zigzag fragments: Synthesis, crystal chemistry and theoretical calculations. *Journal of Solid State Chemistry* **2012,** *192*, 113-119.

24. Zheng, Q.; Gumeniuk, R.; Rosner, H.; Schnelle, W.; Prots, Y.; Burkhardt, U.; Grin, Y.; Leithe-Jasper, A., Synthesis, crystal structure and properties of the new superconductors TaRuB and NbOsB. *J. Phys.: Condens. Matter* **2015,** *27* (41), 415701.

25. Zhang, Y.; Miller, G. J.; Fokwa, B. P. T., Computational Design of Rare-Earth-Free Magnets with the Ti3Co5B2-Type Structure. *Chemistry of Materials* **2017,** *29* (6), 2535-2541.

Chapter 2

Computational and Experimental Investigations of Osmium-Rich Metamagnetic Borides $Hf_2MOs_5B_2$ (M = Mn, Fe, Co)

Kate A. Gibson, Diana Luong, Paul G. Issac, Lars Schumacher, Rainer Pöttgen, Boniface P. T. Fokwa

2.1 Abstract

The new metal borides, $Hf_2MOs_5B_2$ (M = Mn, Fe, Co), which are the first Os-rich quaternary variants of the prolific $Ti_3Co_5B_2$ structure type, were investigated experimentally and computationally. In their crystal structures osmium builds a network of prisms, in which the other elements are located. The magnetic M elements are found in face-connected tetragonal Os_8-prisms leading to M-chains with intra- and inter-chain distances of about 3.0 and 6.5 A, respectively. Density Functional Theory (DFT) showed that magnetic ordering is hugely favored for M = Mn and Fe, but only slightly favored for M = Co. Experimental investigations then confirmed and extended the DFT predictions as a metamagnetic behavior was found for all phases, whereby all show dominating antiferromagnetic interactions (T_N = 19 - 90 K) are low magnetic fields (≤ 1 T for M = Mn and Co, but only 0.01 T for M = Fe). At higher magnetic fields ferromagnetic interactions dominate, especially for M = Fe, leading to above-room temperature ferromagnetism (Tc > 300 K) and a hard-magnet hysteresis at 5 K with a 40 kA/m coercivity.

2.2 Introduction

The targeted discovery of materials with specific physical properties can accelerate their application as well as their adoption by other scientific disciplines. This method has been successful in different materials properties and functions such as magnetocaloric[1], phosphorescent[2], mechanically superhard[3, 4], thermoelectric[5] and catalytic[6, 7] materials, just to name a few. Our approach to this endeavor is to couple computational and experimental methods with the aim of discovering new magnetic materials. Metal borides have been extensively studied due to their ability to yield exciting magnetic materials enabled by the presence of magnetic 3d elements such as Mn, Fe or Co.[8-16] In general, materials containing rare-earth elements and magnetic transition metals have delivered "hard" magnetic materials characterized by large coercivity values (H_c > 30 kA/m) and high Curie temperatures (T_C well above room temperature) The rare-earth-free borides that are based on transition elements have mostly delivered "soft" magnetic materials (H_c < 1 kA/m). Recently, we have started to incorporate heavy (5d) transition metals into the structures of such materials to increase the overall spin-orbit coupling (SOC) and thus boost their intrinsic coercivity through an increased magnetic anisotropy energy. This strategy has yielded some quite significant results with the discovery of the first above room temperature semi-hard magnets in the prolific $Ti_3Co_5B_2$ structure type; the quaternary magnets $Hf_2MnIr_5B_2$ (T_C = 590 K, H_c = 13.0 kA/m at 300 K) and $Hf_2FeIr_5B_2$ (T_C = 900 K, H_c = 8.9 kA/m at 300 K).[9] A more recent study targeted solid solution formation and helped deepen our understanding of the factors that drive the formation of hard magnets in this structure type, resulting in the discovery that modulating the

antagonistic antiferromagnetic (AFM) and ferromagnetic (FM) interactions present in these magnetic structures is an important factor. For the studied $Hf_2Fe_{1-d}Ru_{5-x}Ir_{x+d}B_2$ solid solution, the presence of Ru lowered the valence electron (VE) count of $Hf_2FeIr_5B_2$ ferromagnet and introduced strong AFM interactions which were now competing with FM ones, resulting in the formation of magnets with twice (x = 1 member) and thrice (x = 4 member) the coercivity (at 300 K) of the quaternary $Hf_2FeIr_5B_2$ phase.[17] In the present study we will focus on introducing osmium, for the first time in this structure type, which as a 5d element in the same group as Ru will help in enhancing the SOC component thereby increasing the magnetic hardness. Specifically, we aimed at finding Os-rich variants of the metamagnetic $Hf_2MRu_5B_2$ (M = Fe, Mn) by studying $Hf_2MOs_5B_2$ (M = Mn, Fe, Co) through a Density Functional Theory (DFT) prediction followed by experimental verification.

2.3 Results and Discussion

2.3.1 Computational Results and Discussion

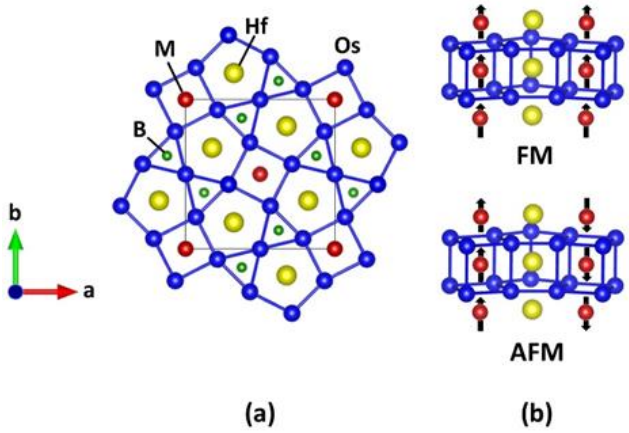

Figure 2.1. (a) Structure of $Hf_2MOs_5B_2$ (M = Mn, Fe, or Co) and (b) the two magnetic models based on ferromagnetic chains of M.

Osmium has never been used in this structure type before, even though neighboring elements such as Ir and Ru have been extensively used as major components in compounds such as $A_2MRu_5B_2$ (A = Zr, Hf; M = Fe, Mn) and $Hf_2MIr_5B_2$ (M = Fe, Mn). Computational models, based on the $Hf_2MRu_5B_2$ structure (replacing Ru by Os), were analyzed to determine the electronic stability, lattice parameters as well as the preferred magnetic ground state in the targeted $Hf_2MOs_5B_2$ (M = Mn, Fe, or Co) compositions, the results of which are given in **Tables 2.1 and 2.2**. The non-spin polarized (*nsp*) calculations are all less stable than spin polarized (*sp*) calculations, indicating that magnetic ordering is highly likely. However, the energy difference (+94.3 meV) between the *sp* and *nsp* models for the Co-based phase is at least six-times smaller than the usual values for this structure type including for the M = Mn and Fe phases (**Table 2.1**), hinting

at potentially weak magnetic interactions in the M = Co phase. This finding is further illustrated by the density of states (DOS) plots in **Figures 2.2, 2.S1 and 2.S2 (left)**. The *nsp* DOS for all three systems have the Fermi energy (E_F) on a peak shoulder, which has been understood as a sign of electronic instability. Interestingly, the magnetic 3d metal M (Fe, Mn, or Co) contributes the most to the states at E_F, which would indicate the metal M to be mainly responsible for the electronic instability. Fortunately, spin-polarized calculations alleviate this instability entirely for M = Mn and Fe but only partially for M = Co (**Figures 2.2, 2.S1 and 2.S2, right**). In fact, in the *sp* DOS E_F is now in a pseudo-gap for M = Mn and Fe while for M = Co one of the spin densities is still on a peak. This finding corroborates well with the relaxation energy calculations discussed above and points to clear magnetic ordering preference for M = Mn and Fe but potentially weak magnetic interactions or even paramagnetism for M = Co. Given that the rigid band model has been successfully applied in this structure type before, it might be used here to also understand the stability of these phases and predict future targets that might show even better magnetic properties. Considering the position of E_F in the *nsp* DOS plots, E_F in positioned near a large peak in the Mn and Fe *nsp* DOS, thus adding more electrons to these systems may lead to greater instability in the *nsp* calculation and to a greater spin-splitting in the sp calculation, thereby producing larger magnetic moments and thus greater magnetic interactions. We are therefore currently studying solid solutions such as $Hf_2MOs_{5-x}Ir_xB_2$ (M = Mn, Fe).

Table 2.1. VASP Total Energies for the different magnetic models relative to the lowest energy model, and Exchange Energy ($E_{EX} = E_{AFM} - E_{FM}$) and Spin-Orbit Coupling Energy (E_{SOC}) for the ferromagnetic models. (VEC = valence electron count, FM = ferromagnetic, AFM = antiferromagnetic, NM = nonmagnetic).

	VEC	FM (meV/f.u.)	AFM (meV/f.u.)	NM (meV/f.u.)	E_{EX} (meV/f.u.)	E_{SOC} (meV/f.u.)	Reference
$Hf_2MnOs_5B_2$	61	0	+5.92	+587.17	+5.92	-2.13	18
$Hf_2FeOs_5B_2$	62	+20.36	0	+732.11	-20.36	+1.92	18
$Hf_2CoOs_5B_2$	63	0	+100.69	+94.31	+100.69	-	This work

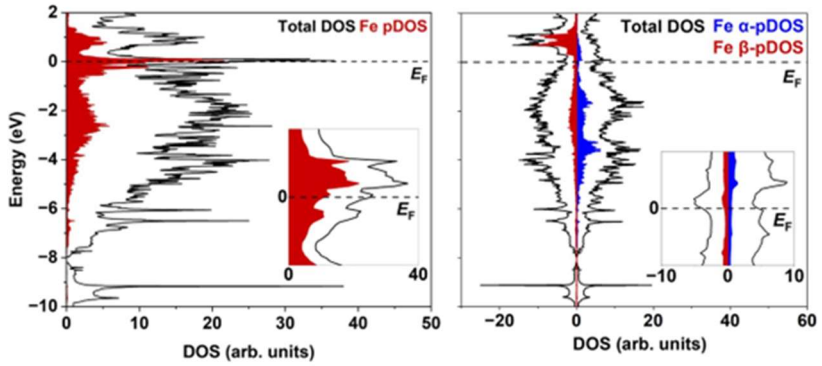

Figure 2.2. Non-spin-polarized (left) and spin-polarized (right) density of state curves of $Hf_2FeOs_5B_2$. Insets represent the zoom in around E_F (between -0.2 and 0.2 eV).

To understand the nature of the underlying magnetism in these compounds we have studied two of the most stable magnetic models found in this structure type, a ferromagnetic (FM) model represented by the above discussed *sp* calculations and an antiferromagnetic (AFM) model (see **Figure 1**). The results show an unexpected trend, as FM is preferred in the Mn-based phase while AFM is preferred in the Fe-based one, which is contrary to the magnetic nature of the 3d elements Mn (AFM) and Fe (FM). The two phases have 61 (M = Mn) and 62 (M = Fe) valence electrons (VE), thus these results

are in line with observations in this structure type: Examples include Ru-rich phases such as the FM ground state found in $Hf_2MnRu_5B_2$ (61 VE)[16] and $Zr_2MnRu_5B_2$ (61 VE)[16] while AFM ground state was found for $Hf_2FeRu_5B_2$ (62 VE)[16] and $Zr_2FeRu_5B_2$ (62 VE)[16]. However, the spin-exchange energy ($E_{EX} = E_{AFM} - E_{FM}$) difference between AFM and FM states in the two new compounds is relatively small (much smaller for Mn at 5.92 meV vs. -20.36 meV for Fe), indicating that a small change in composition or even the magnetic field (metamagnetism) may be enough to flip the ordering from one model to another. The M = Co phase has a FM ground state, but the NM state is more stable than the AFM state which is the first time that this has been encountered in this structure type. In addition, FM is only 94.31 meV more stable than NM, which is also an unprecedentedly low value as discussed above. These findings suggest that the M = Co phase is likely in a very weak magnetic state (spin glass-like) or even paramagnetic. These predictions have been verified experimentally, as shown below. Also, the predicted lattice parameters from the ground state models are in good agreement with those found experimentally with a small underestimation for all phases.

In addition to energy calculations, spin-orbit coupling (SOC) calculations were also executed using equation (1). The magnetocrystalline anisotropy energy (E_{MAE}) is the summation of the spin-orbit coupling Energy (E_{SOC}) and the long-range magnetic dipole–dipole interaction energy (E_{MDD}). However, this study assumes, based on previous studies, that the magnitude of E_{MDD} is relatively insignificant compared to E_{SOC}, and thus $E_{SOC} \approx E_{MAE}$.

$$ESOC = ESOC\parallel c - ESOC\perp c \quad \textbf{(1)}$$

The SOC and spin-exchange energy (E_{EX}) are provided in **Table 2.1** for the three compositions. SOC occurs when the spins prefer to be oriented along a particular axis (called the easy axis). Since $Hf_2MnOs_5B_2$ has a positive E_{SOC}, this would indicate a preference for spin orientations perpendicular to the c-axis. The negative E_{SOC} values for the Fe and Co compositions would indicate a preference for spin orientations on the easy c-axis. However, the spin orientations of these new Os-based phases are opposite to those of the recently discovered $Hf_2FeIr_5B_2$ and $Hf_2MnIr_5B_2$, respectively.[9] We discovered in the study of $Hf_2Fe_{1-d}Ru_{5-x}Ir_{x+d}B_2$ solid solution, that the presence of Ru lowered the valence electron (VE) count of $Hf_2FeIr_5B_2$ ferromagnet and introduced strong AFM interactions which were now competing with FM ones, resulting in the formation of magnets with twice (x = 1 member) and thrice (x = 4 member) the intrinsic coercivity of the quaternary $Hf_2FeIr_5B_2$ phase.[17] These increased intrinsic coercivity resulted mainly from negative E_{SOC} values (or smaller positive E_{SOC} values than that of $Hf_2FeIr_5B_2$) combined with negative E_{EX}. From these observations we can predict that $Hf_2FeOs_5B_2$ will have a greater intrinsic coercivity than $Hf_2FeIr_5B_2$ given its negative E_{EX} and smaller positive E_{SOC} values than that of $Hf_2FeIr_5B_2$. Specifically, E_{SOC} (1.92 meV) and E_{EX} (-20.36 meV) values of $Hf_2FeOs_5B_2$ can be compared to those of the two hardest members, x = 4 (E_{SOC} = 2.92 meV) and x = 2 (E_{EX} = -15.62 meV), of the $Hf_2Fe_{1-d}Ru_{5-x}Ir_{x+d}B_2$ solid solution[17], thereby showing that this new phase could be as magnetically hard as these Ir-containing compositions. $Hf_2MnOs_5B_2$, on the contrary has a very small and positive E_{EX} (5.92 meV) which comparable to that of the x = 3 member (E_{EX} = 6.27 meV) suggesting similarly smaller intrinsic coercivity value. However, its negative E_{SOC} (-2.13 meV) is

closer to that of $Hf_2MnIr_5B_2$ (E_{SOC} = -1.55 meV) suggesting favorable easy axis and intrinsic coercivity value as large as $Hf_2MnIr_5B_2$. Therefore, the intrinsic coercivity of $Hf_2MnOs_5B_2$ would be difficult to predict given these antagonistic suggestions. Nevertheless this new phase should be at least semi-hard just like the x = 3 composition of the $Hf_2Fe_{1-d}Ru_{5-x}Ir_{x+d}B_2$ solid solution.[17]

2.3.2 Experimental Results and Discussion

The three compounds were synthesized by arc-melting, as described in the methods section, and characterized by powder X-ray diffraction (PXRD) and energy dispersive X-ray (EDX) analysis. The PXRD for all three samples yielded two phases – $Hf_2MOs_5B_2$ (M = Fe, Mn, Co) of the $Ti_3Co_5B_2$ structure type and elemental osmium. There are also some small peaks that correspond to HfO_2. The unidentified peaks between 25-35 degrees were more pronounced in the manganese and cobalt samples, so HCl treatment was executed and was successful in reducing the intensity of the unknown phase. Considering Co is a 3d transition metal while Hf and Os are 5d transition metals, mixed occupancy refinement of the PXRD was tested. When the *2a* Fe-site is mixed with 10% Hf and the *4g* Hf-site is mixed with 5% Fe to maintain the overall starting composition, the agreement is comparable to that of refinement with no mixed occupancy. That is, the R_f-factor of the main phase improved to 3.68 with mixed occupancy from 4.70 without mixed occupancy, but the osmium phase R_f-factor got worse with 3.30 with mixed occupancy from 2.36 without mixed occupancy. In addition, there is around 3% increase in the main phase without mixed occupancy. Thus, we conclude that the current data do

not support mixed occupancy refinements. The main phase, when refined against $Hf_2MOs_5B_2$ without mixed occupancy gave weight percentages of 98(2) wt.%, 94(2) wt.%, and 94(2) wt.% for M = Mn, Fe, and Co, respectively. The resulting Rietveld refinement data are given in **Table 2.2** and plotted in **Figures 2.3, 2.S3 and 2.S4**. The PXRDs do not account for preferred orientation. An interesting trend is found, as the *a*-lattice parameter decreases with increasing atomic number, thus correlating from M = Mn to Co, while the *c*-lattice parameter increases, albeit only slightly, leading to an almost constant unit cell volume. The refined lattice parameters agree well with those calculated for the lowest energy models (**Table 2.2**).

Table 2.2. Rietveld refinement data of the $Hf_2MOs_5B_2$ (M = Mn, Fe, Co) phases, and lattice parameters of the corresponding lowest energy computational model.

Fixed composition	**$Hf_2MnOs_5B_2$**	**$Hf_2FeOs_5B_2$**	**$Hf_2CoOs_5B_2$**
Space group		*P4/mbm*	
a (Å)	Expt. 9.4347(5) *Calc. 9.37883*	Expt. 9.4418(5) *Calc. 9.34754*	Expt. 9.4149(6) *Calc. 9.34140*
c (Å)	Expt. 3.0600(2) *Calc. 3.03808*	Expt. 3.0584(2) *Calc. 3.04706*	Expt. 3.0608(2) *Calc. 3.05061*
Unit cell volume ($Å^3$)	272.38(3)	272.64(3)	271.31(3)
Formula units per cell		2	
Calculated density (g/cm^3)	16.882	16.878	16.997
2θ range (°)	3 - 90	5 - 90	3 - 80
Refinement Range		Least-squares	
Profile Function		Pseudo-voigt	
R_{Bragg}	8.28	8.19	10.4
R_F	4.66	4.36	5.53
χ^2	4.90	5.83	7.58
Weight fraction for 2 side phases (wt.%)	7(2)	12(2)	7(2)

EDX semi-quantitative metal analysis was carried out on large grains of the polycrystalline samples as well as elemental mapping, the results of which are provided in **Figures 2.S5-2.S7**. Boron was not detected by EDX for all three compositions. The EDX composition without boron is in relatively good agreement with the expected starting composition given the almost single-phase nature of the samples. Furthermore, the EDX mappings show homogeneous distributions of all the metals, which supports the successful single-phase synthesis of each phase.

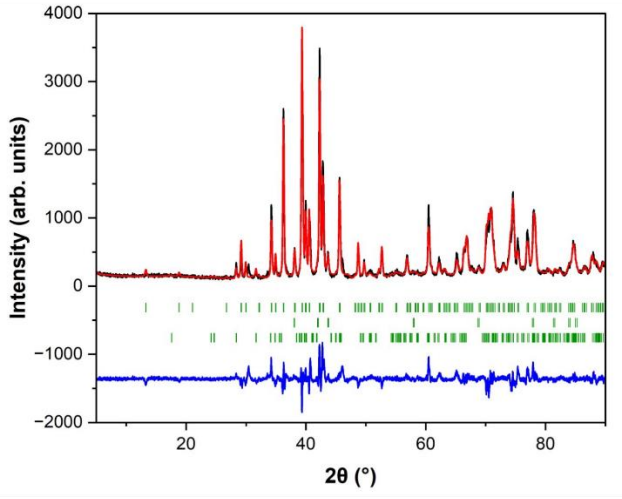

Figure 2.3. Rietveld refinement plot showing observed (black) fitted with calculated (red) powder X-ray diffraction patterns of $Hf_2MnOs_5B_2$. The positions of the Bragg reflections are given in green for $Hf_2MnOs_5B_2$ (top row), Os (middle row), and HfO_2 - *P 21/c* (bottom row). Difference curve (blue) obtained from Rietveld refinement.

Following the above predicted magnetic properties of the new phases, magnetization measurements were carried out for experimental verification. The magnetic susceptibility (c) was measured in zero-field-cooled (ZFC) and field-cooled (FC) modes at 0.01 T and 1 T (ZFC only) as a function of temperature (temperature range 3-300 K) on polycrystalline samples of $Hf_2MOs_5B_2$ (M = Fe, Mn, Co) phases. The low temperature *c-T* plots (**Figures 2.4 and 2.5)** have different behaviors. For M = Mn (**Figures 2.4,** left), a sharp transition at the Néel temperature (T_N = 19 K) in the 0.01 T ZFC curve but it almost vanishes in the FC measurement, showing that the available AFM interactions are weak. The 0.01 T ZFC plot for the M = Fe phase (**Figures 2.5,** left) has a sharper and much higher maximum (T_N = 90 K) suggesting greater AFM interactions than for the Mn-based phase, but the maximum also vanishes in the FC plot, thus these AFM interactions are also weak in the Fe-based phase. For M = Co (**Figures 2.5,** right) the broadest maximum

is observed in the 0.01 T ZFC curve peaking at T_N = 45 K, but contrary to the previous two cases it is maintained in the 0.01 T FC curve, an indication of the robustness of the AFM interactions in this phase albeit in a typical spin-glass-like manner (very broad maximum). However, a minimum is found at about 5 K with a sudden rise in susceptibility, likely due to the presence of a small magnetic impurity. These low-temperatures low magnetic field results show that all these phases have weak AFM interactions, and that the Fe-based phase has the strongest AFM interactions, a result in full agreement with the DFT predictions of a negative E_{EX} (-20.36 meV) for this phase while a small and positive value was found for the Mn-based phase. DFT was undecided on the magnetic state (either weakly ferromagnetic or paramagnetic) of the Co-based phase and so are the current experimental results which suggest a potentially very weak spin glass state.

The assessment of weak AFM interactions in all three phases is further strengthened by the lack of a maximum in the ZFC susceptibility curve at 1 T (**Figure 2.4,** right, and **Figure 2.5**). In fact, the Co-based phase shows a paramagnetic behavior while for M = Mn and M = Fe ferromagnetic behaviors emerge with Curie temperatures T_C = 60 K and > 300 K, respectively. The magnetization versus magnetic field curves at 5, 50 and 300 K confirmed FM below and above 300 K for the Mn- and Fe-based phases, respectively (**Figures 2.6 and 2.7)**.

DFT calculations predicted semi-hard magnetic behavior for the $Hf_2MnOs_5B_2$ and hard magnetic behavior for $Hf_2FeOs_5B_2$. The recorded hypothesis loops at 5 K indeed confirm these predictions as coercivity values of 0.11(1) kOe (or 10.0 kA/m) and 0.55(1) kOe (or

49.9 kA/m) were recorded for $Hf_2MnOs_5B_2$ (61 VE) and $Hf_2FeOs_5B_2$ (62 VE), respectively. These intrinsic coercivity values are unprecedented for phases of this $Ti_3Co_5B_2$ structure type without a group 9 transition metal (Rh or Ir). In fact, all semi-hard and hard magnetic behaviors that have been reported so far for $Ti_3Co_5B_2$-type phases contain at least a group 9 transition metal (**Table 2.S1**). Consequently, the 5d osmium, used for the first time in this structure type, is the main reason for the high magnetic hardness. These observations suggest that incorporating a group 9 transition metal (Rh or Ir) in the new phases through Os substitution might lead to the discovery of even harder magnets, especially above room temperature. Such studies are in progress.

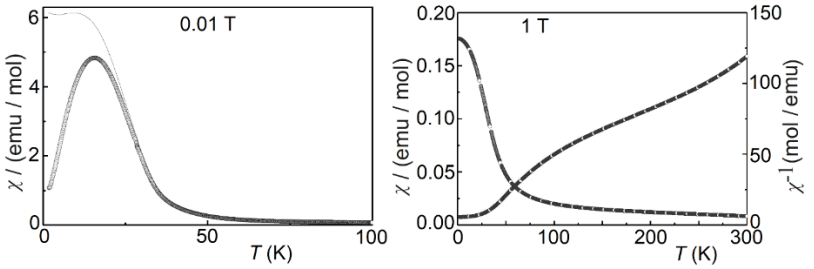

Figure 2.4. Low-temperature ZFC/FC magnetization curves at 0.01 T (left) and ZFC magnetization curve at 1 T (right) for $Hf_2MnOs_5B_2$.

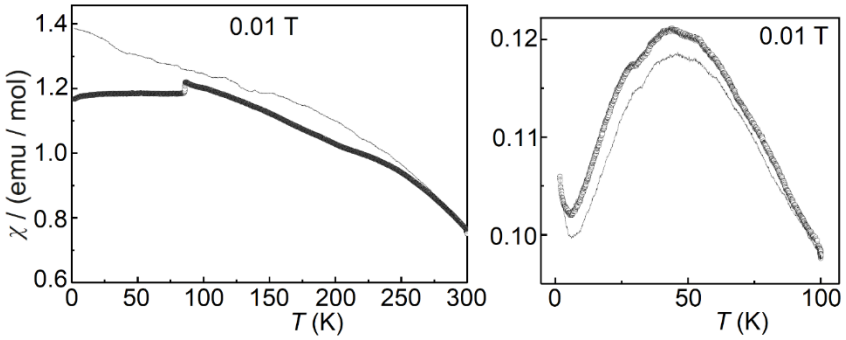

Figure 2.5. Low-temperature ZFC/FC magnetization curves at 0.01 T for $Hf_2FeOs_5B_2$ (left) and $Hf_2CoOs_5B_2$ (right).

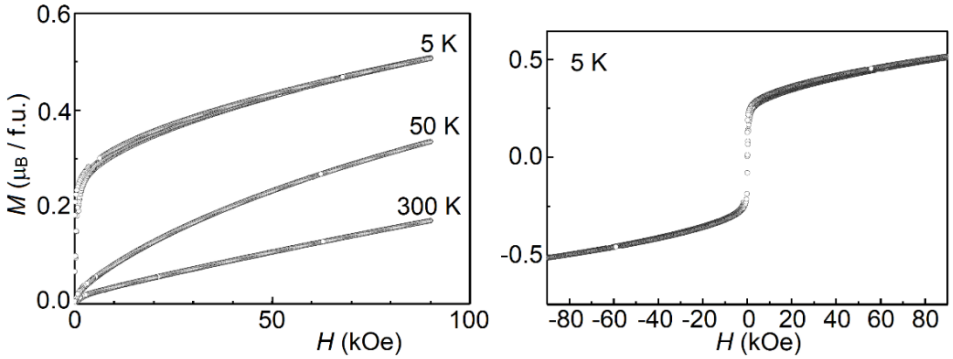

Figure 2.6. Magnetization versus magnetic field plots at different temperatures (left) and hysteresis loop (at 5 K, middle) for $Hf_2MnOs_5B_2$.

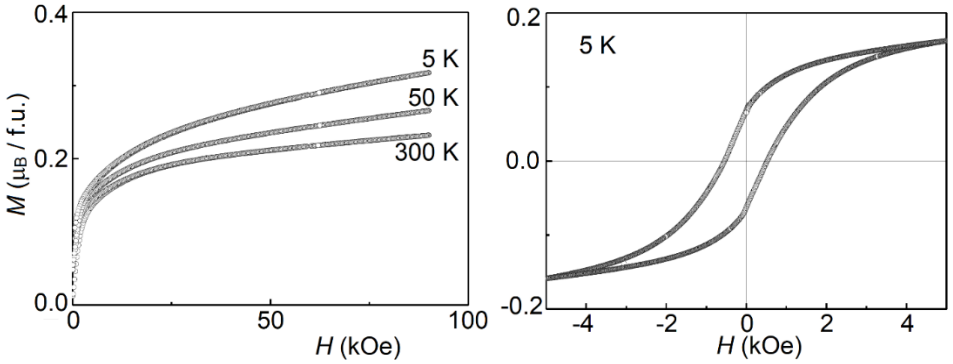

Figure 2.7. Magnetization versus magnetic field plots at different temperatures (left) and hysteresis loop (at 5 K) for $Hf_2FeOs_5B_2$ (right).

2.4 Conclusion

This study reports on the first compositions containing osmium of the $Ti_3Co_5B_2$ structure type, $Hf_2MOs_5B_2$ (M = Mn, Fe, Co), and shows that they enable metamagnetic materials. DFT calculations predicted the stability and metamagnetic nature of the phases with M = Mn and Fe but very weak ferromagnetism or paramagnetism for M = Co. Experimental investigations through PXRD and EDX analysis confirmed the successful arc-melting synthesis of these new materials. Magnetic measurements confirm the semi-hard and hard-magnetic behaviors for $Hf_2MnOs_5B_2$ and $Hf_2FeOs_5B_2$, respectively, thus confirming

DFT predictions based on energy exchange and spin-orbit calculations. This study opens a new avenue for discovering above-room temperature hard-magnetic osmium-based materials of the $Ti_3Co_5B_2$ structure type.

2.5 Methods

2.5.1 Experimental Methods

The materials were synthesized by first mixing the respective elemental powders according to the stoichiometric ratio $Hf_2MOs_5B_2$ (M = Mn, Fe, Co), except for boron where an extra 20% of the stoichiometric amount was weighed, in a glove box. Starting materials consisted of Fe (99+%, Alfa Aesar), Mn (³99%, Aldrich), Co (99.8%, Aldrich), Hf (99.6%, Alfa Aesar), Os (99.8%, Thermo Scientific), and B (95-97% amorphous, Thermo Scientific). The powders were then ground and mixed before being pressed into pellets. Each pellet was then arc-melted for 2-3 seconds in a water-cooled copper crucible under an Ar atmosphere (99.995 %, Airgas) using a tungsten electrode at 20–30 V and 40 A. The metallic beads were then crushed and ground for Powder X-ray Diffraction (PXRD) analysis in a Rigaku Miniflex 600 diffractometer with Cu-Kα1 (λ=1.540593 Å) radiation. Rietveld refinement[19] was applied to refine the lattice parameters and identify the phases present in the products. The chemical compositions of the products were also analyzed using energy dispersive X-ray (EDX) spectroscopy on a Tescan Vega3 SBH with Bruker LN2-free high resolution and a high-speed 30 mm^2 SD detector. For EDX analysis the energy resolution was ≤ 129 eV at Mn-Kα, and the window of detection was from boron to californium. HCl treatment with 60% HCl for 2 hours and 20% HCl for 2

hours were done for $Hf_2MnOs_5B_2$ and $Hf_2CoOs_5B_2$ respectively, to reduce the size of peaks between 25-35 degrees that did not correspond to the desired phase.

For the low temperature magnetization measurements (3-300 K), the powdered samples were filled into polyethylene (PE) capsules that were attached to the sample holder rod. For the high temperature measurements (300-1000 K), the powders were pressed to small pellets (ø 2 mm) under a pressure of 100 bar. Pieces of these pellets were subsequently obtained by careful fragmentation. One fragment was mounted on a high-temperature sample holder using Zircar® cement, followed by careful wrapping in Cu-foil. The sample was then attached to the sample holder rod of a Vibrating Sample Magnetometer (VSM) for measuring the magnetization M (T, H) in a Quantum Design Physical Property Measurement System (PPMS). Samples were initially cooled from room temperature to 4 K in the absence of a magnetic field for the zero-field cooled (ZFC) measurement, then a field was applied, and measurements were made in the warming cycle. Field cooled (FC) curves were attained by cooling to 4 K while maintaining a constant applied field and measurements were recorded as a function of increasing temperature.

2.5.2 Computational Methods

The structural model was prepared from the known $Hf_2FeIr_5B_2$ structure obtained from the ICSD database, and the atoms were adjusted to reflect the expected composition – Ir atoms were changed to Os. The structural model was simplified to not have mixed

occupancies – the 64% Fe: 34% Ir sites were 100% M (M = Mn, Fe, or Co). For energy calculations, the lattice parameters, cell shape, cell volume, and atomic positions were allowed to relax using the projector augmented wave method in the Vienna Ab-initio Simulation Package (VASP)[20]. All VASP calculations employed the generalized gradient approximation (GGA) with exchange and correlation utilizing the Perdew, Burke and Ernzerhof (PBE) functional[21]. The cutoff energy was 450 eV, and the global break condition for the electronic SC-loop (E_{diff}) was 1E-06. The k-point mesh was a 7×7×19 Monkhorst-Pack grid. The magnetic calculations were performed by inputting initial magnetic moments onto the iron atoms for all steps, including relaxation calculations. Upon relaxing, self-consistency (SC) calculations were run followed by density of states (DOS) calculations. The DOS calculations utilized the CHGCAR file from the SC calculation, and the number of grid points on which the DOS was evaluated (NEDOS) was 2000. For DOS plots, the Fermi energy (E_F) was set to 0 eV. Spin-orbit coupling calculations were also executed.

2.6 Acknowledgements

The authors would like to acknowledge the financial support from UC Riverside and the NSF (Career grant to B.P.T.F., DMR 1654780).

2.7 References

1. Fortunato, N. M.; Taubel, A.; Marmodoro, A.; Pfeuffer, L.; Ophale, I.; Ebert, H.; Gutfleisch, O.; Zhang, H., High-Throughput Design of Magnetocaloric Materials for Energy Applications: MM′X alloys. *Advanced Science* **2023,** *10* (17), 2206772.

2. Tian, R.; Gao, S.; Li, K.; Lu, C., Design of mechanical-robust phosphorescence materials through covalent click reaction. *Nature Communications* **2023,** *14* (1), 4720.

3. Kaner, R. B.; Gilman, J. J.; Tolbert, S. H., Materials science. Designing superhard materials. *Science* **2005,** *308* (5726), 1268-9.

4. Zhang, Z.; Brgoch, J., Treating Superhard Materials as Anomalies. *Journal of the American Chemical Society* **2022,** *144* (39), 18075-18080.

5. Mukherjee, M.; Srivastava, A.; Singh, A. K., Recent advances in designing thermoelectric materials. *Journal of Materials Chemistry C* **2022,** *10* (35), 12524-12555.

6. Zhao, Z.-J.; Liu, S.; Zha, S.; Cheng, D.; Studt, F.; Henkelman, G.; Gong, J., Theory-guided design of catalytic materials using scaling relationships and reactivity descriptors. *Nature Reviews Materials* **2019,** *4* (12), 792-804.

7. Lee, E.; Fokwa, B. P. T., Nonprecious Metal Borides: Emerging Electrocatalysts for Hydrogen Production. *Accounts of Chemical Research* **2022,** *55* (1), 56-64.

8. Fokwa, B. P. T.; Lueken, H.; Dronskowski, R., Rational Synthetic Tuning between Itinerant Antiferromagnetism and Ferromagnetism in the Complex Boride Series Sc2FeRu5−nRhnB2 (0≤n≤5). *Chemistry – A European Journal* **2007,** *13* (21), 6040-6046.

9. Shankhari, P.; Janka, O.; Pöttgen, R.; Fokwa, B. P. T., Rare-Earth-Free Magnets: Enhancing Magnetic Anisotropy and Spin Exchange Toward High-TC Hf2MIr5B2 (M = Mn, Fe). *Journal of the American Chemical Society* **2021,** *143* (11), 4205-4212.

10. Xie, W.; Fuccillo, M. K.; Phelan, B. F.; Luo, H.; Cava, R. J., Stabilization of the Ti3Co5B2-type structure for Ti3−xSixRu5B2 through Si–Ti substitution. *Journal of Solid State Chemistry* **2015,** *227*, 92-97.

11. Burghaus, J.; Dronskowski, R.; Miller, G. J., Slater–Pauling behavior within quaternary intermetallic borides of the Ti3Co5B2 structure-type. *Journal of Solid State Chemistry* **2009,** *182* (10), 2613-2619.

12. Shankhari, P.; Scheifers, J. P.; Hermus, M.; Yubuta, K.; Fokwa, B. P. T., Unexpected Trend Deviation in Isoelectronic Transition Metal Borides A3T5B2 (A = group 4, T = group 9): Ti3Co5B2- vs. Perovskite-Type Studied by Experiments and DFT Calculations. *Zeitschrift für anorganische und allgemeine Chemie* **2017,** *643* (21), 1551-1556.

13. Fokwa, B. P. T.; Lueken, H.; Dronskowski, R., Rational Design of Complex Borides – One-Electron-Step Evolution from Soft to Semi-Hard Itinerant Ferromagnets in the New Boride Series Ti2FeRu5–nRhnB2 ($1 \leq n \leq 5$). *European Journal of Inorganic Chemistry* **2011,** *2011* (26), 3926-3930.

14. Brgoch, J.; Yeninas, S.; Prozorov, R.; Miller, G. J., Structure, bonding, and magnetic response in two complex borides: Zr2Fe1−δRu5+δB2 and Zr2Fe1−δ(Ru1−xRhx)5+δB2. *Journal of Solid State Chemistry* **2010,** *183* (12), 2917-2924.

15. Shankhari, P.; Zhang, Y.; Stekovic, D.; Itkis, M. E.; Fokwa, B. P. T., Unexpected Competition between Antiferromagnetic and Ferromagnetic States in Hf2MnRu5B2: Predicted and Realized. *Inorganic Chemistry* **2017,** *56* (21), 12674-12677.

16. Shankhari, P.; Bakshi, N. G.; Zhang, Y.; Stekovic, D.; Itkis, M. E.; Fokwa, B. P. T., A Delicate Balance between Antiferromagnetism and Ferromagnetism: Theoretical and Experimental Studies of A2MRu5B2 (A=Zr, Hf; M=Fe, Mn) Metal Borides. *Chemistry – A European Journal* **2020,** *26* (9), 1979-1988.

17. Luong, D.; Schumacher, L.; Kilic, S.; Haddon, E.; Pöttgen, R.; Fokwa, B. T. P., Enhancing Intrinsic Magnetic Hardness by Modulating Antagonistic Interactions in the Rare-Earth-Free Magnetic Solid Solution Hf2Fe1− δ Ru5− x Ir x + δ B2. *Chemistry – A European Journal* **2023,** https://doi.org/10.1002/chem.202303381.

18. Luong, D. Exploring Magnetism in Metal-Rich Borides: Synthesis, Characterization, and Magnetic Properties. University of California, Riverside, 2023.

19. Rodriguez-Carvajal, J. In *FULLPROF: a program for Rietveld refinement and pattern matching analysis*, satellite meeting on powder diffraction of the XV congress of the IUCr, Toulouse, France:[sn]: 1990.

20. Kresse, G.; Joubert, D., From ultrasoft pseudopotentials to the projector augmented-wave method. *Physical Review B* **1999,** *59* (3), 1758-1775.

21. Perdew, J. P.; Burke, K.; Ernzerhof, M., Generalized Gradient Approximation Made Simple. *Physical Review Letters* **1996,** *77* (18), 3865-3868.

2.8 Supplementary Material

Table S2.1. Calculated spin orbit coupling energy (E_{SOC}), exchange energy (E_{EX}), magnetic moment (M_{th}), and experimental magnetic quantities [coercivity (H_c) at 5 K, magnetic moment (M), Néel temperature (T_N), and Curie temperature (T_C)] for various $Ti_3Co_5B_2$-type phases. VEC = valence electrons count.

	VEC	E_{SOC} (meV/f.u.)	E_{EX} (meV/f.u.)	H_c (kA/m)	T_N; T_C (K)	*Reference*
$Hf_2FeRu_5B_2$	62	-0.39	-62.26	Very small	25; -	1, 2
$Hf_2FeRu_4Ir\ B_2$	63	-0.72	+353.48	23.1	70; 600	1
$Hf_2FeRu_3Ir_2B_2$	64	-0.75	-15.62	74.0	60; 150	1
$Hf_2FeRu_2Ir_3B_2$	65	-0.28	+6.27	26.3	63; 175	1
$Hf_2FeRuIr_4B_2$	66	+2.92	+16.44	66.1	55; 750	1
$Hf_2FeIr_5B_2$	67	+3.27	+40.19	12.1	-; 900	3
$Hf_2MnIr_5B_2$	66	-1.55	-60.01	62.0	30; 590	3
$Sc_2FeRu_3Ir_2B_2$	62	-2.83	-36.77	51.6	-; -	4, 5
$Sc_2FeRu_2Ir_3B_2$	63	-	-	52.4	-; 85	5
$Ti_2FeRu_4RhB_2$	63	-0.23	-30.55	-	-; -	4

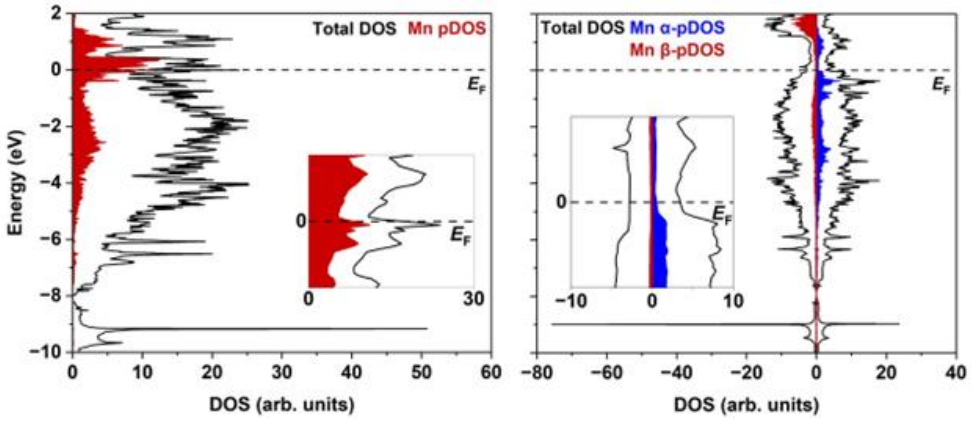

Figure S2.1. Non-spin-polarized (left) and spin-polarized (right) density of state curves of $Hf_2MnOs_5B_2$. Smaller graphs are the zoom in of the E_F between +0.2 and -0.2 eV.

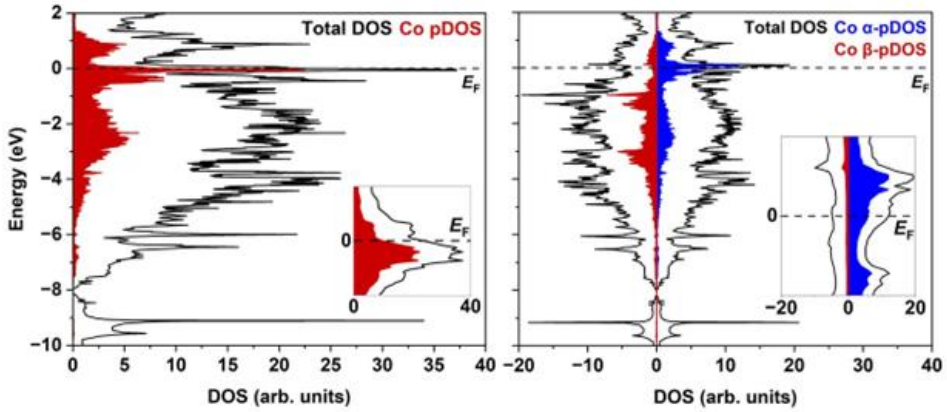

Figure S2.2. Non-spin-polarized (left) and spin-polarized (right) density of state curves of $Hf_2CoOs_5B_2$. Smaller graphs are the zoom in of the E_F between +0.2 and -0.2 eV.

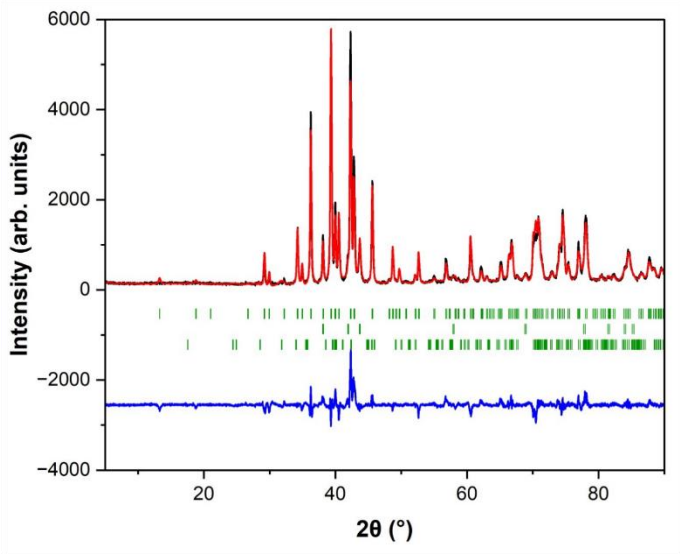

Figure S2.3. Rietveld refinement plot showing observed (black) fitted with calculated (red) powder X-ray diffraction patterns of $Hf_2FeOs_5B_2$. The positions of the Bragg reflections are given in green for $Hf_2MnOs_5B_2$ (top row), Os (middle row), and HfO_2 - *P 21/c* (bottom row). Difference curve (blue) obtained from Rietveld refinement.

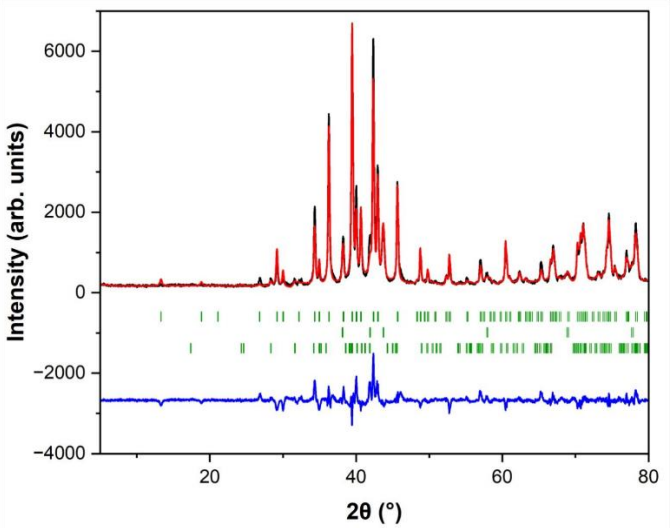

Figure S2.4. Rietveld refinement plot showing observed (black) fitted with calculated (red) powder X-ray diffraction patterns of $Hf_2CoOs_5B_2$. The positions of the Bragg reflections are given in green for $Hf_2MnOs_5B_2$ (top row), Os (middle row), and HfO_2 - *P 21/c* (bottom row). Difference curve (blue) obtained from Rietveld refinement.

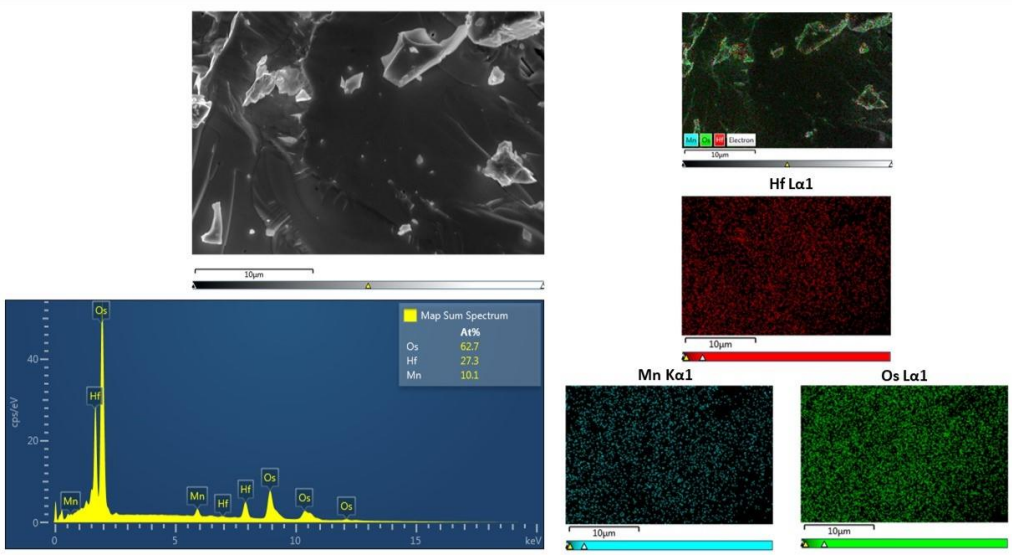

Figure S2.5. SEM image (top left) and EDX spectrum (bottom left) and elemental mapping (right) of $Hf_2MnOs_5B_2$.

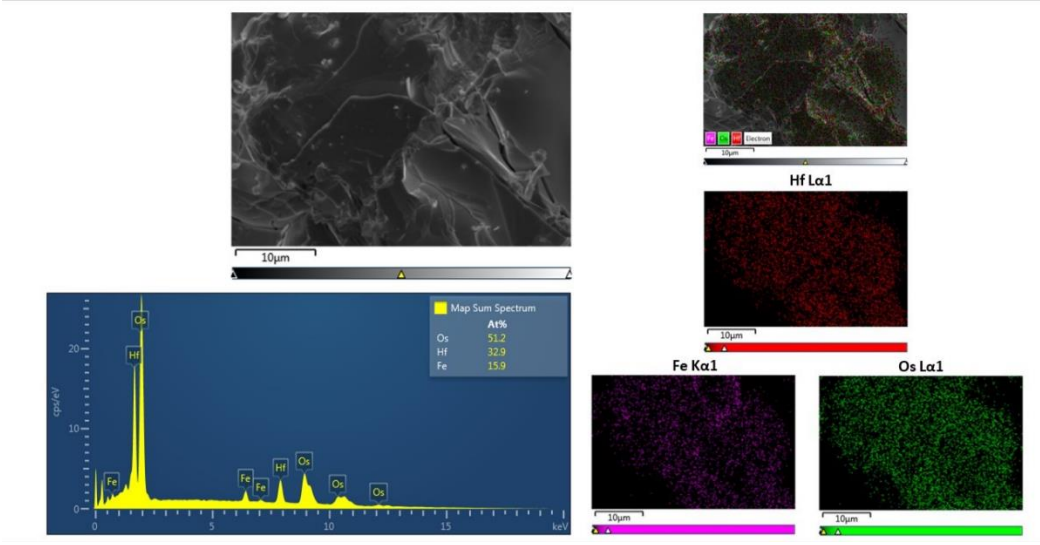

Figure S2.6. SEM image (top left) and EDX spectrum (bottom left) and elemental mapping (right) of $Hf_2FeOs_5B_2$.

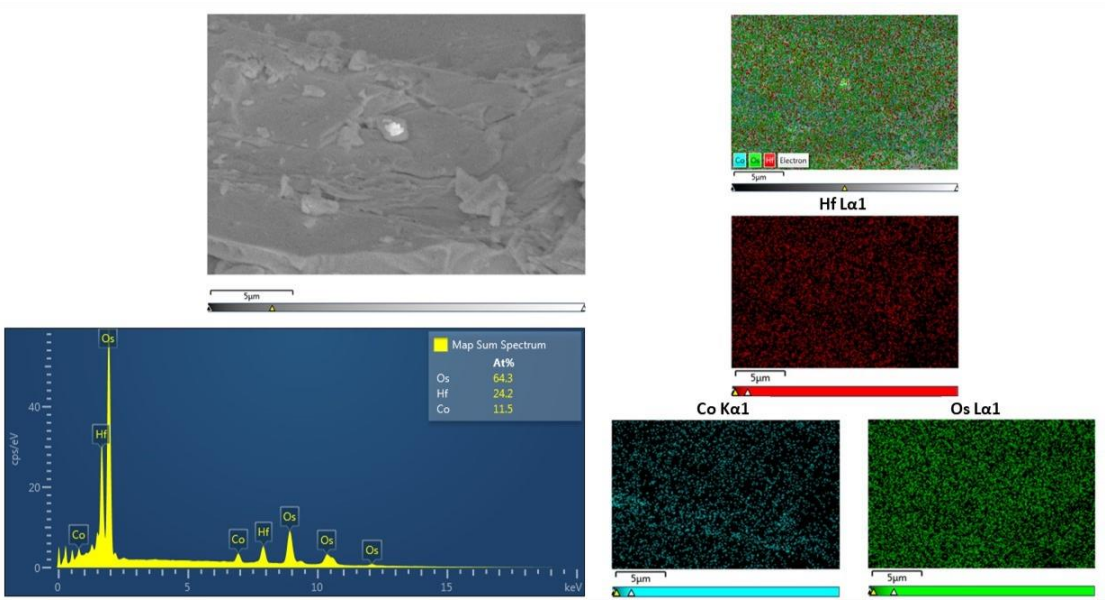

Figure S2.7. SEM image (top left) and EDX spectrum (bottom left) and elemental mapping (right) of $Hf_2CoOs_5B_2$.

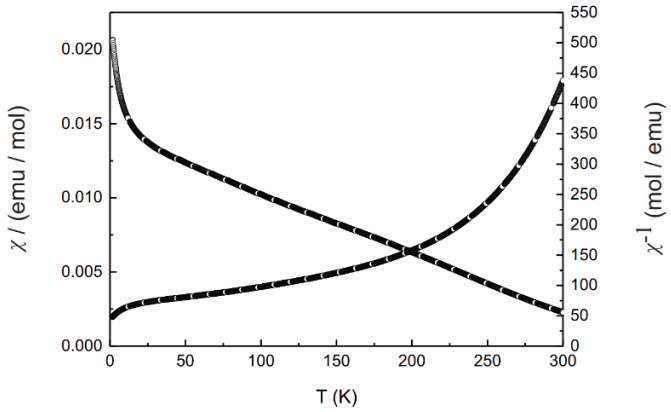

Figure S2.8. Low-temperature ZFC magnetization curve at 1 T (right) for $Hf_2CoOs_5B_2$.

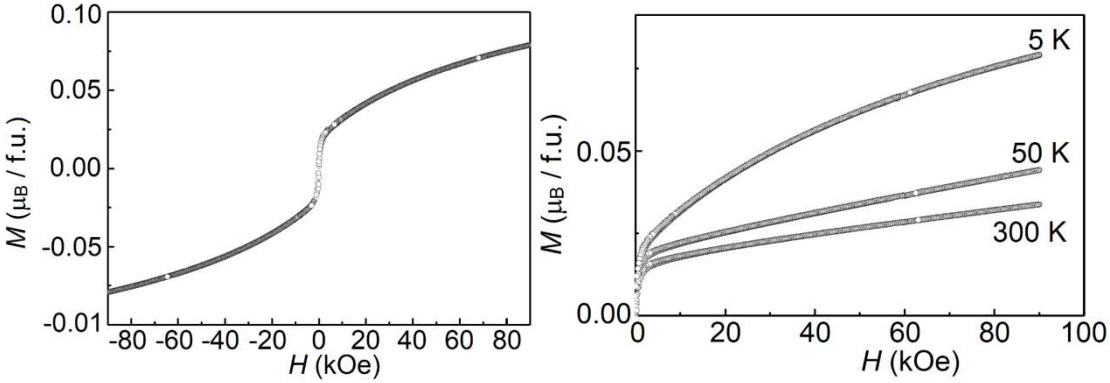

Figure S2.9. Hysteresis plot (at 5 K, left) and magnetization versus magnetic field at different temperatures (right) for $Hf_2CoOs_5B_2$. The hysteresis is likely due to a ferromagnetic impurity.

2.9 Supplementary Material References

1. Luong, D.; Schumacher, L.; Kilic, S.; Haddon, E.; Pöttgen, R.; Fokwa, B. T. P., Enhancing Intrinsic Magnetic Hardness by Modulating Antagonistic Interactions in the Rare-Earth-Free Magnetic Solid Solution Hf2Fe1− δ Ru5− x Ir x + δ B2. *Chemistry – A European Journal* **2023**, *n/a* (n/a), e202303381.

2. Shankhari, P.; Bakshi, N. G.; Zhang, Y.; Stekovic, D.; Itkis, M. E.; Fokwa, B. P. T., A Delicate Balance between Antiferromagnetism and Ferromagnetism: Theoretical and Experimental Studies of A2MRu5B2 (A=Zr, Hf; M=Fe, Mn) Metal Borides. *Chemistry – A European Journal* **2020**, *26* (9), 1979-1988.

3. Shankhari, P.; Janka, O.; Pöttgen, R.; Fokwa, B. P. T., Rare-Earth-Free Magnets: Enhancing Magnetic Anisotropy and Spin Exchange Toward High-TC Hf2MIr5B2 (M = Mn, Fe). *Journal of the American Chemical Society* **2021**, *143* (11), 4205-4212.

4. Zhang, Y.; Miller, G. J.; Fokwa, B. P. T., Computational Design of Rare-Earth-Free Magnets with the Ti3Co5B2-Type Structure. *Chemistry of Materials* **2017**, *29* (6), 2535-2541.

5. Hermus, M.; Yang, M.; Grüner, D.; DiSalvo, F. J.; Fokwa, B. P. T., Drastic Change of Magnetic Interactions and Hysteresis through Site-Preferential Ru/Ir Substitution in Sc2FeRu5–xIrxB2. *Chemistry of Materials* **2014**, *26* (5), 1967-1974.

Chapter 3

Rare-Earth-free Magnets of the $Ti_3Co_5B_2$ structure type $Hf_2MOs_4IrB_2$ and $Hf_2MOs_3Ir_2B_2$ (M = Mn, Fe)

Kate A. Gibson, Boniface P. T. Fokwa

3.1 Abstract

A recent study of the $Ti_3Co_5B_2$ structure type was the first to use osmium in its composition, as opposed to the group 9 metals ruthenium or iridium, and has shown that compositions of $Hf_2MOs_5B_2$ (M = Fe, Mn, or Co) create predominantly antiferromagnets magnets with $Hf_2FeOs_5B_2$ exhibiting hard magnetic behavior. Despite the study illustrating that osmium can be used to obtain hard magnets, the computational results indicated that a harder magnet may be obtainable if more electrons are present. This study computationally investigates the solid solutions of $Hf_2MOs_{5-x}Ir_xB_2$ (M = Mn, Fe) and the DFT calculations indeed confirm that a hard magnet is obtainable with this composition.

3.2 Introduction

Metal borides have been extensively studied with over 150 boride structure types discovered as of 2019.[1] One structure type of particular interest is the $Ti_3Co_5B_2$ structure type which already contained more than sixty phases in 2011.[2, 3] $Sc_3Rh_5B_2$, discovered in 2001, was considered the first successful synthesis of a stoichiometric ternary phase of

the $Ti_3Co_5B_2$ structure type as $Ti_3Co_5B_2$ was initially obtained as a side phase and it was later reinvestigated yielding a non-stoichiometric phase, $Ti_{3-x}Co_{5+x}B_2$ ($x \leq 0.52$).[2, 4-7] Among the more than sixty compositions known less than a dozen are ternaries, due to the fact that in this structure there are two different coordination environments for Ti, i.e. pentagonal Co_{10}-prims and tetragonal Co_8-prisms. These ternary phases have the general formula $A_3T_5B_2$ where A is an early transition metal (Ti, Sc, Nb, Ta, Hf) while T is usually a group 8 or 9 element (Co, Ru, Rh, Ir). Jung et al. realized that stable quaternary compositions could be achieved by using two elements on the two different T positions: a small metal on the tetragonal prism and a larger one on the other. This strategy led to the discovery of phases of the type $A_2MT_5B_2$, where M is smaller transition metal than T.[2] Some of these quaternaries exhibit long-range magnetic order such as antiferromagnetism in $Mg_2MnRh_5B_2$, ferromagnetism in $Sc_2FeRh_5B_2$[4] and $Mg_2FeRh_5B_2$[8] and metamagnetism in $Sc_2MnRh_5B_2$[4] and $Sc_2FeIr_5B_2$[9]. These magnetic properties result from strong intra- and inter-chain M-M interactions at ca. 3.0 Å and 6.5 Å, respectively.[4] Numerous computational studies have also investigated the potential magnetic properties of this structure type.[10, 11]

Multiple quinary series have also been studied to better understand the magnetic properties of this structure type. The $Sc_2FeRu_{5-n}Rh_nB_2$ (n = 0-5) series indicated that as valence electron count increases the materials change from antiferromagnetic to ferromagnetic.[12] This trend was also demonstrated in the theoretical study by Samolyuk et al.[13] A valence electron count of 63 is when ferromagnetism arose, and this pattern has

been part of the foundation of many studies that followed it.[12] The recently studied $Hf_2Fe_{1-d}Ru_{5-x}Ir_{x+d}B_2$ series gave rise to materials with a range of hardness, with $Hf_2FeRu_3Ir_2B_2$ and $Hf_2FeRuIr_4B_2$ being hard magnets, and $Hf_2FeRu_4IrB_2$ and $Hf_2FeRu_2Ir_3B_2$ being semi-hard magnets.[14] This study illustrated how the exchange energy (E_{EX}) and spin-orbit coupling energy (E_{SOC}) can be used to predict the hardness of a material in the $Ti_3Co_5B_2$ structure type. A negative E_{SOC} indicates preference for the easy axis (001 direction) while a positive sign indicates the spins are more oriented to the easy plane. This series showed that for this structure type easy axis anisotropy leads to greater coercivity, and there appears to be a correlation between negative E_{EX} values (indicating antiferromagnetic ordering) and obtaining hard magnets.[14] Another study on $Hf_2MOs_4IrB_2$ (M=Fe, Mn) and $Hf_2MOs_3Ir_2B_2$ (M=Fe, Mn) was the first to use osmium instead of Rh or Ir which are group 9 transition metals (not submitted). The density of states (DOS) calculations in the latter study indicated that adding electrons could lead to increased instability in the non-spin polarized (*nsp*) models, which could suggest greater spin-splitting in spin polarized (*sp*) calculations leading to larger magnetic moments and stronger magnetic interactions (not submitted). Knowing this, and the anisotropy predictions of the $Hf_2Fe_{1-d}Ru_{5-x}Ir_{x+d}B_2$ series, this study computationally investigates solid solutions of $Hf_2MOs_{5-x}Ir_xB_2$ (M = Mn, Fe) and uses the results from the $Hf_2Fe_{1-d}Ru_{5-x}Ir_{x+d}B_2$ series to extrapolate on the potential for hard magnets of this composition.

3.3 Results and Discussion

3.3.1 Experimental

The materials were synthesized by arc-melting, as described in the methods section, and characterized with Powder X-Ray Diffraction (PXRD) and Energy Dispersive X-Ray (EDX) analysis. The PXRD was refined against the respective compositions of $Hf_2MOs_4IrB_2$ or $Hf_2MOs_4IrB_2$ (M = Mn or Fe), taking into account preferred orientation. The refinement assumed stoichiometric amounts of Ir on the Os sites for the mixed occupancy. The main phase, when refined against $Hf_2FeOs_4IrB_2$, $Hf_2FeOs_3Ir_2B_2$, $Hf_2MnOs_4IrB_2$, and $Hf_2MnOs_3Ir_2B_2$ gave yields of 94.5(3)%, 98.4(4)%, 99.2(2)%, and 97.9(4)% respectively. The other major side phase was an osmium phase. There was no significant improvement when the osmium phase was refined with a mixed occupancy of 50% Os/20% Hf/10% Fe/10% Ir, to mirror the composition of $Hf_2FeOs_4IrB_2$. As such, the second phase was refined against only elemental osmium for simplicity. The PXRDs and Rietveld refinement data are given in Figure 1, Figures S3-S5, and Table 1 respectively. What is interesting about the refinement data is for the iron compositions both lattice parameters get larger with more iridium. In the study on the $Hf_2Fe_{1-d}Ru_{5-x}Ir_{x+d}B_2$ series the change in lattice parameters was inversely related – i.e. as one lattice parameter got bigger the other got smaller and vice versa.[14] Considering Os and Ru are both group 8 metals, it would make sense that they should show a similar pattern. On the other hand, for the $Sc_2FeRu_{5-n}Rh_nB_2$ series the general trend is as the a-lattice parameter gets larger, so does the c-lattice parameter.[12] The main difference between the scandium series and

this study is Sc is a group 3 metal while Hf is a group 4 metal. It is possible the other compositions should be studied to gain a better understanding of what is happening.

Table 3.1. Rietveld refinement data of the $Hf_2MOs_4IrB_2$ and $Hf_2MOs_3Ir_2B_2$ (M = Mn, Fe) phases, and lattice parameters of the corresponding lowest energy computational model.

Fixed composition	**$Hf_2MnOs_4IrB_2$**	**$Hf_2MnOs_3Ir_2B_2$**	**$Hf_2FeOs_4IrB_2$**	**$Hf_2FeOs_3Ir_2B_2$**
Space group			*P 4/m b m*	
a (Å)	9.4301(6)	9.4168(6)	9.3935(7)	9.4023(8)
c (Å)	3.0580(2)	3.0649(3)	3.0538(3)	3.0689(3)
Unit cell volume ($Å^3$)	271.93(3)	271.78(3)	269.45(4)	271.30(4)
Formula units per cell			2	
Calculated density (g/cm^3)	21.545	28.784	21.760	28.850
2θ range	5-80	5-80	5-80	5-80
Refinement Range			Least-squares	
Profile Function			Pseudo-voigt	
R_{Bragg}	10.7	12.0	11.3	14.6
R_F	9.51	7.54	6.77	11.1
χ^2	6.4783	7.4568	7.9624	12.7806

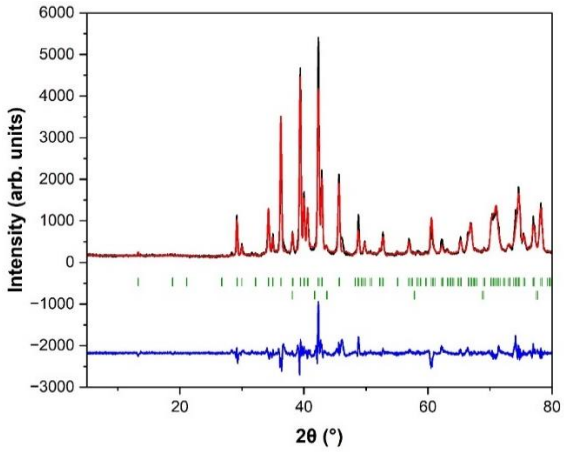

Figure 3.1. Observed (black) and calculated (red) powder X-ray diffraction pattern with starting stoichiometry $Hf_2MnOs_4IrB_2$ with boron 120%. The position of the Bragg reflections (green): $Hf_2MnOs_4IrB_2$ (top row) and Os (bottom row). Difference curve (blue) obtained from Rietveld refinement.

Energy Dispersive X-Ray (EDX) Spectroscopy was used to qualitatively confirm the stoichiometric ratios of the elements in each sample. These are illustrated in Figure 2 and Figures S6-S8 which illustrate the ratios of the elements in the EDX analysis reflects the expected stoichiometric ratio for all four compositions.

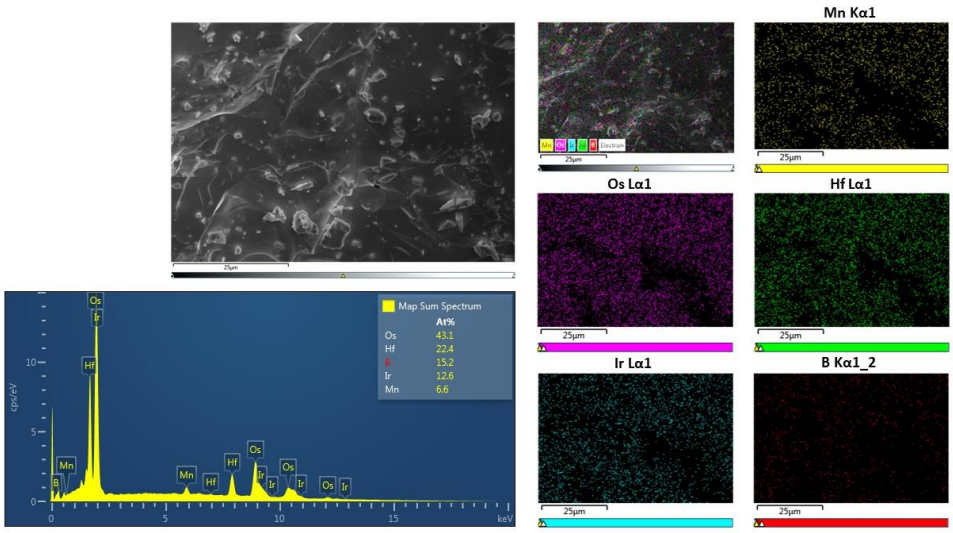

Figure 3.2. EDX spectrum and elemental mapping of $Hf_2MnOs_4IrB_2$

3.3.2 Computational Analysis

In the study conducted by Luong et al.[14] the exchange energy (E_{EX}) and spin orbit coupling energy (E_{SOC}) are evaluated for the $Hf_2FeRu_{5-x}Ir_xB_2$ (x = 0 – 5) series. In this series as x decreases, with the exception of x = 1, E_{EX} and T_C decreases and E_{EX} becomes negative at x = 2.

In this study, three models of $Hf_2FeOs_3Ir_2B_2$ were analyzed (Figure S1). Since the energy differences between AFM, FM, and *nsp* were similar across models, the model with the lowest FM energy was used to compare with $Hf_2FeRu_3Ir_2B_2$. The $Hf_2FeOs_3Ir_2B_2$ model resulted in a preference for AFM ordering and a E_{EX} of -35.80 meV/f.u. and E_{SOC} of -4.27 meV/f.u. For $Hf_2FeRu_3Ir_2B_2$ the E_{EX} is -15.62 meV/f.u. and E_{SOC} is -0.75 meV/f.u. Given both values are negative for both compositions, this would indicate a preference for antiferromagnetic ordering which is desirable to obtain a high coercivity in this structure type per the study by Luong et al.[14] The large and negative E_{SOC} and E_{EX} values of $Hf_2FeOs_3Ir_2B_2$ would suggest a higher coercivity than any value of the $Hf_2FeRu_{5-x}Ir_xB_2$ composition – the highest value of which was 74.0 kA/m at 5 K for $Hf_2FeRu_3Ir_2B_2$.[14]

$$E_{SOC} = E_{SOC}\|c - E_{SOC}\perp c \quad \textbf{(Eqn. 1)}$$

$$E_{EX} = E_{AFM1} - E_{FM} \quad \textbf{(Eqn. 2)}$$

3.4 Conclusion

This study has experimentally synthesized, and computationally analyzed the magnetic properties of $Hf_2MOs_4IrB_2$ (M = Mn, Fe) and $Hf_2MOs_3Ir_2B_2$ (M = Mn, Fe). PXRD and

EDX confirmed the successful synthesis of the novel compositions – the first to contain osmium and iridium in the $Ti_3Co_5B_2$ structure type. Computational data and experimental observations would indicate a high likelihood that the iron compositions will be ferromagnetic. Magnetic measurements will need to be executed to further understand the magnetic hardness, T_C, and magnetic characteristics of the novel materials. These measurements are currently being investigated.

3.5 Methods

3.5.1 Experimental Methods

The materials were synthesized by first mixing the respective elemental powders according to the stoichiometric ratios $Hf_2MOs_4IrB_2$ (M=Fe, Mn) and $Hf_2MOs_3Ir_2B_2$ (M=Fe, Mn), except for boron where 120% of the stoichiometric amount was weighed, in a glove box. Starting materials consisted of Fe (99+%, Alfa Aesar), Mn (≥99%, Aldrich), Hf (99.6%, Alfa Aesar), Os (99.8%, Thermo Scientific), and B (95-97% amorphous, Thermo Scientific). The powders were then ground and mixed before being pressed into pellets. Each pellet was then arc-melted for 2-3 seconds in a water-cooled copper crucible under an Ar atmosphere (99.995 %, Airgas) using a tungsten electrode at 20–30 V and 40 A. The metallic beads were then crushed and ground for Powder X-ray Diffraction (PXRD) analysis in a Rigaku Miniflex 600 diffractometer with Cu-Kα1 (λ=1.540593 Å) radiation. Rietvelt refinement was applied to refine the lattice parameters and identify the phases present in the products.[15] The chemical composition of the products were also analyzed using energy dispersive X-ray (EDX) spectroscopy on a Tescan Vega3 SBH

with Bruker LN2-free high resolution and a high-speed 30 mm^2 SD detector. For EDX analysis the energy resolution was ≤ 129 eV at Mn-Kα, and the window of detection was from boron to californium.

3.5.2 Computational Methods

The structural model was prepared from the known $Hf_2FeOs_5B_2$ structure from the previous study, and the atoms were adjusted to reflect the expected composition of $Hf_2FeOs_3Ir_2B_2$. In the $Hf_2Fe_{1-d}Ru_{5-x}Ir_{x+d}B_2$ series there is Ru and Ir mixed occupancy on the *2d* and *8i* sites.[14] Building off this knowledge, this computational study assumes no site preference. This was accomplished by having one of the two *2d* sites and three of the *8i* sites be Ir, leading to a computational stoichiometry of $Hf_2FeOs_3Ir_2B_2$. Computational models of $Hf_2FeOs_4Ir_1B_2$ were not studied as there is no way to get close to the desired osmium-iridium ratio while maintaining no site preference. For energy calculations, the lattice parameters, cell shape, cell volume, and atomic positions were allowed to relax using the projector augmented wave method in the Vienna Abinitio Simulation Package (VASP).[16] All VASP calculations employed the generalized gradient approximation (GGA) with exchange and correlation utilizing the Perdew, Burke and Ernzerhof (PBE) functional.[17] The cutoff energy was 450 eV, and the global break condition for the electronic SC-loop (E_{diff}) was 1E-06. The k-point mesh was a 7×7×19 Monkhorst-Pack grid. The magnetic calculations were performed by inputting initial magnetic moments onto the iron atoms for all steps, including relaxation calculations. Upon relaxing, self-

consistency (SC) calculations were run. The model with the lowest FM energy also had spin-orbit coupling (SOC) calculations executed.

3.6 Acknowledgements

The authors would like to acknowledge the financial support from UC Riverside and the NSF (Career grant to B.P.T.F., DMR 1654780).

3.7 References

1. Iyer, A. K.; Zhang, Y.; Scheifers, J. P.; Fokwa, B. P. T., Structural variations, relationships and properties of M2B metal borides. *Journal of Solid State Chemistry* **2019,** *270*, 618-635.

2. Hermus, M.; Geier, D.; Fokwa, B. P. T., Nb3Ru5B2 – The First Fully Characterized Ternary Phase in the Nb-Ru-B System: Synthesis, Crystal Structure, and Bonding Analysis. *Zeitschrift für anorganische und allgemeine Chemie* **2012,** *638* (1), 49-52.

3. Scheifers, J. P.; Zhang, Y.; Fokwa, B. P. T., Boron: Enabling Exciting Metal-Rich Structures and Magnetic Properties. *Accounts of Chemical Research* **2017,** *50* (9), 2317-2325.

4. Nagelschmitz, E. A.; Jung, W.; Feiten, R.; Müller, P.; Lueken, H., Ternary Rhodium Borides A3Rh5B2 (A=Mg, Sc) and Quaternary Derivatives A2MRh5B2. Preparation, Crystal Structure (M=Main Group and 3d Elements), and Magnetism (M=Mn, Fe). *Zeitschrift für anorganische und allgemeine Chemie* **2001,** *627* (3), 523-532.

5. Kuz'ma, Y. B.; Yarmolyuk, Y. P., Crystal structure of the compound Ti3Co5B2. *Journal of Structural Chemistry* **1971,** *12* (3), 422-424.

6. Xie, W.; Fuccillo, M. K.; Phelan, B. F.; Luo, H.; Cava, R. J., Stabilization of the Ti3Co5B2-type structure for Ti3−xSixRu5B2 through Si–Ti substitution. *Journal of Solid State Chemistry* **2015,** *227*, 92-97.

7. Shankhari, P.; Zhang, Y.; Stekovic, D.; Itkis, M. E.; Fokwa, B. P. T., Unexpected Competition between Antiferromagnetic and Ferromagnetic States in Hf2MnRu5B2: Predicted and Realized. *Inorganic Chemistry* **2017,** *56* (21), 12674-12677.

8. Feiten, R.; Lueken, H.; Nagelschmitz, E. A.; Jung, W., Magnetismus von Fe- und Mn-Ketten in Mg2FeRh5B2 bzw. In *Kurzreferate / Fachgruppe Festkörperchemie, Gesellschaft Deutscher Chemiker : Vortragstagung Band: 8*, Germany, 1996.

9. Nagelschmitz, E. A.; Jung, W., Scandium Iridium Boride Sc3Ir5B2 and the Quaternary Derivatives Sc2MIr5B2 with M = Be, Al, Si, Ti, V, Cr, Mn, Fe, Co, Ni, Cu, Ga, or Ge: Preparation, Crystal Structure, and Physical Properties. *Chemistry of Materials* **1998,** *10* (10), 3189-3195.

10. Burghaus, J.; Dronskowski, R.; Miller, G. J., Slater–Pauling behavior within quaternary intermetallic borides of the Ti3Co5B2 structure-type. *Journal of Solid State Chemistry* **2009,** *182* (10), 2613-2619.

11. Zhang, Y.; Miller, G. J.; Fokwa, B. P. T., Computational Design of Rare-Earth-Free Magnets with the Ti3Co5B2-Type Structure. *Chemistry of Materials* **2017,** *29* (6), 2535-2541.

12. Fokwa, B. P. T.; Lueken, H.; Dronskowski, R., Rational Synthetic Tuning between Itinerant Antiferromagnetism and Ferromagnetism in the Complex Boride Series Sc2FeRu5−nRhnB2 (0≤n≤5). *Chemistry – A European Journal* **2007,** *13* (21), 6040-6046.

13. Samolyuk, G. D.; Fokwa, B. P. T.; Dronskowski, R.; Miller, G. J., Electronic structure, chemical bonding, and magnetic properties in the intermetallic series ${\mathrm{Sc}}_{2}\mathrm{Fe}{({\mathrm{Ru}}_{1\ensuremath{-}x}{\mathrm{Rh}}_{x})}_{5}{\mathrm{B}}_{2}$ from first principles. *Physical Review B* **2007,** *76* (9), 094404.

14. Luong, D.; Schumacher, L.; Kilic, S.; Haddon, E.; Pöttgen, R.; Fokwa, B. T. P., Enhancing Intrinsic Magnetic Hardness by Modulating Antagonistic Interactions in the Rare-Earth-Free Magnetic Solid Solution Hf2Fe1− δ Ru5− x Ir x + δ B2. *Chemistry – A European Journal* **2023,** *n/a* (n/a), e202303381.

15. Rodriguez-Carvajal, J. In *FULLPROF: a program for Rietveld refinement and pattern matching analysis*, satellite meeting on powder diffraction of the XV congress of the IUCr, Toulouse, France:[sn]: 1990.

16. Kresse, G.; Joubert, D., From ultrasoft pseudopotentials to the projector augmented-wave method. *Physical Review B* **1999,** *59* (3), 1758-1775.

17. Perdew, J. P.; Burke, K.; Ernzerhof, M., Generalized Gradient Approximation Made Simple. *Physical Review Letters* **1996,** *77* (18), 3865-3868.

3.8 Supplementary Material

Table S3.1. Total Energies for the different magnetic models relative to the lowest energy (FM = ferromagnetic, AFM = antiferromagnetic, NM = nonmagnetic).

	FM (meV/f.u.)	AFM (meV/f.u.)	NM (meV/f.u.)
Model 1	+38.60	0	+848.18
Model 2	+35.80	0	+851.88
Model 3	+37.94	0	+841.58

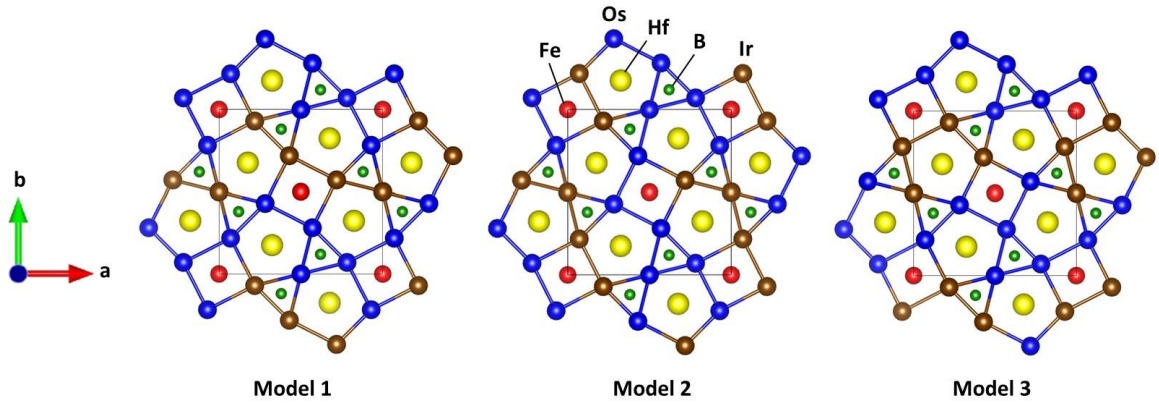

Figure S3.1. The three computational models of $Hf_2FeOs_3Ir_2B_2$.

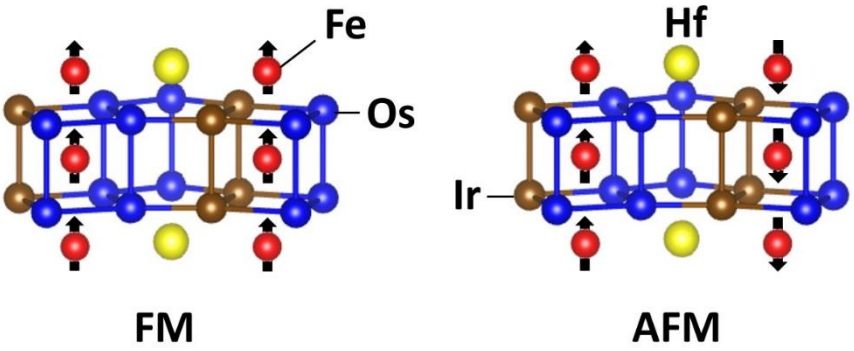

Figure S3.2. Illustration of the magnetic models using ferromagnetic chains of Fe.

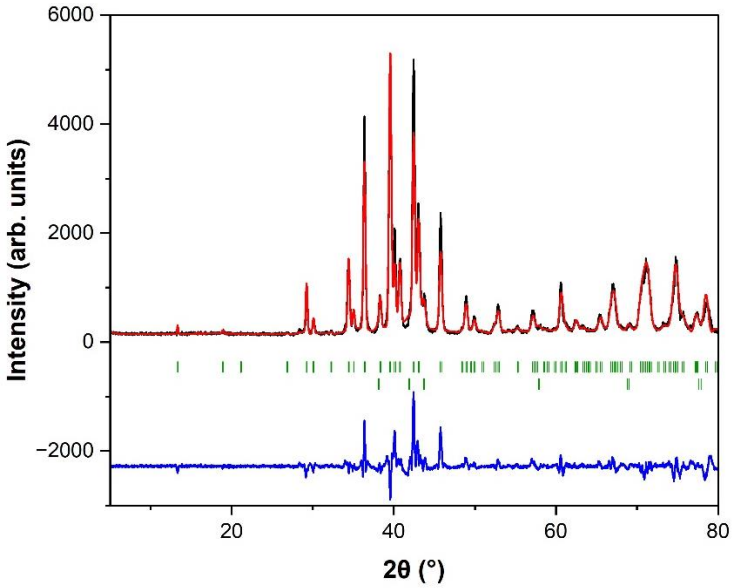

Figure S3.3. Observed (black) and calculated (red) powder X-ray diffraction pattern with starting stoichiometry $Hf_2FeOs_4IrB_2$ with boron 120%. The position of the Bragg reflections (green): $Hf_2FeOs_4IrB_2$ (top row) and Os (bottom row). Difference curve (blue) obtained from Rietveld refinement.

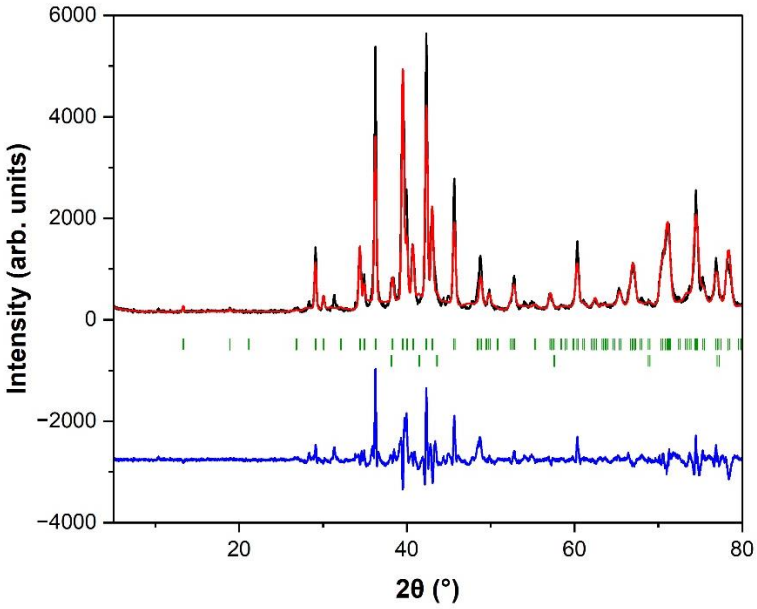

Figure S3.4. Observed (black) and calculated (red) powder X-ray diffraction pattern with starting stoichiometry $Hf_2FeOs_3Ir_2B_2$ with boron 120%. The position of the Bragg reflections (green): $Hf_2FeOs_3Ir_2B_2$ (top row) and Os (bottom row). Difference curve (blue) obtained from Rietveld refinement.

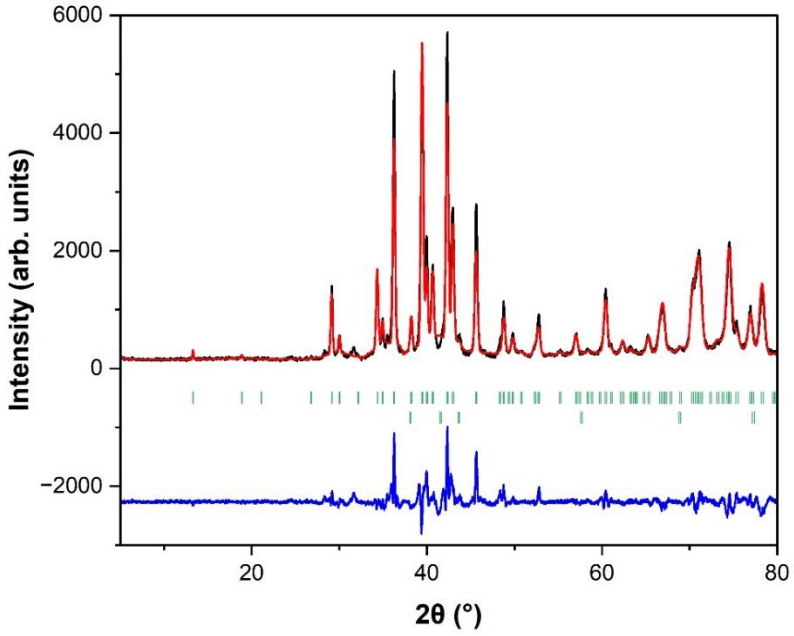

Figure S3.5. Observed (black) and calculated (red) powder X-ray diffraction pattern with starting stoichiometry $Hf_2MnOs_3Ir_2B_2$ with boron 120%. The position of the Bragg reflections (green): $Hf_2MnOs_3Ir_2B_2$ (top row) and Os (bottom row). Difference curve (blue) obtained from Rietveld refinement.

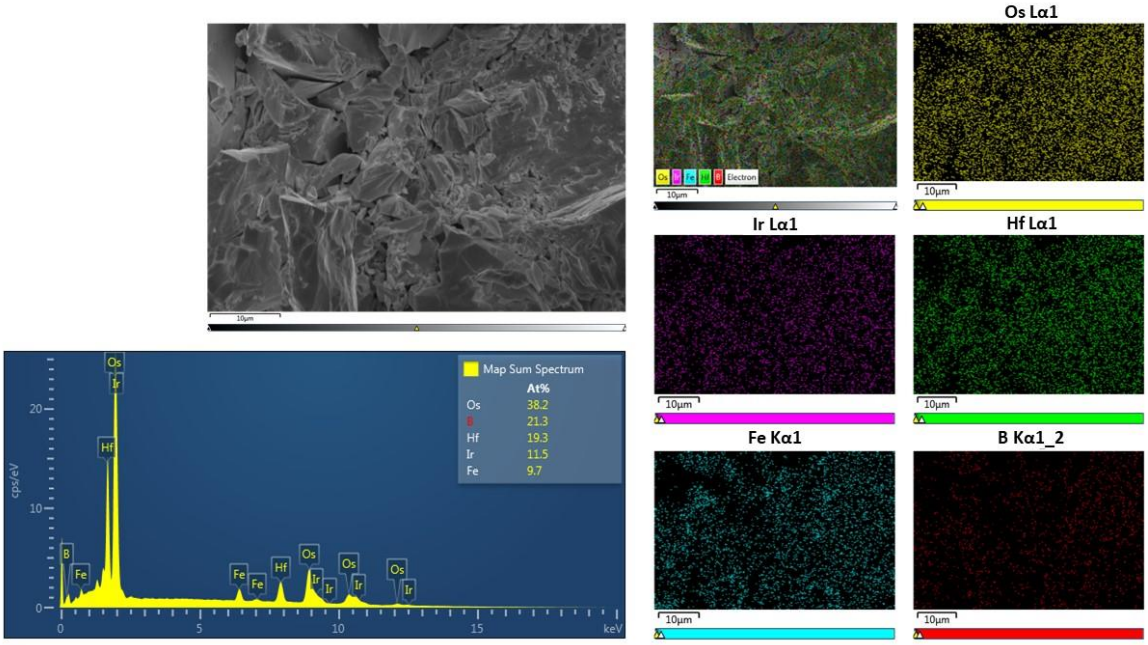

Figure S3.6. EDX spectrum and elemental mapping of $Hf_2FeOs_4IrB_2$

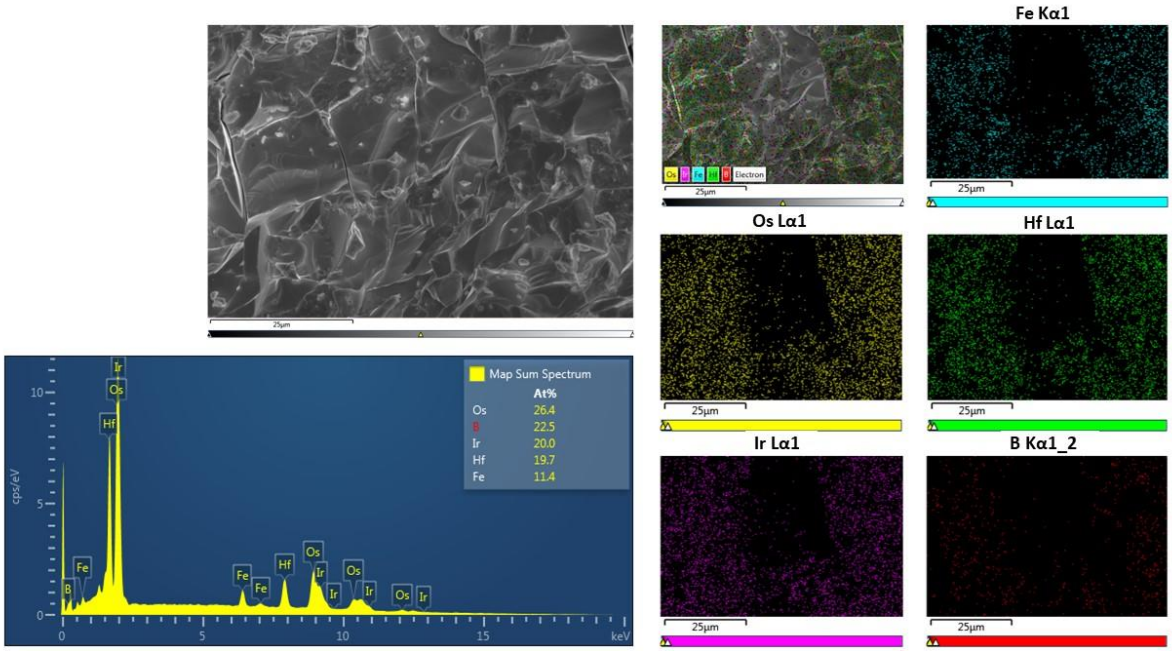

Figure S3.7. EDX spectrum and elemental mapping of $Hf_2FeOs_3Ir_2B_2$

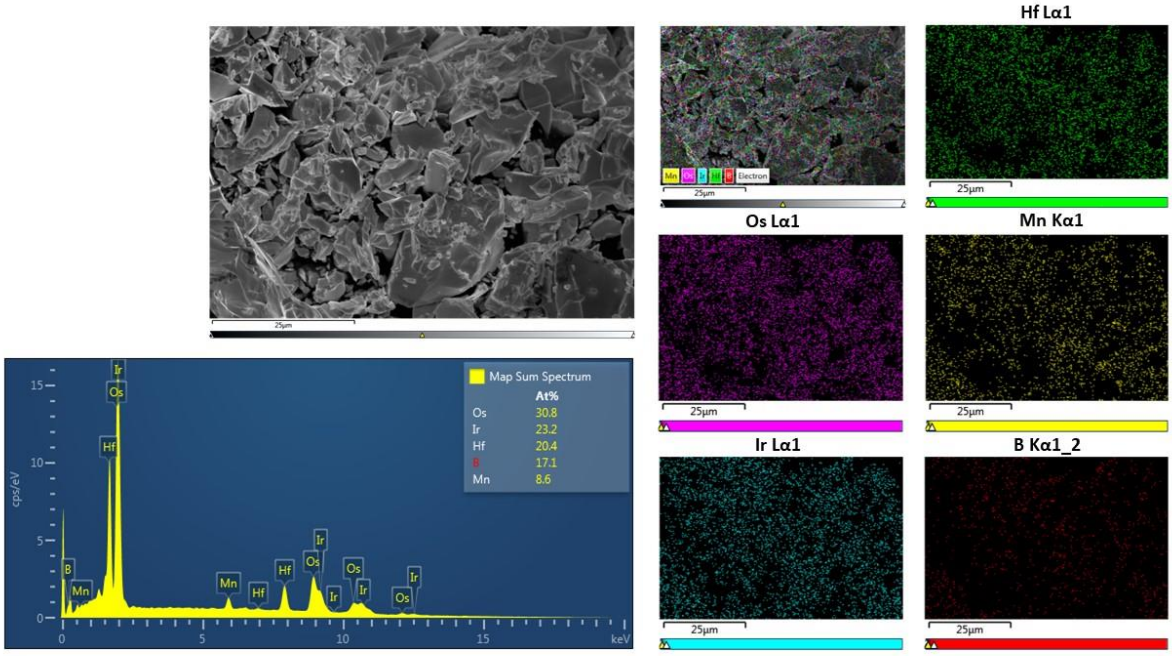

Figure S3.8. EDX spectrum and elemental mapping of $Hf_2MnOs_3Ir_2B_2$

Chapter 4

The First Quaternary Phase of the NbRuB Structure Type: Experimental and Computational Investigations of $TiFe_{1.3}Os_{3.9}B_{2.8}$

Kate A. Gibson, Michael Küpers, Dr. Boniface P. T. Fokwa

4.1 Abstract

The novel composition – $TiFe_{1.3}Os_{3.9}B_{2.8}$ – is the first quaternary phase of the NbRuB structure type. The layer-like structure consists of boron (mixed with 8 % Fe) dumbbells in the same layer as osmium atoms, some sites with mixed occupancies. The second layer has isolated boron, osmium/titanium (51 % Os) and iron atoms. The presence of iron enables the study of magnetism as Fe-chains are present, with intra- and interchain distances of 3.02 Å and 5.76 Å, respectively. Density functional theory (DFT) predicts magnetic ordering to be likely with the antiferromagnetic ground state only 13 meV more favorable than the ferromagnetic state. This discovery opens the possibilities of studying various quaternary compositions in the superconducting NbRuB structure type.

4.2 Introduction

Borides have been studied for several decades due to their broad range of applications, and the interesting chemical and physical properties that arise when the electron deficient boron bonds to metals. Boron icosahedral compounds have large

Seebeck coefficients and small thermal conductivities, making them ideal candidates for high-temperature thermoelectric applications.[1] Specifically, transition-metal (TM) borides are of particular interest due to having high hardness, chemical inertness, metallic conductivity, refractory behavior, superconductivity, and magnetic ordering.[2-4] However, the structural diversity of borides is one of the many reasons why they are challenging to synthesize, especially as single crystalline phases suitable for investigating physical properties. Thus alternative synthetic methods are being developed to synthesize these materials.[3]

Roughly 130 metal borides with a metal to boron ratio M : B=2 : 1 were discovered as of 2019, and more have been reported since.[4] Despite the high metal content in these phases, some structures have been reported to contain B_2 dumbbells,[5, 6] B_4 zigzag fragments,[7-9] trigonal planar B_4 fragments,[10] B_5 zigzag fragments,[11] B_6 rings,[12] and even boron chains.[13, 14] The structural diversity of this M_2B composition is well illustrated by the ternary NbMB (M=Fe, Ru and Os) compounds which build three different structure types. The hexagonal NbFeB structure (ZrNiAl structure type)[15] contains only isolated boron atoms while the orthorhombic NbRuB (own structure type)[6] contains isolated boron atoms and B_2 dumbbells. NbOsB has two modifications: The first was reported to crystallize with $Ti_{1+x}Rh_{2-x+y}Ir_{3-y}B_3$ structure type[8, 17] and contains isolated boron atoms and B_4 zigzag fragments, while the second, HT-NbOsB, has its own structure type (space group *Pnma*) in which isolated boron atoms and B-chains are found. Exciting properties have already emerged from these structures, especially the non-centrosymmetric superconductor NbRuB which has garnered a lot of

attention.[16, 18] However, magnetic ordering in metal borides with these three structure types is yet to be realized. The hexagonal $Ti_{1.6}Os_{1.4}RuB_2$ structure type,[10] which is closely related to the $Ti_{1+x}Rh_{2-x+y}Ir_{3-y}B_3$-type and contains trigonal planar B_4 fragments, has produced the $TiCrIr_2B_2$ ferrimagnet[19] and the $TiFe_{1-x}Os_{2+x}B_2$ ($x\approx1/3$) ferromagnet.[20] $TiFe_{1-x}Os_{2+x}B_2$ was the first quaternary composition containing titanium, osmium, iron, and boron and its exciting magnetic properties such as the high curie temperature of 523(2) K and large Weiss constant of 554(3) K encouraged us to explore this quaternary system in search of new members. Indeed a new structure type was reported recently by preparing $Ti_{5-x}Fe_{1-y}Os_{6+x+y}B_6$ ($0 < x,y <1$), which can be derived from HT-NbOsB by chemical twinning, and it contains isolated boron atoms, zigzag boron chains and iron chains in its structure.[13] The present study discusses the third composition in this quaternary system, $TiFe_{1.3}Os_{3.9}B_{2.8}$, which represents the first quaternary phase of the NbRuB structure type, in which the ruthenium atoms are replaced with osmium, and the niobium atoms are replaced with iron at one site and almost 50 : 50 mixed occupancy of titanium and osmium at another. Density functional theory (DFT) calculations were applied to study its electronic structure, chemical bonding and magnetic properties.

4.3 Results and Discussion

4.3.1 X-ray diffraction and structure analysis

The powder X-ray diffraction (PXRD) data (Figure S1) from the "$TiFe_2Os_3B_3$" starting stoichiometry shows three phases; elemental osmium and phases from the $Ti_{1+x}Rh_{2-x+y}Ir_{3-y}B_3$ and NbRuB structure types. There are also some unidentified peaks, possibly due to another new phase. Further syntheses were attempted using near single-crystal stoichiometry of "$TiFe_{1.5}Os_{3.5}B_3$", followed by the single-crystal stoichiometry of $TiFe_{1.3}Os_{3.9}B_{2.8}$. The "$TiFe_{1.5}Os_{3.5}B_3$" sample did show a clearer PXRD after HCl treatment (Figure S2), with the desired phase being about 36(2) wt.% of the product. However, peaks of elemental Os and some unidentified peaks were still present. The absence of the $Ti_{1+x}Rh_{2-x+y}Ir_{3-y}B_3$-type phase in the "$TiFe_{1.5}Os_{3.5}B_3$" diffractogram indicated an improved synthesis. When the single-crystal starting stoichiometry was used, the $Ti_{1+x}Rh_{2-x+y}Ir_{3-y}B_3$-type phase was also absent from the diffractogram and the phase fraction increased to 40(2) wt.% of the product (Table S1), confirming the improved synthesis. However, single crystals were obtained only from the "$TiFe_2Os_3B_3$" starting composition. The refined lattice parameters from the single-crystal X-ray diffraction (SCXRD) data, a=10.841(9) Å, b=3.021(3) Å and c=6.201(5) Å, are in good agreement with those from the PXRD (a=10.866(2) Å, b=3.0248(4) Å and c=6.218(2) Å). Also, they are smaller than those of NbRuB, a=10.870(2) Å, b=3.173(1) Å and c=6.350(2) Å.[6] Considering the similarities of the atomic radii of Nb (1.429 Å) vs. Ti (1.448 Å), and Ru (1.325 Å) vs. Os (1.338 Å), the decrease in the lattice parameters occurs due to iron

(1.241 Å) substituting for the larger Nb. The crystal structure was solved by direct methods using the collected SCXRD data (Table 2.1). The proposed structure model matched very well with the atomic arrangement from the NbRuB structure type (space group *Pmma*, no. 51) as proposed by the PXRD. As Table 2 shows, the light transition metals (Ti and Fe) were found on the Nb sites (4j and 2 *f*) while the heavier metal (Os) was found mainly on the Ru sites (4*i* and 2*e*). However, given that Nb and Ru are 4d transition metals and are being replaced by 3d and 5d transition metals, mixed occupancies were inevitable. Indeed, mixed occupancies were detected for two metal sites, Os1 on 2*e* (mixed with 11 % Fe) and Ti3 on 4j (mixed with 51 % Os). The Fe site (2 *f*), when refined freely showed 90 % occupancy, but the standard deviation of one anisotropic displacement parameter became larger than the actual value and the *R* values did not improve. Also, a mixed occupancy refinement using any of the possible three elements did not change the result. Consequently, full occupancy was maintained for the iron site. The Fe-atoms build chains that are like those previously found in similar phases, with intra- and interchain distances of 3.02 Å (*b* lattice parameter, Figure 1) and 5.76 Å, respectively. Such chains are known to enable magnetic ordering in these phases,[4b] and thus will be further investigated theoretically (see theory section). The two boron positions were easily located in the difference Fourier map (showing two similar electron densities of 10 and 11 $e^{-}/Å^{3}$) after identifying all metal positions. While the boron dumbbell distance (B2-B2) was somewhat large (1.99(7) Å, see Table S2.2), it is still (within standard deviation) in the range of B−B distances (1.76 Å–1.90 Å) found in NbRuB and other borides containing boron fragments.[4a, 5-12] Given that a boron/metal

mixed occupancy has been observed in some metal borides such as $Hf_2Ir_{5+\delta}B_{2-2\delta}$,[21] $Mn_{3-x}Ir_5B_{2+x}$,[22a] and $Ti_{3-x}Ru_{5-y}Ir_yB_{2+x,}$[22b] we freely refined the occupancies of B1 (2 *f*) and B2 (4*i*): While the B1 site was fully occupied the B2 site was about 92 % occupied and a subsequent mixed occupation with 8 % Fe (smallest of the three, metals) improved the *R* values and the isotropic displacement parameters significantly. In fact, the displacement parameter of B2 showed a significantly improved standard deviation. All metal atoms were refined anisotropically while the boron atoms were refined isotropically (Table S3). The final refinement led to the composition $Ti_{0.99(1)}Fe_{1.27(2)}Os_{3.90(2)}B_{2.84}$, simplified as $TiFe_{1.3}Os_{3.9}B_{2.8}$ in the document and SI (Figure 1). The composition is not generalized as only one single crystal was obtained that was good enough for structure determination. Energy dispersive X-ray (EDX) spectroscopy was carried out, but due to the uneven surface of the crystal only a qualitative analysis was possible, which confirmed the presence of all elements (Figure S3). Even an attempt to quantify only the metal content failed, as far more titanium (Ti : Fe ratio was approximately 3 : 1, Table S4) was found than expected from both the refinement and the starting composition.

Table 4.1. Single-crystal refinement results for $TiFe_{1.3}Os_{3.9}B_{2.8}$.

Refined chemical formula	**$Ti_{0.99(1)}Fe_{1.27(2)}Os_{3.90(2)}B_{2.84}$**
Formula weight [g/mol]	890.87
Crystal system, space group	orthorhombic, *Pmma*, no. 51
Lattice parameters	a = 10.841(9) Å,
Volume [Å^3], Z	203.1(3), 2
Density [g/cm^3]	14.57
Absorption coefficient [mm^{-1}]	127.58
F (000)	731
Crystal size [mm^3]	0.05×0.03×0.01
Θ range [°]	3.28 to 30.83
hkl ranges	-15 ≤ h ≤ 15
Reflections [collected/independent/R_{int}]	2177/370/0.1360
Data/ parameters	370/ 28
Goodness-of-fit on F^2	1.093
Final R indices [I>2 sigma(I)]	R_1 = 0.0509, wR_2 = 0.0862
R indices (all data)	R_1 = 0.0801, wR_2 = 0.0962
Extinction coefficient	0.0038(6)
Largest diff. Peak/hole [e-/Å^3]	4.58/-5.78
CSD Deposition number	2270489

Table 4.2. Wyckoff sites, fractional coordinates, occupancy, and equivalent (isotopic for boron) displacement parameters for $TiFe_{1.3}Os_{3.9}B_{2.8}$.

site	Wyckoff site	x/a	y/b	z/c	Occupancy [%]	U_{eq} [Å^2]
Os1/Fe1	2*e*	3/4	0	0.1870(3)	89(2)/11	0.0076(7)
Os2	4*i*	0.6199(2)	0	0.5680(2)	100	0.0082(5)
Os3/Ti3	4*j*	0.5413(2)	-1/2	0.1945(4)	51(1)/49	0.0125(8)
Fe4	2*f*	3/4	-1/2	-0.157(2)	100	0.019(2)
B1	2*f*	3/4	-1/2	0.45(1)	100	0.033(7)
B2/Fe2	4*i*	0.586(3)	-1	-0.055(6)	92/8	0.033(7)

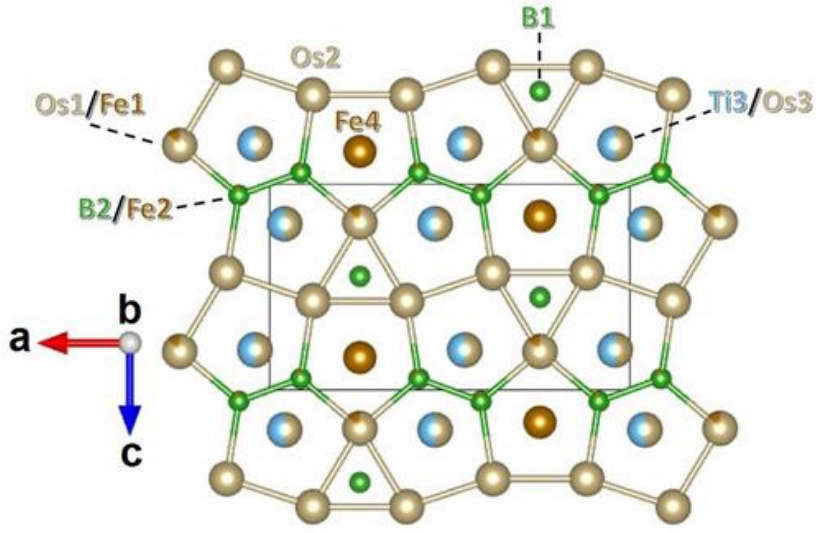

Figure 4.1. Projected crystal structure of $TiFe_{1.3}Os_{3.9}B_{2.8}$ as obtained from single-crystal refinement.

Figure 4.2 shows the coordination geometries around the Fe4 and Ti3/Os3 sites. Both polyhedra have the central atom coordinated to four Os2 atoms, four B2/Fe2 atoms, and two Os1/Fe1 atoms, but they are differently shaped pentagonal prisms. Additionally, the Os3/Ti3 polyhedron is capped by an Os3/Ti3 site at 2.573(6) Å, a distance much shorter than those connecting Os3/Ti3 to the Os2 sites [2.739(3) and 2.894(3) Å]. Therefore, the Os3/Ti3 polyhedron is distorted and Os3/Ti3 is shifted from the center due to the proximity of the capping Os3/Ti3 site. Consequently, the capping Os3/Ti3 site contributes to enlarging the polyhedron if compared to the similar but uncapped Fe4 polyhedron, a fact which is also in agreement with the size difference between Ti/Os and Fe atoms. The capping affects the distances around the Os3/Ti3 site which is only 2.22(4) Å away from B2/Fe2, while in the Fe4 polyhedron the Fe4 site is 2.42(3) Å away from B2/Fe2.

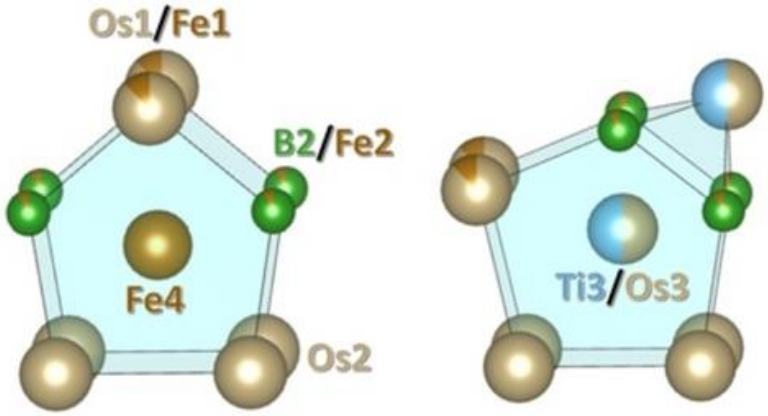

Figure 4.2. Coordination polyhedra around the Fe4 (left) and Ti3/Os3 (right) sites in the crystal structure of $TiFe_{1.3}Os_{3.9}B_{2.8}$.

4.3.2 Electronic structure, chemical bonding, and magnetism

Theoretical calculations, as implemented in the Vienna *ab-initio* software package (VASP), were carried out according to the procedures given in the computational methods section below and using the ideal $TiFeOs_4B_3$ composition. Because of the Os : Ti mixed occupancy of 0.51:0.49 found experimentally on the 4j site, two structure models, based on the equal distribution of titanium and osmium on these four positions (in the primitive triclinic cell), were relaxed and the lowest energy structure was 236 meV/f.u. more favorable than the other structure (Figure S4). The low energy structure was used to conduct all following calculations and plots. The resulting non-spin polarized (*nsp*) and spin polarized (*sp*) density of states (DOS) are plotted in Figure 2.3 and Figure S2.5. In the *nsp* DOS, Os and Fe contribute almost equally at (and near) the Fermi energy (E_F). The non-zero DOS at E_F indicates metallic behavior, as expected for this metal-rich boride. The Fermi energy also lies on a peak, which is associated with electronic instability due either to a potential structure distortion or to the presence of magnetic interactions. When spin polarization is applied, a large spin splitting is observed, thereby lowering the total energy, and shifting E_F to a smaller peak. Such a behavior indicates the presence of strong magnetic interactions and the large energy difference (258 meV/f.u.) favors magnetic ordering over the nonmagnetic state. This pattern is reminiscent of the $TiFe_{1-x}Os_{2+x}B_2$, $Ti_{5-x}Fe_{1-y}Os_{6+x+y}B_6$, and other intermetallic phases, where magnetic ordering has been observed or predicted.[13, 20, 23, 24] Iron and osmium contribute the most at the Fermi energy, and only Fe has a significant α (majority) and β (minority) spin split indicating it is likely responsible for the electronic stabilization of the structure through

magnetic Fe−Fe interactions. While the stabilization of the electronic structure can be explained by the presence of magnetic interactions in the crystal structure, it is worth noting that bonding optimization due to mixed occupations not considered theoretically (Os/Fe and B/Fe) can also contribute significantly (see bonding discussion below).

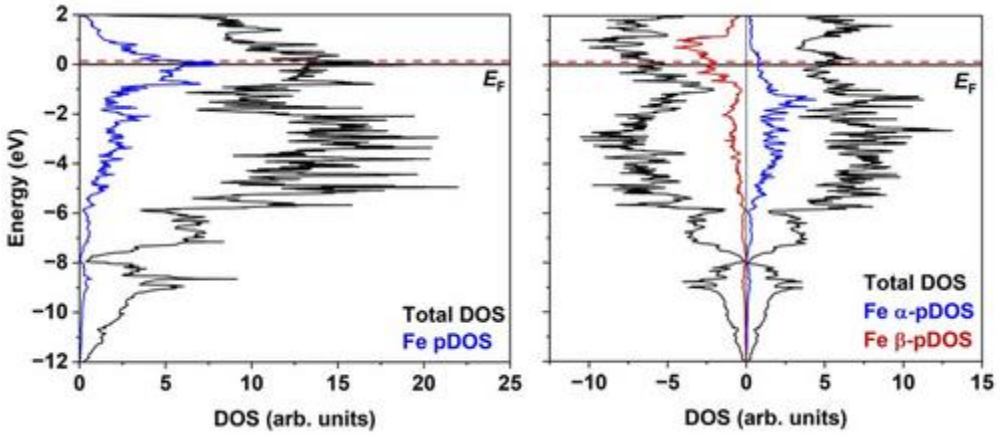

Figure 4.3. Total (black) and partial (colored) non-spin polarized (left) and spin-polarized (right) density of states (DOS) plots for a unit cell of $TiFeOs_4B_3$. Fermi energy (E_F, black line) set at 0 eV, the red dashed line is the projected E_F of the experimental composition.

To find out the nature of magnetic interactions, different magnetic ordering models were tested. Given the numerous examples of magnetic studies of iron chains in metal borides, we have limited our analysis to the most common and stable models found – ferromagnetic (FM), and antiferromagnetic (AFM) where two FM Fe-chains are aligned antiferromagnetically to each other (Figure S2.6). The AFM model has the lowest energy and thus is the ground state. The calculated magnetic moment per iron atom is about 2.09 μ_B in the FM model and about 2.16/−2.16 μ_B in the AFM model. Interestingly, the FM model is only 13 meV less stable than the AFM model. Considering recent studies such as $A_2MRu_5B_2$ (A=Zr, Hf; M=Mn, Fe),[25] $Ti_{5-x}Fe_{1-y}Os_{6+x+y}B_6$[13] and $TiFe_{1-x}Os_{2+x}B_2$,[20] where

such small energy differences were also found between the same types of AFM and FM models, and that in many cases a variation in either the external magnetic field or the composition led to ferromagnetic ordering being favored experimentally, it is likely that our synthesized phase could be dominated by ferromagnetic interactions as the mixed occupations observed experimentally and involving Fe could not be modeled theoretically. Furthermore, the experimental composition, $TiFe_{1.3}Os_{3.9}B_{2.8}$, has 108 valence electrons (VE) per unit cell, i.e. 2 VE more than the ideal composition ($TiFeOs_4B_3$ used for calculations), which assuming a valid rigid band model would shift the Fermi energy (E_F) by +0.12 eV (Figure 2.3, red dashed line). The so-derived experimental E_F would still be positioned in a region of high electron density; consequently, the interpretation of the magnetic data will remain unchanged, thereby also predicting magnetic ordering for the experimental composition (see also pCOHP discussion below).

Chemical bonding and magnetic interactions were analyzed by the projected Crystal Orbital Hamilton Populations (−pCOHP is plotted) using the ideal composition $TiFeOs_4B_3$. A negative -pCOHP value accounts for antibonding interactions, while a positive value indicates bonding interactions (Figures 2.4 and S2.7). The integrated pCOHP (pICOHP, negative values) provides a framework to measure the strength of covalent bonding in solids and was performed on the nonmagnetic and spin polarized models. The higher the pICOHP (absolute value), the greater the covalency contribution of that bond. According to the values given in Table S4.5, the highest pICOHP

contribution came from the Os−B interactions followed by mainly the other boron-based interactions Ti−B and Fe−B. The heteroatomic all-metal Ti−Os, Fe−Os interactions were the next highest and decreased in this order. These interactions constitute the backbone of the structure and are in line with all reported metal borides of these elements to date, including $Ti_{5-x}Fe_{1-y}Os_{6+x+y}B_6$[13] and $TiFe_{1-x}Os_{2+x}B_2$.[20] All but Os−Os (Figure S2.7) homoatomic all-metal interactions are weak while the boron-boron interaction is even weaker than the Os−Os due to the very large B−B distance. Given that the experimental B−B distance was much smaller [1.99(7) Å vs. 2.605 Å in the AFM model], we have tested another structure relaxation model by fixing this B−B distance only (Table S4.6). While convergence could be achieved, this model was energetically less favorable than a fully relaxed model, suggesting that the boron site (B2) in this structure may not be fully occupied by boron only, in agreement with the experimental mixed-occupancy refinement. It is worth mentioning that a structure relaxation (VASP, same GGA functional) of isotypic NbRuB did not increase the experimental B−B distance significantly,[6] thus the experimentally found mixed occupations (Os/Fe and B/Fe) in the new phase that were not accounted for in the current calculations could have impacted the experimental results by bonding optimization as mentioned above.

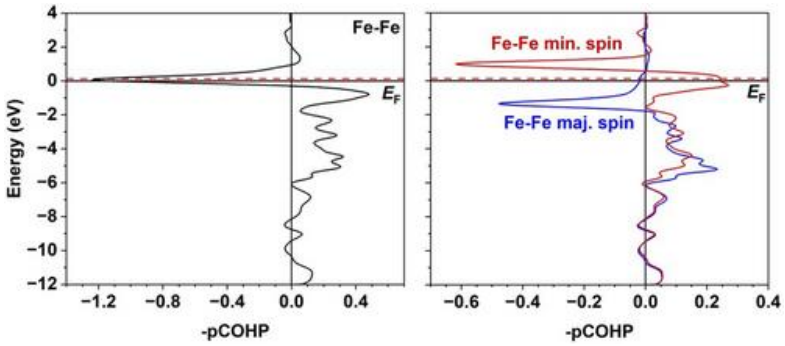

Figure 4.4. Non-spin polarized (left) and spin polarized (right) -pCOHP curves for intrachain Fe−Fe interaction in $TiFeOs_4B_3$. Fermi energy (E_F, black line) set at 0 eV, the red dashed line is the projected E_F of the experimental composition.

The COHP methodology can also be used to understand magnetic interactions in solids. The Fermi energy for the Fe−Fe interaction from the *nsp* calculations lies in the antibonding region (Figure 4.4, left), which has been interpreted before as a sign of either structural instability or as the presence of ferromagnetic interactions.[26] Indeed, spin-polarization annihilates almost all antibonding interactions at E_F, (Figure 4.4, right) a behavior characteristic of ferromagnetic interactions between the atoms involved, thus confirming the energy calculations favoring the two magnetic models (FM and AFM with ferromagnetic Fe chains). As mentioned in the DOS discussion, the projected E_F of the experimental composition is 0.12 eV above the ideal E_F position, but such a shift still places E_F in the peak area of the *nsp* -pCOHP plot (Figure 4.4, red dashed line), thus also favoring FM interactions for the experimental composition. Additionally, both the analyzed single crystal and the entire polycrystalline product are strongly attracted to an external magnet which would indicate dominating ferromagnetic interactions. Experimental quantification is still pending on either the synthesis of large crystals of the new phase or a polycrystalline product of higher quality and without unidentified peaks.

4.4 Conclusions

In this study, we have discovered the first quaternary composition of the NbRuB structure type, $TiFe_{1.3}Os_{3.9}B_{2.8}$, which is the latest in a series of quaternary compositions containing titanium, osmium, iron, and boron. The non-spin polarized DFT calculations indicate an electronic instability that is resolved with spin-polarization, indicating the presence of magnetic ordering. By incorporating the magnetic element iron in a structure that has produced the exciting NbRuB superconductor, the new composition becomes of interest for studying magnetic and superconducting properties. Such studies are pending improved synthesis of this phase.

4.5 Experimental Section

4.5.1 Synthesis and Characterization

The new phase was synthesized by mixing elemental powders of titanium (99.5 %, Alfa Aesar), iron (99+%, Alfa Aesar), osmium (99.8 %, Thermo Scientific), and boron (amorphous 95–97 %, Thermo Scientific) in starting stoichiometries of "$TiFe_2Os_3B_3$", "$TiFe_{1.5}Os_{3.5}B_3$" and "$TiFe_{1.3}Os_{3.9}B_{2.8}$" inside a glove box. The powders were then ground and mixed before being pressed into pellets. Each pellet was then arc-melted in a water-cooled copper crucible under an Ar atmosphere (99.995 %, Airgas) using a tungsten electrode at 20–30 V and 20 A. The metallic beads were then crushed and ground for Powder X-ray Diffraction (PXRD) analysis in a Rigaku Miniflex 600 diffractometer with Cu−Kα1 (λ=1.540593 Å) radiation. Rietvelt refinement[27] was applied

to refine the lattice parameters and identify the phases present in the products. Single crystals were selected from the "$TiFe_2Os_3B_3$" product under an optical microscope and analyzed in a STOE IPDS II diffractometer with graphite-monochromatized Mo−Kα (λ=0.71073 Å) radiation. Data collection and reduction were carried out with the STOE software package (Stoe and Xred). An empirical absorption correction (by multipole expansion)[28] was carried out. The single-crystal structure was solved and refined using SHELXL-2014/7.[29] The chemical composition of the single crystal was also analyzed using energy dispersive X-ray (EDX) spectroscopy on a LEO/Zeiss 1450 VP system.

4.5.2 Computational methods

The structural model was prepared from the NbRuB structure obtained from the ICSD database, and the atoms were adjusted to reflect the composition of the single-crystal data. As the single crystal had mixed occupancies, the structural model was simplified to not have mixed occupancies for sites with less than 15 % mixed occupancy (Os1/Fe1 and B2/Fe2 sites). The Os : Ti site (4j) had an occupancy of 0.51:0.49 from the single-crystal data, thus different combinations of two titanium and two osmium sites (in the primitive triclinic cell) were energetically analysed before conducting further calculations on a model system with the lowest energy. These simplifications led to a computational composition of $TiFeOs_4B_3$, which is very close to the experimental composition, $TiFe_{1.3}Os_{3.9}B_{2.8}$. For energy calculations, the lattice parameters, cell shape, cell volume, and atomic positions were allowed to relax using the projector augmented wave method in the Vienna *Ab-initio* Simulation Package (VASP).[30] All VASP calculations employed

the generalized gradient approximation (GGA) with exchange and correlation utilizing the Perdew, Burke and Ernzerhof (PBE) functional.[31] The cutoff energy was 450 eV, and the global break condition for the electronic SC-loop (E_{diff}) was 1E-06. The k-point mesh was a 5×19×9 Monkhorst-Pack grid. The magnetic calculations were performed by inputting initial magnetic moments onto the iron atoms for all steps, including relaxation calculations. Upon relaxing, self-consistency (SC) calculations were run followed by density of states (DOS) calculations. The DOS calculations utilized the CHGCAR file from the SC calculation, and the number of grid points on which the DOS was evaluated (NEDOS) was 2000. The projected Crystal Orbital Hamilton Population (pCOHP) calculations, and integrated COHP (ICOHP) calculations were run using Lobster.[32-34] For DOS and COHP plots, the Fermi energy (E_F) was set to 0 eV.

4.6 References

[1] T. Mori,J. SolidStateChem.2019,275,70–82.

[2] Q. Zheng,R. Gumeniuk,H. Borrmann,W. Schnelle,A. A. Tsirlin,H. Rosner,U. Burkhardt,M. Reissner,Y. Grin,A. Leithe-Jasper,DaltonTrans.2016,45, 9590–9600.

[3] V. Gvozdetskyi,M. P. Hanrahan,R. A. Ribeiro,T.-H.Kim,L. Zhou,A. J. Rossini,P. C. Canfield,J. V. Zaikina,Chem.Eur. J.2019,25,4123–4135.

[4] a) A. K. Iyer,Y. Zhang,J. P. Scheifers,B. P. T. Fokwa,J. SolidStateChem.2019,270,618–635.

[4] b) J. P. Scheifers,Y. Zhang,B. P. T. Fokwa,Accountof ChemicalResearch2017,50, 2317–2325.

[5] M. Mbarki,R. S. Touzani,C. W. G. Rehorn,F. C. Gladisch,B. P. T.Fokwa,J. SolidStateChem.2016,242,28–33.

[6] M. Mbarki,R. S. Touzani,B. P. T. Fokwa,Eur.J. Inorg.Chem.2014,2014,1381–1388.

[7] J. P. Scheifers,K. A. Gibson,B. P. T. Fokwa,ZeitschriftfürNaturforschungB2021,76, 727–731.

[8] C. Goerens,B. P. T. Fokwa,J. SolidStateChem.2012,192,113–119.

[9] D. Kotzott,M. Ade,H. Hillebrecht,SolidStateSci.2008,10,291–302.

[10] B. P. T. Fokwa,J. vonAppen,R. Dronskowski,Chem.Commun.2006,4419–4421.

[11] M. Ade,D. Kotzott,H. Hillebrecht,J. SolidStateChem.2010,183,1790–1797.

[12] B. P. T. Fokwa,M. Hermus,Angew.Chem.Int. Ed.2012,51,1702–1705.

[13] J. P. Scheifers,M. Küpers,N. G. Bakshi,R. S. Touzani,F. C.Gladisch,U. C. Rodewald,R. Pöttgen,B. P. T. Fokwa,Inorg.Chem.2023,62, 8670–8677.

[14] R. Forsythe,J. P. Scheifers,Y. Zhang,B. P. T. Fokwa,Eur. J. Inorg.Chem.2018,2018,3297–3303.

[15] Y. B. Kuzma,Dopov.Akad.NaukUkr.RSR Ser. A1967,939–940.

[16] W. Xie,H. Luo,K. Baroudi,J. W. Krizan,B. F. Phelan,R. J. Cava,Chem.Mater.2015,27, 1149–1152.

[17] Q. Zheng,R. Gumeniuk,H. Rosner,W. Schnelle,Y. Prots,U.Burkhardt,Y. Grin,A. Leithe-Jasper,J. Phys.Condens.Matter2015,27, 415701.

[18] F. Parvin,S. H. Naqib,ChinesePhysicsB.2017,26.

[19] M. Küpers,L. Lutz-Kappelman,Y. Zhang,G. J. Miller,B. P. T.Fokwa,Inorg.Chem.2016,55, 5640–5648.

[20] J. P. Scheifers,J. H. Flores,O. Janka,R. Pöttgen,B. P. T. Fokwa,Chem.Eur. J.2022,28, e202201058.

[21] O. Sichevych,S. Flipo,A. Ormeci,M. Bobnar,L. Akselrud,Y.Prots,U. Burkhardt,R. Gumeniuk,A. Leithe-Jasper,Y. Grin,Inorg.Chem.2020,59, 14280–14289.

[22] a) B. Petermüller,C. Neun,M. Stekiel,D. Zimmer,M. Tribus,K.Wurst,B. Winkler,H. Huppertz,Chem.Eur. J.2018,24, 14679–14685.

[22] b) B. P. T. Fokwa,M. Hermus,Inorg.Chem.2011,50,3332–3341.

[23] N. Sharma,M. Mbarki,Y. Zhang,A. Huq,B. P. T. Fokwa,Angew.Chem.Int. Ed.2018,57, 10323–10327.

[24] M. Hermus,M. Yang,D. Grüner,F. J. DiSalvo,B. P. T. Fokwa,Chem.Mater.2014,26, 1967–1974.

[25] P. Shankhari,N. G. Bakshi,Y. Zhang,D. Stekovic,M. E. Itkis,B. P. T. Fokwa,Chem.Eur. J.2020,26, 1979–1988.

[26] Y. Kurtulus,R. Dronskowski,J. SolidStateChem.2003,176,390–399.

[27] J. Rodriguez-Carvajal,insatellitemeetingon powderdiffractionof the XV congressof the IUCr,Vol. 127,1990.

[28] R. H. Blessing,ActaCrystallogr.Sect.A1995,51, 33–38.

[29] G. M. Sheldrick,ActaCrystallogrA FoundAdv2015,71, 3–8.

[30] G. Kresse,D. Joubert,Phys.Rev.B1999,59, 1758–1775.

[31] J. P. Perdew,K. Burke,M. Ernzerhof,Phys.Rev.Lett.1996,77,3865–3868.

[32] R. Dronskowski,P. E. Bloechl,J. Phys.Chem.1993,97, 8617–8624.

[33] V. L. Deringer,A. L. Tchougréeff,R. Dronskowski,J. Phys.Chem.A2011,115,5461 5466.

[34] S. Maintz,V. L. Deringer,A. L. Tchougréeff,R. Dronskowski,J.Comput.Chem.2016,37, 1030–103

4.7 Supporting Information

Table S4.1. Results of the Rietveld refinement for $TiFe_{1.3}Os_{3.9}B_{2.8}$ and elemental osmium corresponding to the Powder X-Ray Diffractogram (PXRD) in Figure S4.2.

	$TiFe_{1.3}Os_{3.9}B_{2.8}$	Os
a [Å]	10.866(2)	2.7256(3)
b [Å]	3.0248(4)	2.7256(3)
c [Å]	6.218(2)	4.3153(7)
R_{Bragg}	15.8	10.5
R_f	10.1	6.58
Phase fraction [wt-%]	40(2)	60(3)

Table S4.2. Selected distances in $TiFe_{1.3}Os_{3.9}B_{2.8}$.

Atoms 1,2	d 1,2 [Å]	Atoms 1,2	d 1,2 [Å]
Os1|Fe1—B1^{i}	2.22(5)	Os3|Ti3—Os3|Ti3^{ix}	2.573(5)
Os1|Fe1—B1	2.22(5)	Os3|Ti3—Os3|Ti3^{ix}	2.573(5)
Os1|Fe1—B2|Fe2^{i}	2.33(4)	Fe4—B2|Fe2	2.41(3)
Os1|Fe1—B2|Fe2^{i}	2.33(4)	Fe4—B2|Fe2^{ii}	2.41(3)
Os1|Fe1—B2|Fe2^{ii}	2.33(4)	Fe4—B2|Fe2^{ii}	2.41(3)
Os1|Fe1—B2|Fe2^{ii}	2.33(4)	Fe4—B2|Fe2^{x}	2.41(3)
Os1|Fe1—Fe4	2.615(7)	Fe4—B2|Fe2^{x}	2.41(3)
Os1|Fe1—Fe4^{i}	2.615(7)	Fe4—B2|Fe2^{i}	2.41(3)
Os1|Fe1—Os3|Ti3	2.721(2)	Fe4—B2|Fe2^{i}	2.41(3)
Os1|Fe1—Os3|Ti3^{iii}	2.721(2)	Fe4—B1^{xi}	2.44(6)
Os1|Fe1—Os3|Ti3^{iii}	2.721(2)	Fe4—Os1|Fe1^{xii}	2.615(7)
Os2—B1^{i}	2.19(2)	B1—Os2^{iii}	2.19(2)
Os2—B1	2.19(2)	B1—Os2^{xii}	2.19(2)
Os2—B2|Fe2^{iv}	2.36(4)	B1—Os2^{ii}	2.19(2)
Os2—B2|Fe2^{iv}	2.36(4)	B1—Os1|Fe1^{xii}	2.22(5)
Os2—Fe4^{iv}	2.678(5)	B1—Os1|Fe1^{xii}	2.22(5)
Os2—Fe4^{v}	2.678(5)	B1—Fe4^{v}	2.44(6)
Os2—Os2^{vi}	2.733(3)	B1—Os3|Ti3^{ii}	2.76(4)
Os2—Os3|Ti3^{vii}	2.739(2)	B2|Fe2—B2|Fe2^{viii}	1.99(7)
Os2—Os3|Ti3^{vii}	2.739(2)	B2|Fe2—B2|Fe2^{viii}	1.99(7)
Os2—Os3|Ti3^{vi}	2.739(2)	B2|Fe2—Os3|Ti3^{xii}	2.22(3)
Os2—Os3|Ti3^{vi}	2.739(2)	B2|Fe2—Os3|Ti3^{xii}	2.22(3)
Os3|Ti3—B2|Fe2^{i}	2.22(3)	B2|Fe2—Os3|Ti3^{viii}	2.22(3)
Os3|Ti3—B2|Fe2^{i}	2.22(3)	B2|Fe2—Os3|Ti3^{viii}	2.22(3)
Os3|Ti3—B2|Fe2	2.22(3)	B2|Fe2—Os3|Ti3^{ix}	2.22(3)
Os3|Ti3—B2|Fe2^{viii}	2.22(3)	B2|Fe2—Os3|Ti3^{ix}	2.22(3)
Os3|Ti3—B2|Fe2^{viii}	2.22(3)	B2|Fe2—Os1|Fe1^{xii}	2.33(4)
Os3|Ti3—B2|Fe2^{ix}	2.22(3)	B2|Fe2—Os1|Fe1^{xii}	2.33(4)
Os3|Ti3—B2|Fe2^{ix}	2.22(3)		

(i) x, 1+y, z; (ii) 1.5-x, -1-y, z; (iii) 1.5-x, -y, z; (iv) x, 1+y, 1+z; (v) x, y, 1+z; (vi) 1-x, -y, 1-z; (vii) 1-x, -1-y, 1-z; (viii) 1-x, -2-y, -z; (ix) 1-x, -1-y, -z; (x) 1.5-x, -2-y, z; (xi) x, y, -1+z; (xii) x, -1+y, z.

Table S4.3. Anisotropic displacement parameters (in Å^2) for $TiFe_{1.3}Os_{3.9}B_{2.8}$. $U_{12} = U_{23} = 0$.

Atom	U_{11}	U_{22}	U_{33}	U_{13}
Os1/Fe1	0.0063(9)	0.011(2)	0.006(2)	0
Os2	0.0062(6)	0.0129(8)	0.0055(7)	0.0002(5)
Os3/Ti3	0.007(1)	0.014(2)	0.017(2)	0.0020(9)
Fe4	0.026(4)	0.021(5)	0.010(4)	0

Table S4.4. Energy dispersive X-ray (EDX) results of the metals content for $TiFe_{1.3}Os_{3.9}B_{2.8}$.

Spectrum	Si	Ti	Fe	Os
Spectrum 1		28.08	12.30	59.62
Spectrum 2		29.30	11.72	58.98
Spectrum 3	5.72	26.65	10.15	57.48

Table S4.5. Selected experimental (d_{exp}, Å) and theoretical (d_{th}, Å) bond distances in $TiFeOs_4B_3$, and the corresponding pICOHP values (eV).

Bond	$TiFe_{1.3}Os_{3.9}B_{2.8}$ (d_{exp})	$TiFeOs_4B_3$ FM (d_{th})	$TiFeOs_4B_3$ FM pICOHP (Spin 1 + Spin 2)
B2/Fe2-B2/Fe2	1.99(7)	2.62	-1.015
Fe4-B2/Fe2	2.41(3)	2.15	-2.233
Os3/Ti3-B2/Fe2	2.22(3)	2.27 (Os3-B2), 2.40 (Ti3-B2)	-2.713 (Os3-B2), -1.745 (Ti3-B2)
Os2-B1	2.19(2)	2.19	-3.229
Os1/Fe1-B1	2.22(5)	2.25	-2.899
Fe4-Os2	2.678(5)	2.68	-0.814
Os3/Ti3-Os1/Fe1	2.721(2)	2.82 (Os3-Os1), 2.70 (Ti3-Os1)	-1.345 (Os3-Os1), -1.459 (Ti3-Os1)
Os2-Os2	2.733(3)	2.70	-2.369

Table S4.6. Lattice parameters [Å] and B_2 bond distances [Å] for $TiFe_{1.3}Os_{3.9}B_{2.8}$ (d_{exp}), theoretical (antiferromagnetic model) $TiFeOs_4B_3$ (d_{th}), theoretical (antiferromagnetic model) $TiFeOs_4B_3$ with B2 distance fixed at the single crystal B_2 distance (d_{th}/fixed B_2), and the NbRuB structure.

	$TiFe_{1.3}Os_{3.9}B_{2.8}$ (d_{exp})	$TiFeOs_4B_3$ (d_{th})	$TiFeOs_4B_3$ ($d_{th/fixed\ B2}$)	NbRuB (d_{exp})[6]
Lattice parameters	a = 10.841(9) Å b = 3.021(3) Å c = 6.201(5) Å	11.339 Å 2.902 Å 6.172 Å	11.184 Å 2.938 Å 6.212 Å	10.870(2) Å 3.173(1) Å 6.350(2) Å
B_2 bond distance	1.99(7) Å	2.61 Å	2.04 Å	1.88(2) Å

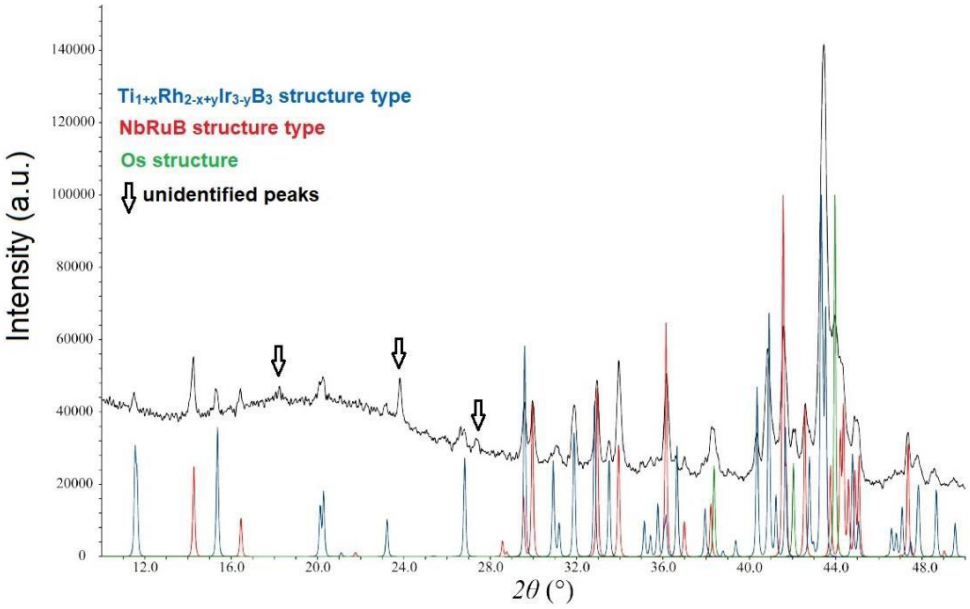

Figure S4.1. Powder X-ray Diffractogram consisting of NbRuB structure type (red), $Ti_{1+x}Rh_{2-x+y}Ir_{3-y}B_3$ structure type (blue), elemental osmium (green), and unidentified peaks (arrows).

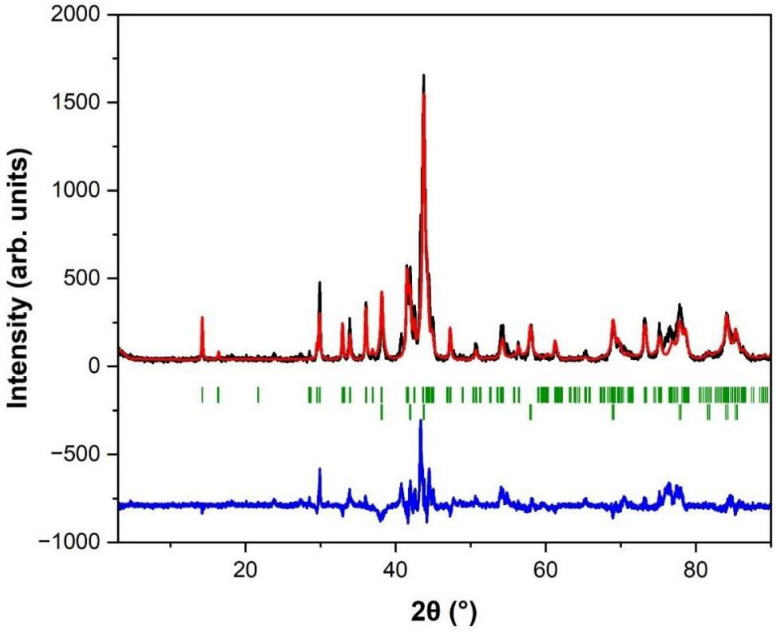

Figure S4.2. Observed (black) and calculated (red) powder X-ray diffraction pattern with starting stoichiometry $TiFe_{1.5}Os_{3.5}B_3$. The position of the Bragg reflections (green): $TiFe_{1.3}Os_{3.9}B_{2.8}$ (top row) and Os (bottom row). The difference curve (blue) obtained from Rietveld refinement.

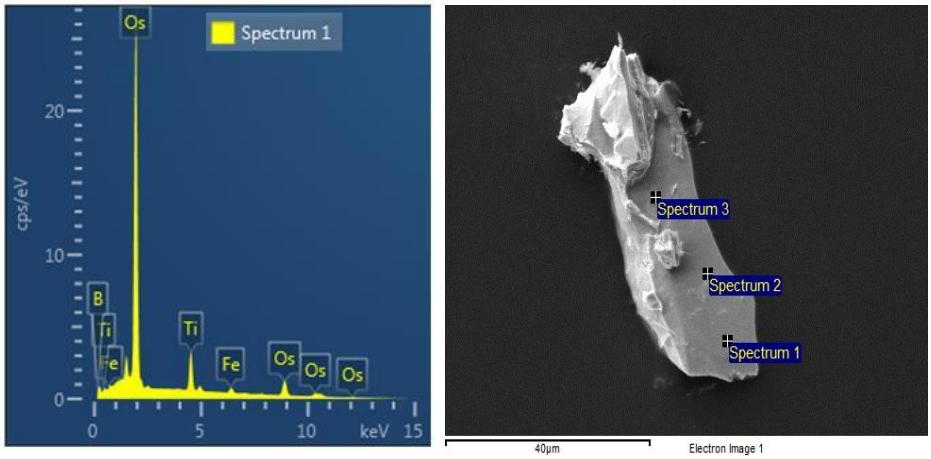

Figure S4.3. Energy dispersive X-ray (EDX) spectrum (left) of $TiFe_{1.3}Os_{3.9}B_{2.8}$ and an electron micrograph of the analyzed single crystal (right).

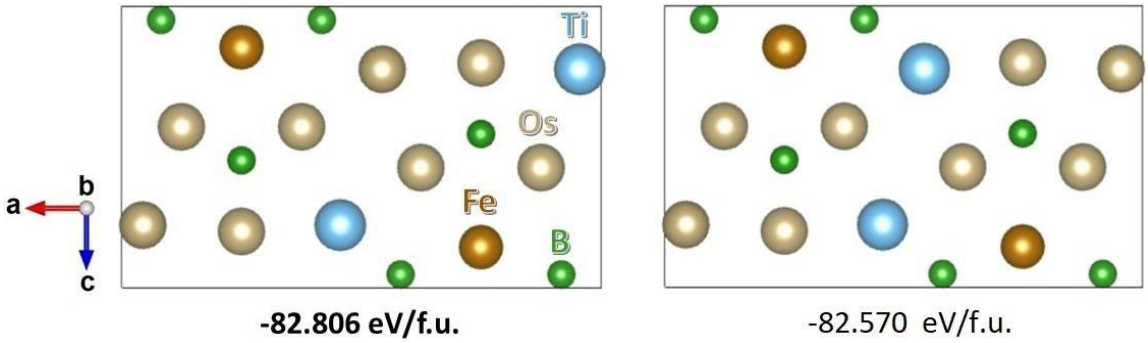

Figure S4.4. Structure models (non-spin polarized) and their relative energies for $TiFeOs_4B_3$ showing the different Ti and Os positions derived from the experimentally determined mixed occupied Os:Ti (50:50) site (4j).

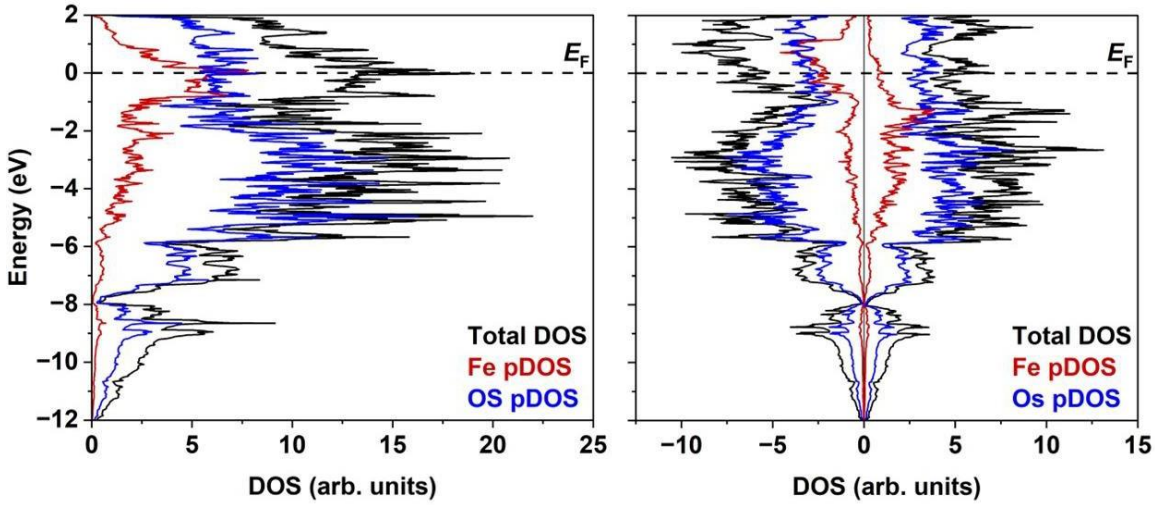

Figure S4.5. Total (black) and partial (colored) non-spin polarized DOS (left) for the unit cell of $TiFeOs_4B_3$.

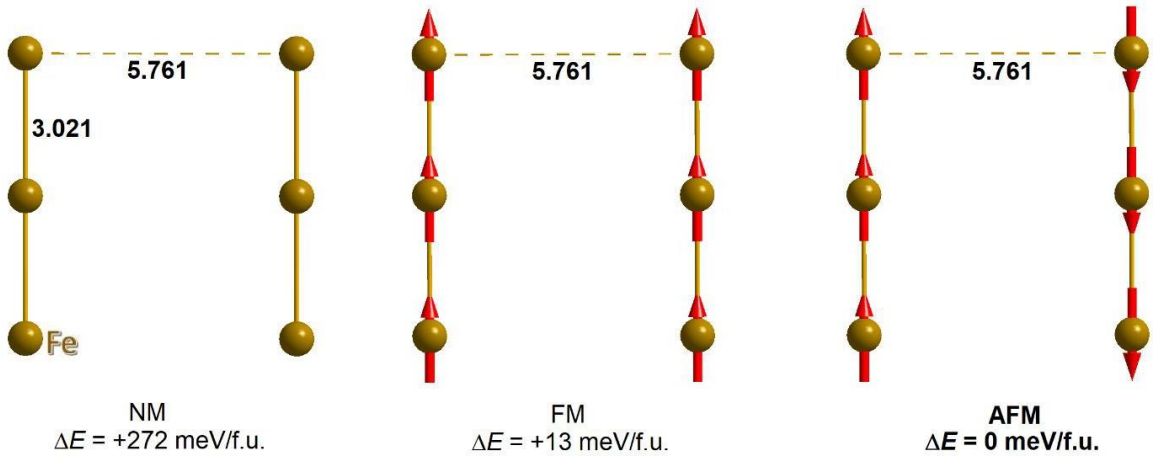

Figure S4.6. Magnetic models for $TiFeOs_4B_3$ based on the most favorable structure model from Figure S3.4. Energy differences are relative to the AFM ground state. Intrachain and interchain Fe-Fe distances given in Å.

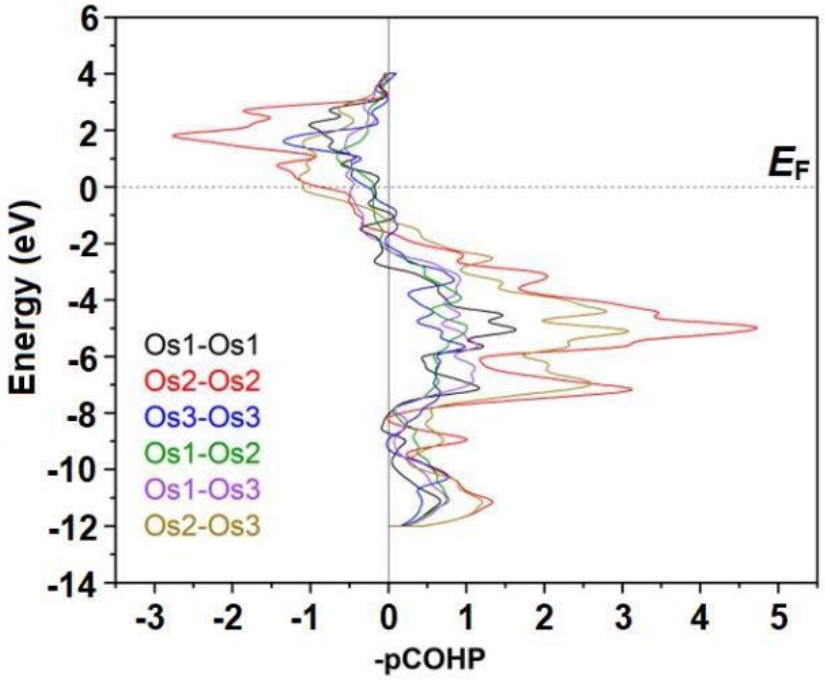

Figure S4.7. Projected COHP **(**pCOHP) curves for Os-Os interactions in $TiFeOs_4B_3$.

Chapter 5

Experimental and computational investigations of TiIrB: a new ternary boride with $Ti_{1+x}Rh_{2-x+y}Ir_{3-y}B_3$-type structure

Jan P. Scheifers, Kate A. Gibson and Boniface P. T. Fokwa*

5.1 Abstract

A new ternary phase, TiIrB, was synthesized by arc-melting of the elements and characterized by powder X-ray diffraction. The compound crystallizes in the orthorhombic $Ti_{1+x}Rh_{2-x+y}Ir_{3-y}B_3$ structure type, space group *Pbam* (no. 55) with the lattice parameters a = 8.655(2), b = 15.020(2), and c = 3.2271(4) Å. Density Functional Theory (DFT) calculations were carried out to understand the electronic structure, including a Bader charge analysis. The charge distribution of TiIrB in the $Ti_{1+x}Rh_{2-x+y}Ir_{3-y}B_3$- type phase has been evaluated for the first time, and the results indicate that more electron density is transferred to the boron atoms in the zigzag B_4 units than to isolated boron atoms.

5.2 Introduction

We recently reviewed borides with a metal-to-boron ratio (M:B) of 2:1, highlighting their structural variations, relationships, and physical properties [1]. The currently known 130 phases (from binaries to quaternaries) crystallize with 21 structure types. Most of these structures are based on B-centered trigonal prisms instead of other modes of

coordination, such as those with octahedrally coordinated B atoms. When these prisms share one or more rectangular faces, bonding occurs between neighboring boron atoms. For example, in the MoAlB-type structure infinite zigzag B chains are observed because of shared rectangular faces along the crystallographic *c* axis [2]. However, many structures with finite boron fragments exist, such as trigonal planar B_4 fragments in the $Ti_{1+x}Os_{2-x}RuB_2$ structure [3] and zigzag B_4 fragments in the Ni_3ZnB_2 [4] and $Ti_{1+x}Rh_{2-x+y}Ir_{3-y}B_3$ [5] structures. Another rare configuration of the B_4 fragment is observed in β-Cr_2IrB_2 [6], where the B_4 fragment is bent, while a second modification, α-Cr_2IrB_2 [6], contains the common zigzag B_4 fragment. These B_4-based structures have produced some exciting materials including the ferrimagnetic $TiCrIr_2B_2$ [7] and the superconducting LT-NbOsB [8]. Interestingly, LT-NbOsB remains the only available ternary boride with an orthorhombic $Ti_{1+x}Rh_{2-x+y}Ir3_{-y}B_3$-type structure, where Nb occupies the Ti and Rh positions while Os occupies the Ir positions. In addition to the quaternary compound, four other phases were recently presented as part of an exciting series, $Ti_{2-x}M_{1+x-\delta}Ir3_{+\delta}B_3$ (M = Mn–Ni and $\delta < 0.2$) [9], in which a substructure change from trigonal planar B_4 units (for M= V–Mn and x = 0.5) to zigzag B_4 units (for M = Mn–Ni and x = 0) was observed along the series. Members of the series with early transition metals M = V–Mn crystallize in a hexagonal $Ti_{1+x}Os_{2-x}RuB_2$-type structure. Consequently, an extrapolation of this series where M = Ti hints at a possible ternary phase, TiIrB, crystallizing with $Ti_{1+x}Os_{2-x}RuB_2$-type structure. The only Ti-based ternary phase with this structure containing trigonal planar B_4 units is $Ti_{1.6}Os_{2.4}B_2$ [10]. As mentioned above, LT-NbOsB is another ternary phase with a M:B of 2:1 that contains B_4

units, but crystallizes with the $Ti_{1+x}Rh_{2-x+y}Ir_{3-y}B_3$-type structure containing a zigzag configuration of the B_4 units instead. We recently also discovered another modification of NbOsB, HT-NbOsB [11], which crystallizes with its own structure type and contains infinite zigzag B chains instead of B_4 units. Herein, we report on the discovery of the anticipated ternary phase "TiIrB", its crystal and electronic structures, as well as its Bader charge analysis.

5.3 Results and discussion

5.3.1 Phase analysis and structure refinement

The TiIrB sample was synthesized by arc-melting of the elements as detailed in the Experimental Section. Phase analysis of the arc-melted product by powder X-ray diffraction (PXRD) indicated four crystalline phases in the sample. Subsequent Rietveld refinement of the PXRD pattern in FULLPROF [12] generated Figure 1, with results summarized in Table 1. Besides the known TiB_2 (AlB_2 type), TiIr (CuAu type) and $TiIr_3$ (Cu_3Au type) phases, a new phase could be identified whose lattice parameters and space group (*Pbam*) indicate the $Ti_{1+x}Rh_{2-x+y}Ir_{3-y}B_3$ structure type. The refined lattice parameters of the new phase are a = 8.655(2), b = 15.020(2), and c = 3.2271(4) Å. These lattice parameters and the unit cell volume are larger than those reported for quaternary phases containing smaller transition metals, M = Mn–Ni [9], and Rh containing $Ti_{1+x}Rh_{2-x+y}Ir_{3-y}B_3$. This is expected since a larger Ti atom replaces the smaller Rh atom. The refined weight fractions (given in Table 1) indicate that the new phase constitutes 27.9(8) wt. % of the sample. To increase the weight fraction of the new phase the amount

of iridium in the starting material was increased to a higher ratio, but this change yielded a sample containing less of the targeted phase, even though the formation of TiIr was suppressed.

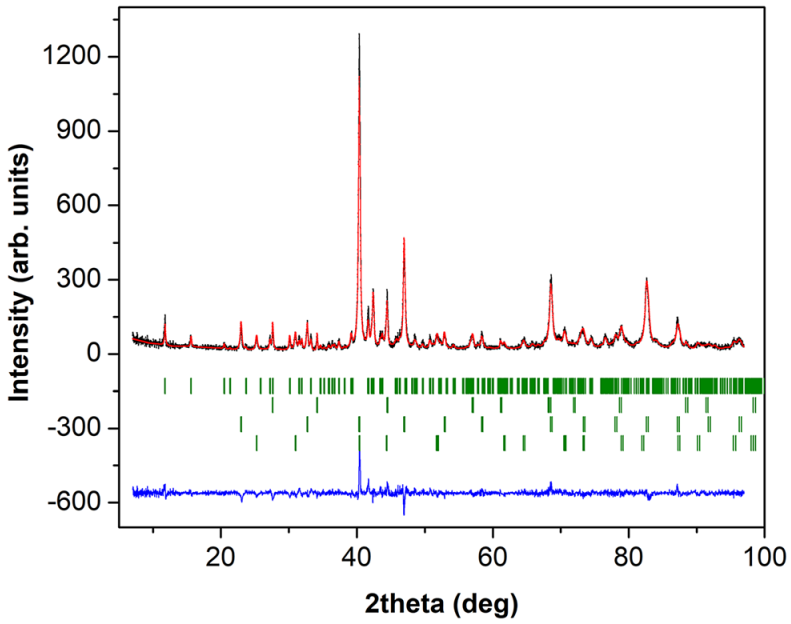

Figure 5.1. Observed (black) and calculated (red) powder X-ray diffraction pattern of TiIrB; the position of the Bragg reflections (green) for TiIrB (top row), TiB_2 (second row), $TiIr_3$ (third row), and of TiIr (bottom row); the difference curve (blue) obtained from Rietveld refinement.

Table 5.1. Details of the Rietveld refinement for TiIrB sample.

Refined composition	**$Ti_{0.93(1)}Ir_{1.07(1)}B$**
Space group, *Z*	*Pbam*
a,Å	8.655(2)
b,Å	15.020(2)
c,Å	3.2271(4)
V, Å^3	419.5(1)
2θ range, deg	7.02-96.96
Refinement method	Least-squares
Profile function	Pseudo-voigt
R_{Bragg}	9.92
Fraction, wt. %	27.9(8)
By-products, fraction, wt. %	TiB_2, 14.0(9) $TiIr_3$, 41.6(8) TiIr, 16.5(6)

Rietveld refinement was successfully applied to refine the atomic positions and occupational factors for the new phase. For this refinement the asymmetric unit of the $Ti_{1+x}Rh_{2-x+y}Ir_{3-y}B_3$ parent compound was used as the starting model (Figure 2), replacing Rh with Ti and neglecting all mixed occupancies in the first run. After convergence, mixed occupancies of Ir and Ti were successfully refined on two out of three possible Ti sites (see Table 2), leading to a refined composition of $Ti_{0.93(1)}Ir_{1.07(1)}B$ indicating a phase width with general formula $Ti_{3-x}Ir_{3+x}B_3$. The Ir content mixed on the Ti sites correlates well with the volume of the different coordination polyhedra, with the largest polyhedron exclusively occupied by Ti and the smallest polyhedron containing the highest fraction

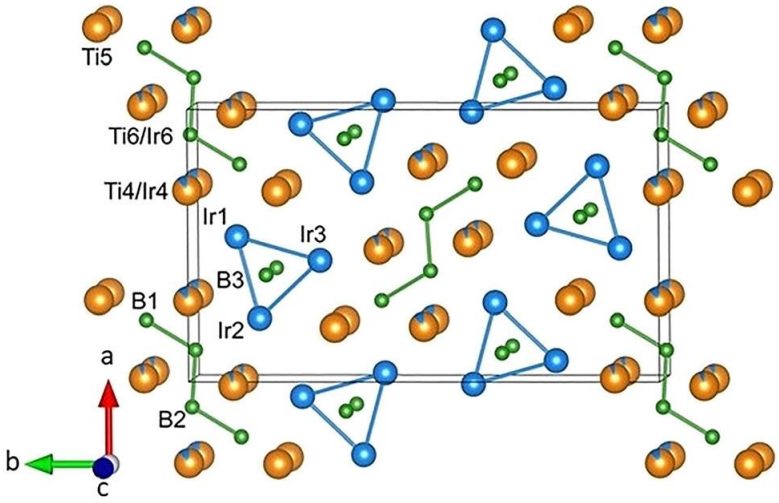

Figure 5.2. Projected structure of TiIrB ($Ti_{1+x}Rh_{2-x+y}Ir_{3-y}B_3$ type) as obtained from Rietveld refinement.

Table 5.2. Atomic coordinates from PXRD experiments and DFT calculations and site occupation factors (SOF) for TiIrB.

Atom label	Wyckoff position	*x* (PXRD)	*x* (DFT)	*y* (PXRD)	*y* (DFT)	*z* (PXRD/DFT)	SOF (PXRD)
B3[a]	4*g*	0.107	0.111	0.334	0.333	0	1
B1[a]	4*h*	0.214	0.213	0.100	0.099	1/2	1
B2[a]	4*h*	0.395	0.396	0.496	0.496	1/2	1
Ir1	4*h*	0.481(1)	0.479	0.094(1)	0.096	1/2	1
Ir2	4*h*	0.281(1)	0.282	0.3586(8)	0.358	1/2	1
Ir3	4*h*	0.068(1)	0.068	0.2301(7)	0.231	1/2	1
Ti4/Ir4	4*g*	0.302(5)	0.299	0.004(2)	0.003	0	0.866(1)/ 0.134(1)
Ti5	4*g*	0.300(6)	0.314	0.204(3)	0.203	0	1
Ti6/Ir6	4*g*	0.019(3)	0.017	0.097(3)	0.093	0	0.926(1)/ 0.074(1)

[a]Atomic coordinates are based on geometric considerations and on data of isostructural compounds.

The volume of the polyhedra and how it affects the coloring of the different Ti sites has been discussed in more detail for quaternary compounds containing three transition metals [9]. Given that x is very small, we use the ideal composition, TiIrB, for simplification when referring to the new compound. The refined interatomic distances around the B atoms (Table 3) were all within expected ranges as found in borides containing these transition metals, especially those mentioned above that have the same or similar structures [3, 5, 7–11]. The flat B_4 units have bond angles of ca. 117°, which agrees very well with the bond angle in the relaxed computational structure (see electronic structure section below). The B–B interatomic distances are provided without uncertainty as the boron positions have not been refined. However, these coordinates match well with the coordinates of the relaxed structure (Table 2). The chemical bonding analysis performed previously for similar borides containing B_4 fragments has indicated that the boron-based interactions are the strongest bonds [3, 5, 7, 8].

Table 5.3. Experimental interatomic distances (Å) around the boron atoms in TiIrB obtained from Rietveld refinement.

B3	Ir1	2.23(1)
	Ir2	2.24(1)
	Ir3	2.27(1)
B1	B2	1.83
	Ti4|Ir4	2.29(2)
	Ir1	2.31(1)
	Ti6|Ir6	2.34(2)
	Ir3	2.33(1)
	Ti5	2.37(3)
B2	B2	1.82
	B1	1.83
	Ir2	2.29(1)
	Ti4|Ir4	2.35(3)
	Ti6|Ir6	2.34(3)
	Ti6|Ir6	2.39(3)

5.3.2 Electronic structure

The electronic structure was calculated with the Vienna ab Initio Simulation Package (VASP) as detailed in the Experimental Section. The resulting structure, after relaxation, had lattice parameters of a = 8.707, b = 15.094, and c = 3.2412 Å which agree with the experimental data. A slight overestimation of all three parameters is observed, as expected from generalized gradient approximation (GGA) calculations. The atomic coordinates after relaxation agree well with the coordinates used for the Rietveld refinement (Table 2). The total Density of States (DOS) and partial Density of States (pDOS) are illustrated in Figure 3. Boron slightly dominates the low-lying part of the valence band between −9 and −12 eV. Iridium states dominate the DOS below the Fermi energy (E_F) and titanium states dominate above E_F, as expected from their different electronegativities. The Fermi energy is located within a pseudo-gap that extends between −1.5 and 0.5 eV, hinting at an optimized electronic structure and confirming the stability of this phase with an almost ideal composition of TiIrB. However, having a finite DOS at EF infers metallic character, as expected for this metal-rich boride. The results of a Bader charge analysis indicate that titanium atoms transfer electron density to Ir and B, as their average valence electron count is 9.81 (instead of 9) and 3.52 (instead of 3), respectively, while that of Ti is 2.67 (instead of 4). Remarkably, the boron atoms in the B_4 zigzag fragments retain higher electron density (charge of −3 per B_4 fragment) compared to the lone boron atoms (charge of −0.025 per lone boron atom). The pDOS of

the lone boron atoms and B_4 zigzag fragments are compared in Figure 4. The pDOS of B is almost uniform in the range of −1 to −8 eV (see Figure 3), but when divided into two components, the pDOS of the lone B atoms and the pDOS of the B_4 fragments, significant differences become apparent. The pDOS of the B_4 fragments make up most of the boron pDOS in the range of −1 to −5.5 eV compared to that of the lone boron atoms.

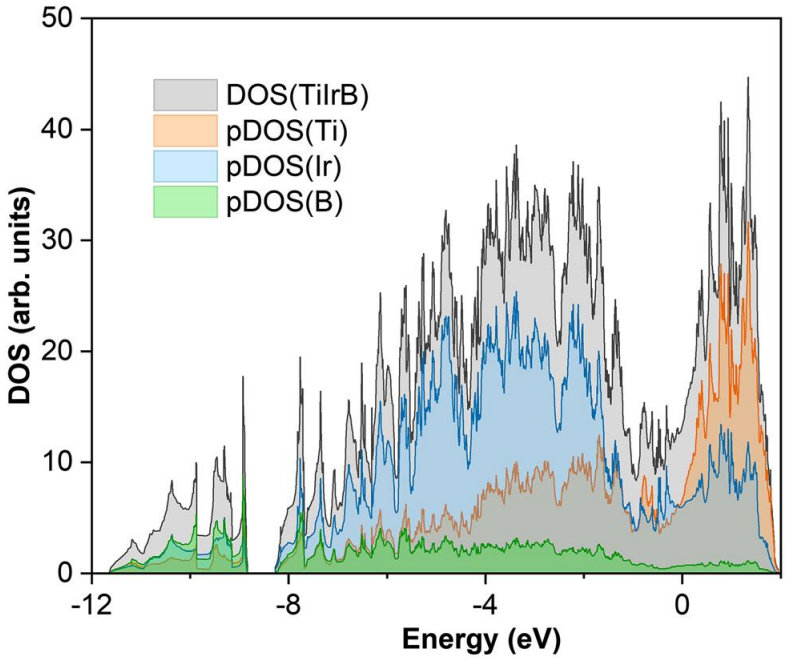

Figure 5.3. Total and partial density of states (DOS) plots for TiIrB.

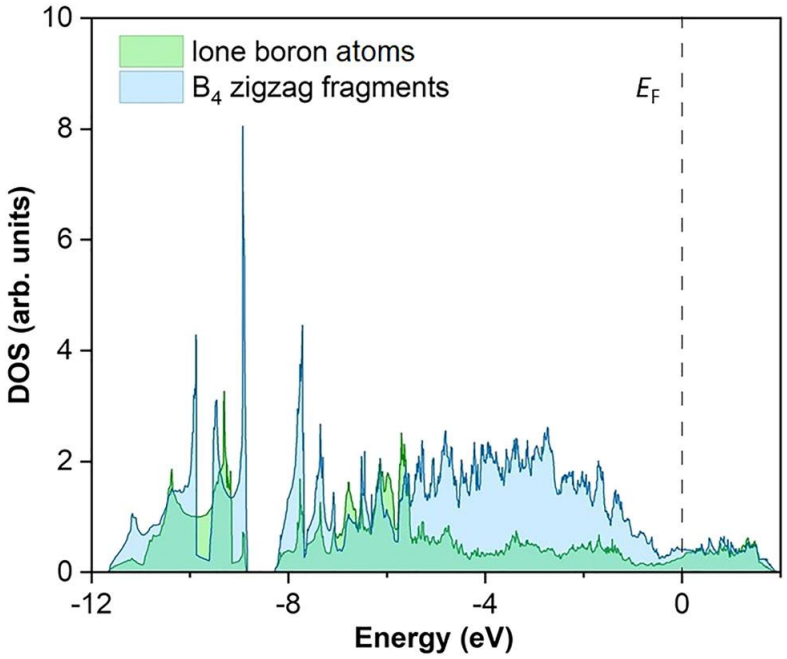

Figure 5.4. Partial density of states (DOS) plots for the lone boron atoms and the B_4 zigzag boron fragments.

Thus, it is reasonable to assume that those states are occupied by the additional electrons that have been transferred to the B_4 fragments from Ti. Because of the charge transfer, the atoms at z = 1/2 form a negatively charged layer containing Ir atoms and B_4 fragments, and a positively charged layer at z = 0 containing Ti and lone B atoms. However, not all valence electrons of Ti have been transferred, so it is plausible to also assume significant metallic bonding between the layers. Furthermore, covalent interactions are expected between the lone boron and the surrounding Ir atoms, as found in similar compounds [3, 5, 7, 8]. Consequently, a complex mixture of covalent and metallic bonding as well as some level of electron transfer are the major characteristics of this metal-rich boride.

5.4 Conclusions

We have synthesized the new boride $Ti_{0.94(1)}Ir_{1.06(1)}B$ for the first time and showed that it crystallizes with the orthorhombic $Ti_{1+x}Rh_{2-x+y}Ir_{3-y}B_3$ structure type. The structure was refined based on its powder X-ray diffraction pattern, and the apparent occupational disorder was elucidated. First-principles calculations explored the electronic structure and a Bader charge analysis has shown that electron density is transferred from Ti to both Ir and B. However, the boron atoms building the B_4 fragments inherit more electron density than the isolated B atoms.

5.5 Experimental section

5.5.1. Synthesis of TiIrB

Ti (99.99%), Ir (99.9%) and B (99% amorphous) were used as purchased from Alfa Aesar, and any air sensitive materials were handled in a glovebox. A starting elemental composition of 1Ti:1Ir:1B was mixed in powder form until a homogenous mixture was obtained before being pressed into a dense pellet. The pellets were then melted in an argon-filled arc furnace. Upon arc-melting, The small metallic bead obtained after arc melting was powdered and characterized by Powder X-ray Diffraction (PXRD) in a Rigaku MiniFlex 600 instrument with CuKα1 radiation (λ = 1.54,059 Å) and a Ge monochromator. The refined experimental values were used to provide the information in Tables 1–3, and Figures 1 and 2. CSD 2107342 contains the supplementary

crystallographic data for this paper. These data can be obtained free of charge from The Cambridge Crystallographic Data Centre via www.ccdc.cam.ac.uk/data_request/cif.

5.5.2. Computational methods

DFT calculations were used to investigate the electronic structure of the new compound. The TiIrB structural model was prepared in accordance with the $Ti_{1+x}Rh_{2-x+y}Ir_{3-y}B_3$ structure type in which the Rh positions were fully occupied by Ti. A model without occupational disorder was used to represent the refined X-ray diffraction data, which showed that less than 12% Ir is mixed on two out of three possible Ti sites. The lattice parameters were relaxed using the projector augmented wave method of Blöchl [13, 14] coded in VASP [15]. All VASP calculations employed the generalized gradient approximation (GGA) with exchange and correlation treated by the Perdew-Burke Enzerhoff (PBE) functionals [16]. The cutoff energy was 450 eV, and the k-point mesh was 19 × 19 × 19. The global break condition for the electronic SC-loop (Ediff) was 1E − 06, and the Fermi level was set to zero. After relaxation, short-circuit (SC) calculations were run. The DOS calculations utilized the CHGCAR file from the SC calculation, with the number of grid points on which the DOS is evaluated (NEDOS) being 2000, making sure to converge the k-points. Bader charge analysis was also performed, ensuring the k points were converged to ensure an accurate grid for these calculations [17].

5.6 References

1. Iyer A. K., Zhang Y., Scheifers J. P., Fokwa B. P. T. J. Solid State Chem. 2019, 270, 618–635.

2. Jeitschko W. Monatsh. Chem. 1966, 97, 1472–1476.

3. Fokwa B. P. T., von Appen J., Dronskowski R. Chem. Commun. 2006, 4419–4421; https://doi.org/10.1039/b608903h.

4. Malik Z., Grytsiv A., Rogl P., Giester G., Bursik J. J. Solid State Chem. 2013, 198, 150–161.

5. Goerens C., Fokwa B. P. T. J. Solid State Chem. 2012, 192, 113–119.

6. Kotzott D., Ade M., Hillebrecht H. Solid State Sci. 2008, 10, 291–302.

7. Küpers M., Lutz-Kappelman L., Zhang Y., Miller G. J., Fokwa B. P. T. Inorg. Chem. 2016, 55, 5640–5648.

8. Zheng Q., Gumeniuk R., Rosner H., Schnelle W., Prots Y., Burkhardt U., Grin Y., Leithe-Jasper A. J. Phys. Condens. Matter 2015, 27, 415701.

9. Scheifers J. P., Küpers M., Zhang Y., Lutz-Kappelman L., Miller G. J., Fokwa B. P. T. Solid State Sci. 2020, 107, 106294.

10. Fokwa B. P. T., Dronskowski R. Z. Anorg. Allg. Chem. 2008, 634, 1955–1960.

11. Forsythe R., Scheifers J. P., Zhang Y., Fokwa B. P. T. Eur. J. Inorg. Chem. 2018, 2018, 3297–3303.

12. Rodríguez-Carvajal R. FULLPROF2000, A program for Rietveld refinement and pattern matching analysis. In Satellite Meeting on Powder Diffraction of the 15th International Congress of the IUCr ; Laboratoire Léon Brillouin (CEA-NRS) Gif sur Ivette: Cedex, France, 1990; p. 127, See also: Rodríguez-Carvajal J. Phys. B, 1993, 192, 55–69.

13. Blöchl P. E. Phys. Rev. B 1994, 50, 17953–17979.

14. Kresse G., Joubert D. Phys. Rev. B 1999, 59, 1758–1775.

15. Kresse G., Furthmüller J. Phys. Rev. B 1996, 54, 11169–11186.

16. Perdew J. P., Burke K., Ernzerhof M. Phys. Rev. Lett. 1996, 77, 3865–3868.

17. Henkelman G., Arnaldsson A., Jónsson H. Comput. Mater. Sci. 2006, 36, 354–360.

Chapter 6

Conclusion

The nine novel structures obtained in this dissertation, belonging to the $Ti_3Co_5B_2$, NbRuB, and $Ti_{1+x}Rh_{2-x+y}Ir_{3-y}B_3$ structure types, have advanced our understanding magnetic materials. The combined efforts of computation and experimentation have also enabled the study of these novel materials on a level deeper than either individual method.

The synthesis of $Hf_2MOs_5B_2$ (M = Fe, Mn, or Co) resulted in semi-hard and hard magnets, indicating that osmium is capable of replacing ruthenium or iridium to make hard magnets. The degree of hardness for some of the osmium quaternary phases are on par with members of the previously published $Hf_2Fe_{1-d}Ru_{5-x}Ir_{x+d}B_2$ series which is also of the same $Ti_3Co_5B_2$ structure type. With this foundation, $Hf_2MOs_4IrB_2$ and $Hf_2MOs_3Ir_2B_2$ (M = Mn, Fe) were also synthesized and the computational results indicate a high possibility of obtaining one of the hardest magnetic materials of the $Ti_3Co_5B_2$ structure type. Magnetic measurements are currently underway on these latter two compositions. The discovery of the $TiFe_{1.3}Os_{3.9}B_{2.8}$ ferromagnet has shown the NbRuB structure type can form magnetic materials, opening another avenue to the synthesis of magnetic materials. TiIrB is one of the few ternary phases of the $Ti_{1+x}Rh_{2-x+y}Ir_{3-y}B_3$ structure type, and computational calculations indicated a preference for the titanium atoms to donate electron density to the B_4 zigzag units as opposed to the lone boron atoms.